Orientation Selective Effects in III-V Heterostructure Systems with Application to Nanostructure Fabrication

Thesis by

Michael Eugene Hoenk

In Partial Fulfillment of the Requirements

for the Degree of

Doctor of Philosophy

California Institute of Technology

Pasadena, California

1990

(Submitted May 15, 1990)

© 1990

Michael Eugene Hoenk

All Rights Reserved

to my parents

with all of my love

Acknowledgments

Essential to the process of completing the work presented here were the friendship, collaboration, and assistance of my family, friends, and colleagues. They are a part of this thesis, and a part of my life.

For everything he has done to make this thesis possible, and for his friendship, encouragement, and guidance, I express my sincere gratitude to my advisor, Professor Kerry Vahala.

Special thanks to my friends, the members of my research group with whom I have had invaluable collaborations and discussions, both scientific and otherwise. To Mike Newkirk, with whom I share an office and a friendship, thank you for everything. To Pete Sercel and John Lebens, good friends who contributed to the work presented here, thank you. To Hal Zarem, my friend and colleague whose entrepreneurial efforts are connected to part of this thesis, thank you for first directing me to Kerry's group, for introducing me to windsurfing, and for your friendship. Thanks to the recent members of the group, Charles Tsai and Jay Dawson, with whom I have enjoyed working. To Dragan Gaj́ic, who left a short while ago for Columbia University to start work on his own Ph.D. thesis, thank you (and good luck).

I would like to thank the scientists who collaborated in parts of this work, Howard Chen, Simon Nieh, Professor Amnon Yariv, and Professor Hadis Morkoç. I would especially like to thank Professor Amon Yariv and Professor David Rutledge, who kindly allowed me to use the facilities in their laboratories. To Professor Brent Fultz, Channing Ahn, and Carol Garland, who provided me with training and invaluable

instruction in transmission electron microscopy, thank you very much. Thanks to Professor Bill Bridges, with whom I shared a brief collaboration. To my colleagues who have contributed to this work through many enjoyable discussions, Michael Mittelstein, Lars Eng, Joel Paslaski, T. R. Chen, and David Chow, thank you very much. Special thanks go to Desmond Armstrong and Ali Ghaffari, for their help on numerous occasions.

I would like to acknowledge the various agencies and companies that supported the research appearing in this thesis. I would particularly like to thank the National Science Foundation, for supporting me through an NSF Graduate Fellowship during the first three years of my graduate study.

I would like to thank all of the members of the Caltech staff, whose have contributed to the completion of this thesis. Special thanks go to all of the secretaries who have helped me through my graduate studies: Vicky Arriola, Rosalie Rowe, Donna Driscoll, Jana Mercado, Laura Rodriguez, and Linda Dosza. Much of the apparatus discussed in Chapter 2 was machined by Larry Begay, whose fine work was essential to the completion of this thesis. Thanks also to Elmer Szombathy and Marty Gould, who helped me in my efforts at machining. To the Caltech librarians who helped me with the references in this thesis, thank you very much.

Warm thanks go to my teachers, without whom none of this would have happened. To Professor Bill Klink, who provided guidance and instruction while I was an undergraduate, thank you for your patient encouragement and guidance. I would like to express my sincere gratitude to Donald Schaefer, who with consummate skill

as a teacher introduced me to physics at Bettendorf High School, and to Joanna Stuhr, who as a high school teacher of mathematics has had the courage to demand excellence of her students. You are all a special part of this thesis.

To my colleagues and friends Professor Frank Porter, Eric Soderstrom, Zhaoping Li, Andrew Weir, Ryszard Stroynowski, Barrett Millikan, Dolly Wu, and Mark Nelson, with whom I worked for a year in high energy physics, thank you very much.

Among all of the friends that I have made in graduate school, some stand out for that quality of friendship that is, and will always be, the best part of life. To my best friend, Bob Walker, whose wit and warmth made life fun even during the most difficult of times, thank you for your friendship. To my special friends, Michael Mittelstein and Soheila Mirhashemi, whose warm friendship I shall always treasure, thank you for all of your support and encouragement. Special thanks to Michael Coleman Miller, with whom I enjoyed many movies, chess games, and discussions about Big 10 sports.

There have been many friends and colleagues who have contributed to this work through numerous discussions, softball, basketball, and volleyball games, and a few beers. Special thanks to Doug Collins, Tom Fric, and John Apostolakis. To my friends Duncan and Susan Weathers, Steve and Sherri Spicklemire, and Michelle Vine, thank you for your friendship, and for the stimulating discussions in FWIF. I would especially like to thank my teammates on the InfraRed Sox, who are all winners, regardless of the outcome of the playoffs, and who provided me with my nickname, "Mad Dog." The InfraRed Sox roster: Doug Collins, Mike Brown, Joe Vittitoe, Ed

Croke, Patti Pratt (honorary member), Dave Chow, Ed Yu, Andy Mutz, Marcia Hudson, Todd Rossi, Professor Tom Christman, Jay Dawson, John Lebens, Moonil Kim, Chuck Krill, Hong Jiao, Doug Pearson, Dave Lee, Dave Ting, Jay Dawson, Victor Leyva, Jan Soderstrom, Yixin Liu, Johannes Swenberg, George Haas, Mark Phillips, Bin Zhao, Yasantha, Kathy Widdowson, Bob Fox, Channing Ahn, Koichi Sayano, Yong, and Professor Harry Atwater.

My love and gratitude goes to my family, for providing me with the confidence and dedication to complete this thesis. To my father and mother, whose support and encouragement carried me through the hard times and added to the joy of the good times, I love you with all of my soul. To my brothers, Steve and Mark, whose friendship and love I hold as one of the greatest treasures of my life, I love you very much. To Grandma and Grandpa Nicholson, who have a very special place in my heart, my deepest love and affection.

I would like to thank the new members of my family, for their love and support, particularly during the time when my fiancee was at Argonne National Laboratories. Thank you, Lance and Azar, for welcoming me into your home, and Kamran, for your friendship.

To my beautiful bride, Shouleh Nikzad, whose love, support, encouragement, and sense of humor have added another dimension to my life, you are my inspiration and joy. I couldn't have done this without you. I love you, now and always.

Abstract

Orientation selective effects in the molecular beam epitaxial (MBE) growth of $Al_{1-x}Ga_xAs$ on a patterned (100) GaAs substrate are investigated. Under particular growth conditions, the spontaneous, selective formation of a superlattice or quantum wire array on the sides of grooves is observed. Experiments and modelling indicate that this growth technique, orientation selective epitaxy (OSE), has application to the *in situ* growth of nanometer scale structures.

An optical fiber cathodoluminescence system is described. By using an optical fiber to collect light directly from the surface of the sample, spectrally resolved cathodoluminescence measurements can be done without precluding simultaneous measurement of other signals. The system attains comparable performance to alternative systems which utilize concave mirrors for light collection. A cryogenic cold stage, using a continuous flow of liquid helium or nitrogen, is described.

Experimental results on the MBE growth of $Al_xGa_{1-x}As$ on $[01\bar{1}]$ grooves in a (100) GaAs substrate exhibit orientation selective effects. Spontaneous growth of a superlattice is observed on the sides of grooves. The superlattice, with a period of approximately 70Å, exhibits strong luminescence, red-shifted by 127 meV from the emission of uniform $Al_{0.25}Ga_{0.75}As$ grown on adjacent facets. This is the first observation of compositional modulation in the growth of AlGaAs on a {111} surface. The abrupt termination of the superlattice at the interface with adjacent facets constitutes a heterojunction oriented lateral to the growth direction, the first such structure to be formed spontaneously during growth.

Orientation selective epitaxy is modelled, using calculations and Monte Carlo simulations of growth on surfaces inclined with respect to the substrate rotation axis. The proposed mechanism predicts an in-plane variation of the composition, resulting from growth by step flow in the presence of time dependent fluxes. The time dependence is caused by the inclination of the surface with respect to the substrate rotation axis.

The dependence of OSE growth on surface orientation is investigated by varying groove orientation in a patterned (100) GaAs substrate. A strong dependence of cathodoluminescence emission on groove orientation is observed. In some ranges of groove angles, monotonic dependence of the peak emission on groove orientation is observed, suggesting the possibility of bandgap tuning by variation of surface orientation. In growth on [010] grooves, quantum wire arrays were observed, with a wire dimension of approximately 60Å.

The growth of $Al_xGa_{1-x}As$ in oval defects is investigated. A strong dependence of the composition on the orientation of growth in oval defects is observed. Comparison with growth in grooves indicates that orientation selective epitaxy plays a role in determining $Al_xGa_{1-x}As$ composition in oval defects.

Contents

1 Introduction 1

1.1 Semiconductor physics on the nanometer scale 1

1.2 Nanostructure fabrication 3

1.3 Outline of the thesis 6

2 Optical fiber cathodoluminescence system 15

2.1 Introduction 15

2.2 Cathodoluminescence scanning electron microscopy 16

2.3 Collection of the cathodoluminescence signal 18

2.4 Cathodoluminescence apparatus and techniques 20

2.5 Liquid helium cold stage 24

2.6 Application of cathodoluminescence: Study of a TJS laser 28

3 Orientation selective epitaxy 38

3.1 Growth on patterned substrates 38

3.2 Growth of the crystal 39

3.3 Cathodoluminescence of AlGaAs in the groove 40

3.4 Transmission electron microscopy of a groove 44

3.5 Zinc diffusion induced disordering of the OSE superlattice 47

3.6 Discussion: Orientation selective epitaxy 49

3.7 Conclusions 51

4 Orientation selective epitaxy: Theory **57**

4.1 Introduction 57

4.2 Molecular beam epitaxy 59

4.2.1 Nucleation and growth 59

4.2.2 Kinetics of GaAs/AlGaAs growth 63

4.2.3 Monte Carlo simulation of MBE growth 65

4.3 Alloy growth in III-V epitaxy: Ordering and segregation 67

4.4 Migration enhanced epitaxy 71

4.4.1 Tilted superlattices 72

4.4.2 Coherent tilted superlattices 75

4.5 Orientation selective epitaxy 77

4.5.1 Surface chemistry 77

4.5.2 Geometry of MBE growth on nonplanar surfaces 78

4.5.3 Time dependent fluxes 79

4.5.4 Substrate rotation induced compositional modulation 81

4.5.5 Beat frequency compositional modulation 82

4.5.6 Orientation selective epitaxy and the OSE superlattice: Selective migration enhanced epitaxy 85

4.6 Monte Carlo simulation of orientation selective epitaxy 94
4.6.1 Parameters of the simulation 94
4.6.2 Simulation algorithm 97
4.6.3 Results of OSE simulations 100
4.7 Conclusions 107

5 Orientation selective epitaxy: Dependence on groove orientation 114
5.1 Introduction 114
5.2 Orientation selective epitaxy: Variation of groove orientation 115
5.2.1 Sample preparation 115
5.2.2 Orientation considerations 117
5.3 Cathodoluminescence of grooves: Dependence on surface orientation . 118
5.4 Transmission electron microscopy 123
5.5 Discussion 124

6 Orientation selective epitaxy in oval defects 130
6.1 Introduction 130
6.2 Oval defects in $Al_xGa_{1-x}As$ grown by MBE 131
6.3 Experimental results 133
6.3.1 Sample MBE 562 133
6.3.2 Sample MBE 775 135
6.3.3 Sample MBE 815 139
6.3.4 Sample NSI1 142
6.3.5 Sample NSI3 145

6.4 Discussion: Variation of composition of AlGaAs in oval defects 148

6.4.1 Orientation selective epitaxy in oval defects 148

6.4.2 Surface diffusion in oval defects grown at high temperature . . 150

6.5 Conclusions 151

List of Figures

2.1 Electron beam excitation of a sample 17

2.2 Schematic of cathodoluminescence system 21

2.3 Photograph of the optical fiber translation stage used for collection of cathodoluminescence in a scanning electron microscope 22

2.4 Cryogenic system for low temperature cathodoluminescence 26

2.5 Schematic diagram of the cryogenic feedthrough 27

2.6 Schematic diagram of the cold stage 29

2.7 Schematic diagram of a junction-up TJS laser 30

2.8 Secondary electron micrograph of a TJS laser 32

2.9 Cathodoluminescence images of the TJS laser active region 33

2.10 Cathodoluminescence spectra of a TJS laser 35

3.1 Diagram of AlGaAs epilayers grown by molecular beam epitaxy on a nonplanar substrate 41

3.2 Cathodoluminescence images of a cross section of a groove 42

3.3 Cathodoluminescence spectra of the interface between the side and bottom facets of a groove 43

3.4 TEM micrograph of a cross section of the side facet of a groove . . . 45

3.5 TEM micrograph of the interface between the side and bottom facets of a groove 46

3.6 Calculation of the effect of compositional modulation on the effective bandgap energy in a superlattice, using the envelope function approximation. 50

4.1 MBE growth chamber 60

4.2 MBE growth by step flow and island nucleation 62

4.3 Shutter sequence used in migration enhanced epitaxial growth of GaAs 74

4.4 Deposition scheme for tilted superlattice growth 74

4.5 Deposition scheme for growth of a coherent tilted superlattice 76

4.6 Relative geometry of the effusion cells and the rotating substrate . . . 80

4.7 Beat frequency compositional modulation 84

4.8 Time dependent fluxes for a rotating, patterned substrate 87

4.9 Group III fluxes for growth on the (111) facets of a rotating (100) substrate 89

4.10 In-plane variation of the composition in orientation selective epitaxy . 90

4.11 Diagram showing deposition of an orientation selective epitaxy superlattice. 92

4.12 Monte Carlo simulation of the in-plane variation of the aluminum concentration 102

4.13 Comparison of Monte Carlo simulation with a calculation of the averaged fluxes . . . 103
4.14 Monte Carlo simulations at two different temperatures . . . 105
4.15 Monte Carlo simulation using time-independent fluxes . . . 106
5.1 Schematic diagram of fan pattern of grooves . . . 116
5.2 CL peak as a function of groove orientation . . . 119
5.3 TEM micrograph of growth on the (211) facet . . . 127
5.4 TEM micrograph of a quantum wire array . . . 128
6.1 CL images of oval defects in MBE 562 . . . 134
6.2 CL spectra of an oval defect in MBE 562 . . . 136
6.3 CL images of an oval defect in MBE 775 . . . 138
6.4 CL spectra of an oval defect in MBE 775 . . . 140
6.5 CL images of an oval defect in MBE 815 . . . 141
6.6 CL spectra of an oval defect in MBE 815 . . . 143
6.7 CL spectra from a second defect in MBE 815 . . . 144
6.8 CL spectra of an oval defect in NSI1 . . . 146
6.9 CL spectra from three oval defects in NSI3 . . . 147

Chapter 1

Introduction

1.1 Semiconductor physics on the nanometer scale

Electrons in solids occupy energy states which form essentially continuous bands, as opposed to discrete states in atoms and molecules. In conceiving of the smallest possible device, properties of systems in some intermediate size regime must be considered. A transition from classical[1] to quantum behavior of electrons in crystals takes place when the size of the crystal becomes comparable to the deBroglie wavelength of electrons. This critical size is a function of the effective masses of electrons and holes, and the temperature [2,3].

In the nanometer size regime, quantization of electronic states and coherent effects in electron transport modify the optical and transport properties of the crystal. Such quantum size effects have observable macroscopic consequences for the behavior of

[1]Classical, in this sense, refers to semiconductor systems which behave according to the energy level schemes laid out by Shockley in *Electrons and holes in semiconductors* [1].

devices. Examples of this in electron transport include the quantum hall effect [4,5], quantum transport [6], and the Aharonov-Bohm effect [7,8], and in optical properties of semiconductors, the quantum confined Stark effect [9]. These effects have been observed in GaAs/AlGaAs heterostructures [5,6,8,9].

The effect of quantum confinement on electronic energy states can be calculated within the envelope function approximation. This assumes that the total potential can be modelled by a periodic potential due to an infinite crystal lattice, with a superimposed slowly varying potential describing the effect of the nanometer scale heterostructure. While a rigorous treatment of the problem requires a multiband approach [10], several qualitative effects of quantum confinement are predicted by a simple one-band effective mass calculation[2]. In this approximation, the envelope function and eigenenergy of an electron at zone center (crystal momentum $\vec{k} = 0$) are calculated using an effective mass Schrödinger equation,

$$[-\frac{\hbar^2}{2}\vec{\nabla} \cdot (\frac{1}{m^*(\vec{r})}\vec{\nabla}) + V(\vec{r})]\Psi(\vec{r}) = (E - E_0)\Psi(\vec{r}), \tag{1.1}$$

in which the potential, $V(\vec{r})$, is given by the band offsets in the heterostructure, E_0 is the position of the relevant band edge, and $m^*(\vec{r})$ is the effective mass (given by the curvature of the band at $\vec{k} = 0$) [12,13]. In particular, equation (1.1) assumes that the electron energy in the crystal near the zone center is a parabolic function of the crystal momentum, $\vec{k}$.

Increasing singularity of the density of states for higher dimensional confinement

[2]Calculation of some of the effects of quantum confinement, such as polarization dependence of the optical matrix elements in quantum wires, requires the incorporation of band coupling effects, which are not accessible by the one-band model discussed herein [11].

results in changes in the macroscopic properties of a crystal containing arrays of nanostructures. A semiconductor laser with such a crystal in the active region is predicted to have decreased sensitivity to temperature, lower threshold current density, reduced linewidth, and increased modulation speed [2,3,14,15]. Other applications of quantum confinement in optoelectronic devices include short-pulse light sources, optical switches in cavities, high speed optical modulators, self electro-optic devices, and high gain avalanche photodetectors [16]. Furthermore, control over macroscopic crystal properties afforded by nanometer scale bandgap engineering will certainly result in new, and unsuspected, applications in electronic and optoelectronic circuits and devices.

1.2 Nanostructure fabrication

Quantum states in thin GaAs layers were first observed in transport measurements in 1974, and in optical measurements shortly thereafter [17,18]. In 1975, a laser was fabricated with a multiple quantum well active region [19]. Rapid improvement of the crystal growth technology resulted in quantum well lasers with superior performance, operating at room temperature with low threshold current densities [20].

High quality quantum wells are routinely grown by molecular beam epitaxy (MBE) and organo-metallic vapor phase epitaxy (OMVPE). The technology for fabricating quantum wells has found application in a wide variety of devices, both optical and electronic in nature [16]. Fabrication of higher dimensional nanometer scale structures has proven to be much more difficult. Arakawa and Sakaki proposed a new type of

laser in 1982, which would constitute an application of such structures, later termed quantum wires (2D quantum well) and quantum dots (3D quantum well) [14]. Significant improvement in the dynamic and spectral characteristics of such quantum wire and quantum dot lasers are expected, based on the effect of quantum confinement on the electronic density of states [2,3,15].

In 1982, the first quantum wire structures were fabricated in a silicon accumulation layer, using electric field induced confinement in a field effect transistor [21]. Shortly thereafter, electron beam lithography and reactive ion etching were used to define narrow conducting channels ($\approx$ 1 μm wide) in a silicon inversion layer [22], anticipating by four years the use of this fabrication technology in the realization of quantum wire and dot heterostructures exhibiting optical evidence of quantized electronic states.

In order to realize the predicted benefits of quantization of electronic states for optical device applications, arrays of such structures must be fabricated with sufficient uniformity to overcome the loss in volume of luminescing material, relative to quantum wells of equivalent dimension [2,3]. In addition, the achievement of efficient luminescence is incompatible with damage, contamination, and surface states which are inherent in fabrication technologies employing ion beam implantation and dry etching. In order to obtain luminescence from structures fabricated by these techniques, surface passivation or annealing is generally done to eliminate some of the deep levels caused by the fabrication process.

The first optical studies of higher dimensional quantum confinement were done

with semiconductor crystallites in colloidal suspensions [23]. Optical spectra of the crystallites, with typical dimensions of 20-200Å, exhibited partly resolved discrete features, characteristic of spatial confinement in three dimensions. The data are also indicative of the importance of inhomogeneous broadening, impurity states, and surface states in nanometer scale structures.

In anticipation of future device applications, quantum wires were simulated in semiconductor lasers using high magnetic fields to obtain Lorentz confinement of electrons and holes [14,24,25,26]. Predicted improvements in the dynamic and spectral characteristics of quantum wire and quantum dot lasers were verified in these experiments.

Reports of optical studies of quantum wire and dot heterostructures first appeared in 1986 and 1987[3] [28,29,30,31]. All of these experiments used reactive ion etching or ion beam implantation. Initial reports of high luminescence intensity from nanometer scale structures [29] have not been verified in subsequent measurements, and fabrication induced damage continues to be a problem in these techniques. A more successful approach in this regard spatially separates the damage from the nanostructures, while retaining reactive ion etching for patterning, by using a strain-induced confinement potential [32].

The fabrication of higher dimensional semiconductor structures during crystal growth has several advantages over lithographic patterning techniques. These include fabrication in a single growth step, natural incorporation into device heterostructures,

[3] An earlier report of structures fabricated by a chemical etch did not provide conclusive evidence for quantum size effects, and only suggested such effects as one possible explanation of the observations [27].

and avoidance of fabrication induced damage. Recently, several techniques for *in situ* fabrication of nanometer scale structures have been introduced. Quantum wires and grid-inserted quantum wells were grown on vicinal substrates[4] using migration enhanced epitaxy[5] [33,34]. Quantum wires have been grown on grooves in a GaAs substrate, using orientation dependent growth rates to confine electrons in the lateral dimensions [35,36]. The first quantum wire laser was recently fabricated in growth on a patterned substrate, exemplifying the inherent advantages of *in situ* fabrication techniques [35].

1.3 Outline of the thesis

Orientation selective effects in the molecular beam epitaxial (MBE) growth of $Al_{1-x}Ga_xAs$ on a patterned (100) GaAs substrate are investigated. Under particular growth conditions, the spontaneous, selective formation of a superlattice or quantum wire array on the sides of grooves is observed. Experiments and modelling indicate that this growth technique, orientation selective epitaxy (OSE), has application to the *in situ* growth of nanometer scale structures.

An optical fiber cathodoluminescence system and liquid helium cold stage for a scanning electron microscope are described in Chapter 2. By using an optical fiber to directly collect light from the surface of the sample, spectrally resolved cathodolumi-

[4]Vicinal substrates are slightly misoriented from the exact crystallographic orientation. Misorientation results in the occurrence of steps on the surface, which are essential to the formation of the quantum wires.

[5]Migration enhanced epitaxy is a specialized form of molecular beam epitaxy, which utilizes alternating beam deposition of the constituents to enhance surface migration of atoms and molecules during growth.

nescence measurements can be done without precluding simultaneous measurement of other signals [37,38]. The system attains comparable performance to alternative systems which utilize concave mirrors for light collection. The application of cathodoluminescence to the analysis of heterostructures is demonstrated by data from a transverse junction stripe (TJS) laser.

Experimental results (Chapter 3) on the MBE growth of $Al_xGa_{1-x}As$ on $[01\bar{1}]$ grooves in a (100) GaAs substrate exhibit orientation selective effects [39]. Spontaneous growth of a superlattice is observed on the sides of grooves. The superlattice, with a period of approximately 70Å, exhibits strong luminescence, red-shifted by 127 meV from the emission of uniform $Al_{0.25}Ga_{0.75}As$ grown on adjacent facets. This is the first observation of compositional modulation in the growth of AlGaAs on a {111} surface. The abrupt termination of the superlattice at the interface with adjacent facets constitutes a heterojunction oriented lateral to the growth direction, the first such structure to be formed spontaneously during growth.

A model for orientation selective epitaxy is presented, based on the kinetics of MBE growth on a patterned substrate, and a Monte Carlo simulation of the growth is presented (Chapter 4). Large in-plane variations in the composition are predicted by the model, in agreement with the experiments. The implications of the model are discussed, regarding manipulation of OSE growth, application of OSE growth to bandgap engineering in two and three dimensions, and the extension of OSE growth to other heterostructure systems.

The dependence of OSE growth on surface orientation is investigated by varying

the groove orientation in a patterned (100) GaAs substrate (Chapter 5). Strong dependence of cathodoluminescence emission on groove orientation is observed. In some ranges of groove angles, monotonic dependence of the peak emission on groove orientation is observed, suggesting the possibility of bandgap tuning by variation of surface orientation. The observation of quantum wire-like structures in OSE growth demonstrates the potential of OSE growth for nanometer scale bandgap engineering in two and three dimensions [40].

A study of $Al_xGa_{1-x}As$ grown in oval defects by molecular beam epitaxy is presented in Chapter 6. A strong dependence of the composition on the orientation of growth in oval defects is observed [41]. Comparison with growth in grooves indicates that orientation selective epitaxy plays a role in determining the composition of $Al_xGa_{1-x}As$ in oval defects.

Bibliography

[1] William Shockley, *Electrons and Holes in Semiconductors, with applications to transistor electronics*, D. Van Nostrand Company, Inc., Princeton, New Jersey, 1950.

[2] Kerry J. Vahala, "Quantum Box Fabrication Tolerance and Size Limits in Semiconductors and Their Effect on Optical Gain," IEEE J. Quantum Electron., **QE-24**, 523 (1988).

[3] Hal Zarem, Kerry Vahala, and Amnon Yariv, "Gain Spectra of Quantum Wires With Inhomogeneous Broadening," J. Quantum Electron., **QE-25**, 705 (1989).

[4] K. v. Klitzing, G. Dorda, and M. Pepper, "New Method for High-Accuracy Determination of the Fine-Structure Constant Based on Quantized Hall Resistance," Phys. Rev. Lett., **45**, 494 (1980).

[5] D. C. Tsui and A. C. Gossard, "Resistance standard using quantization of the Hall resistance of GaAs-$Al_xGa_{1-x}As$ heterostructures," Appl. Phys. Lett., **38**, 550 (1981).

[6] M. L. Roukes, A. Scherer, S. J. Allen, Jr., H. G. Craighead, R. M. Ruthen,

E. D. Beebe, and J. P. Harbison, "Quenching of the Hall Effect in a One-Dimensional Wire," Phys. Rev. Lett., **59**, 3011 (1987).

[7] Y. Aharonov and D. Bohm, "Significance of Electromagnetic Potentials in the Quantum Theory," Phys. Rev., **115**, 485 (1959).

[8] A. Scherer, M. L. Roukes, H. G. Craighead, R. M. Ruthen, E. D. Beebe, and J. P. Harbison, "Ultranarrow conducting channels defined in GaAs-AlGaAs by low-energy ion damage," Appl. Phys. Lett., **51**, 2133 (1987).

[9] D. A. B. Miller, D. S. Chemla, T. C. Damen, A. C. Gossard, W. Wiegmann, T. H. Wood, and C. A. Burrus, "Electric field dependence of optical absorption near the band gap of quantum-well structures," Phys. Rev. B, **32**, 1043 (1985).

[10] Peter C. Sercel and Kerry J. Vahala, "An Analytical Formalism for Determining Quantum Wire and Quantum Dot Bandstructure in the Multiband Envelope Function Approximation," Phys. Rev. B, in press (1990).

[11] Peter C. Sercel and Kerry J. Vahala, "An analytical technique for determining the polarization dependence of optical matrix elements in quantum wires with band coupling effects," Appl. Phys. Lett., submitted for publication (1990).

[12] G. Bastard, "Superlattice band structure in the envelope-function approximation," Phys. Rev. B, **24**, 5693 (1981).

[13] Richard A. Morrow and Kenneth R. Brownstein, "Model effective-mass Hamiltonians for abrupt heterojunctions and the associated wave-function-matching conditions," Phys. Rev. B, **30**, 678 (1984).

[14] Y. Arakawa and H. Sakaki, "Multidimensional quantum well laser and temperature dependence of its threshold current," Appl. Phys. Lett., **40**, 939 (1982).

[15] Yasuhiko Arakawa, Kerry Vahala, and Amnon Yariv, "Quantum noise and dynamics in quantum well and quantum wire lasers," Appl. Phys. Lett., **45**, 950 (1984).

[16] Daniel S. Chemla, "Quantum wells for photonics," Physics Today, p. 57, May, 1985.

[17] L. L. Chang, L. Esaki, and R. Tsu, "Resonant tunneling in semiconductor double barriers," Appl. Phys. Lett., **24**, 593 (1974).

[18] R. Dingle, W. Wiegmann, and C. H. Henry, "Quantum States of Confined Carriers in Very Thin $Al_xGa_{1-x}As$-GaAs-$Al_xGa_{1-x}As$ Heterostructures," Phys. Rev. Lett., **33**, 827 (1974).

[19] J. P. van der Ziel, R. Dingle, R. C. Miller, W. Wiegmann, and W. A. Nordland, Jr., "Laser oscillation from quantum states in very thin GaAs-$Al_{0.2}Ga_{0.8}As$ multilayer structures," Appl. Phys. Lett., **26**, 463 (1975).

[20] W. T. Tsang, "A graded-index waveguide separate-confinement laser with very low threshold and a narrow Gaussian beam," Appl. Phys. Lett., **39**, 134 (1981).

[21] A. B. Fowler, A. Hartstein, and R. A. Webb, "Conductance in Restricted-Dimensionality Accumulation Layers," Phys. Rev. Lett., **48**, 196 (1982).

[22] W. J. Skocpol, L. D. Jackel, E. L. Hu, R. E. Howard, and L. A. Fetter, "One-

Dimensional Localization and Interaction Effects in Narrow (0.1-μm) Silicon Inversion Layers," Phys. Rev. Lett., **49**, 951 (1982).

[23] Louis Brus, "Zero-Dimensional 'Excitons' in Semiconductor Clusters," IEEE J. Quantum Electron., **QE-22**, 1909 (1986).

[24] Y. Arakawa, K. Vahala, A. Yariv, and K. Lau, "Enhanced modulation bandwidth of GaAlAs double heterostructure lasers in high magnetic fields: Dynamic response with quantum wire effects," Appl. Phys. Lett., **47**, 1142 (1985).

[25] Y. Arakawa, K. Vahala, A. Yariv, and K. Lau, "Reduction of the spectral linewidth of semiconductor lasers with quantum wire effects - Spectral properties of GaAlAs double heterostructure lasers in high magnetic fields," Appl. Phys. Lett., **48**, 384 (1986).

[26] Kerry Vahala, Yasuhiko Arakawa, and Amnon Yariv, "Reduction of the field spectrum linewidth of a multiple quantum well laser in a high magnetic field - spectral properties of quantum dot lasers," Appl. Phys. Lett., **50**, 365 (1987).

[27] P. M. Petroff, A. C. Gossard, R. A. Logan, and W. Wiegmann, "Toward quantum well wires: Fabrication and optical properties," Appl. Phys. Lett., **41**, 635 (1982).

[28] M. A. Reed, R. T. Bate, K. Bradshaw, W. M. Duncan, W. R. Frensley, J. W. Lee, and H. D. Shih, "Spatial quantization in GaAs-AlGaAs multiple quantum dots," J. Vac. Sci. Technol. B, **4**, 358 (1986).

[29] K. Kash, A. Scherer, J. M. Worlock, H. G. Craighead, and M. C. Tamargo, "Optical spectroscopy of ultrasmall structures etched from quantum wells,"

Appl. Phys. Lett., **49**, 1043 (1986).

[30] J. Cibert, P. M. Petroff, G. J. Dolan, S. J. Pearton, A. C. Gossard, and J. H. English, "Optically detected carrier confinement to one and zero dimension in GaAs quantum well wires and boxes," Appl. Phys. Lett., **49**, 1275 (1986).

[31] H. Temkin, G. J. Dolan, M. B. Panish, and S. N. G. Chu, "Low-temperature photoluminescence from InGaAs/InP quantum wires and boxes," Appl. Phys. Lett., **50**, 413 (1987).

[32] K. Kash, J. M. Worlock, M. D. Sturge, P. Grabbe, J. P. Harbison, A. Scherer, and P. S. D. Lin, "Strain-induced lateral confinement of excitons in GaAs-AlGaAs quantum well microstructures," Appl. Phys. Lett., **53**, 782 (1988).

[33] Masaaki Tanaka and Hiroyuki Sakaki, "Formation of planar superlattice states in new grid-inserted quantum well structures," Appl. Phys. Lett., **54**, 1326 (1989).

[34] M. Tsuchiya, P. M. Petroff, and L. A. Coldren, "Spontaneous growth of coherent tilted superlattice on vicinal (100)GaAs substrates," Appl. Phys. Lett. **54** 1690 (1989).

[35] E. Kapon, D. M. Hwang, and R. Bhat, "Stimulated Emission in Semiconductor Quantum Wire Heterostructures," **63**, 430 (1989).

[36] Keisuke Kojima, Kazumasa Mitsunaga, and Kazuo Kyuma, "Fabrication and characterization of quantum well wires grown on corrugated GaAs substrates by molecular beam epitaxy," Appl. Phys. Lett., **56**, 154 (1990).

[37] Michael E. Hoenk and Kerry J. Vahala, "Cathodoluminescence system for a scanning electron microscope using an optical fiber for light collection," Rev. Sci. Instrum., **60**, 226 (1989).

[38] Michael E. Hoenk and Kerry J. Vahala, "Cathodoluminescence and Transmission Electron Microscopy of an Abrupt Lateral Junction in AlGaAs Grown by Molecular Beam Epitaxy," Scanning, **11**, 191 (1989).

[39] Michael E. Hoenk, C. W. Nieh, Howard Z. Chen, and Kerry J. Vahala, "Compositional modulation in $Al_xGa_{1-x}As$ epilayers grown by molecular beam epitaxy on the (111) facets of grooves in a nonplanar substrate," Appl. Phys. Lett., **55**, 53 (1989).

[40] M. E. Hoenk and K. J. Vahala, "Spontaneous selective epitaxial growth of compositionally modulated AlGaAs with an orientation dependent bandgap," *Advances in Semiconductors and Superconductors: Physics Toward Device Applications*, invited paper 1285-19, San Diego, CA, March 17-21, 1990.

[41] Michael E. Hoenk and Kerry J. Vahala, "Cathodoluminescence of oval defects in $GaAs/Al_xGa_{1-x}As$ epilayers using an optical fiber light collection system," Appl. Phys. Lett., **53**, 2062 (1988).

Chapter 2

Optical fiber cathodoluminescence system

2.1 Introduction

In order to study ultrasmall structures, analysis tools with a high degree of spatial resolution are required. Cathodoluminescence scanning electron microscopy[1](CL) is well suited to measurements of spectral emission of small structures in direct gap semiconductors [1]. The power of cathodoluminescence analysis is augmented by information obtained concurrently by the detection of other signals generated by the electron beam. This capability is sacrificed to a large degree by cathodoluminescence systems which restrict access to the sample in order to collect light from a large solid angle (using, for example, an elliptical mirror for light collection). A system with

[1]Cathodoluminescence is the emission of light from a material as a result of excitation by an electron beam.

comparable performance, but which does not compromise the use of other detectors, would have an important advantage over elliptical mirror collection.

In this chapter, we report the development of a novel cathodoluminescence system, which uses an optical fiber for direct collection of light from the surface of the sample. The system is capable of simultaneous operation with other imaging apparatus, without sacrificing performance. Techniques for generating spectrally resolved cathodoluminescence (SRCL) images and local CL spectra are discussed, and the application of this system is demonstrated by a study of a transverse junction stripe (TJS) laser.

2.2 Cathodoluminescence scanning electron microscopy

A scanning electron microscope generates a beam of electrons which is focused to a small spot on the sample surface (see Figure 2.1). The beam is swept across an area of the sample in a raster pattern. In the conventional mode of operation, the image is formed by detecting the emission of secondary electrons from the sample surface, and electronically correlating the secondary electron signal with the position of the beam. Other signals, carrying different information about the sample, can also be used for image formation. For example, a backscattered electron detector produces an image which is sensitive to variations in the material composition of the surface.

The electron beam induces a variety of excitations that result in emitted radiation. In particular, electron-hole pairs are produced in the interaction volume of the electron beam with the sample. The carriers generated by this process exist for a time

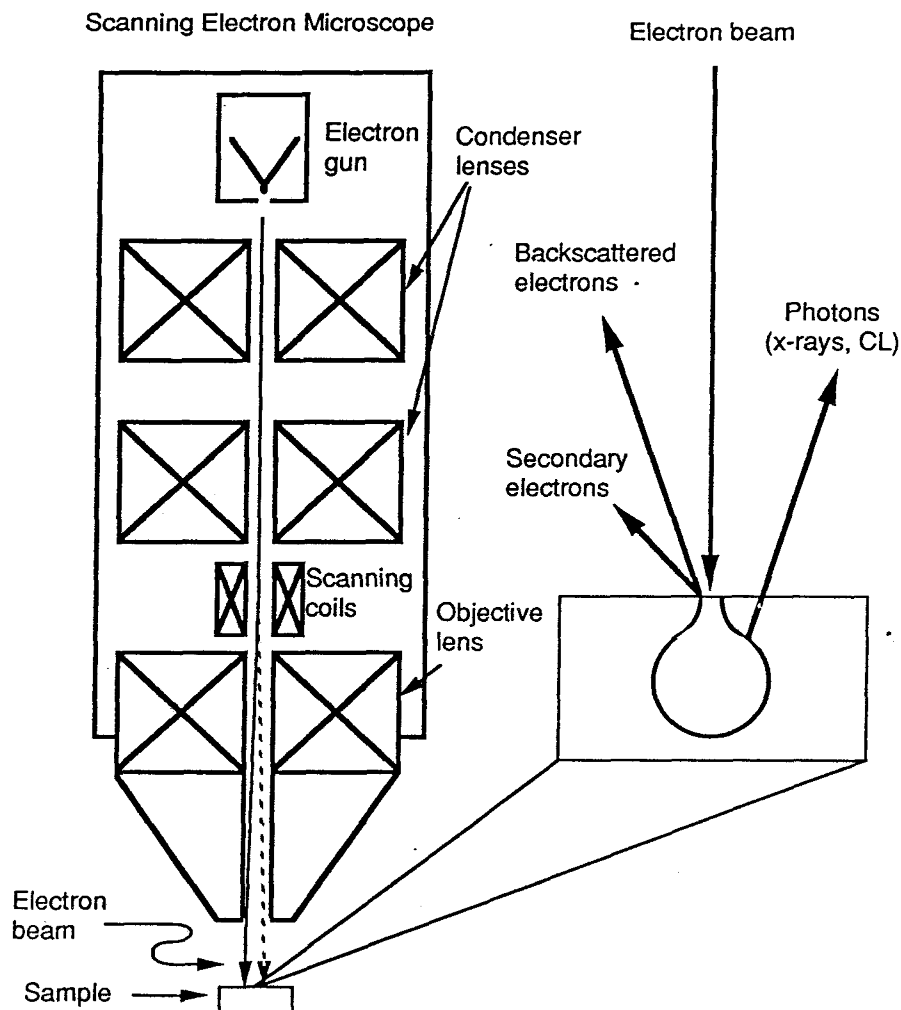

Figure 2.1: Schematic diagram of electron beam excitation of a sample. The scanning electron microscope column is illustrated on the left, with the electron beam originating at the filament and passing through the two condenser lenses, the scanning coils, and the objective lens, finally impinging on the sample as a fine probe. On the right, the interaction of the electron beam with the sample is illustrated, showing the interaction volume, and some of the products of the interaction.

characteristic of the material before recombining. Recombination can be accompanied by the emission of a photon, particularly in the case of direct gap semiconductors. The light generated by this process (cathodoluminescence) carries information about energy states near the bandgap. Cathodoluminescence images and spectra can be used to study the local properties of the material, and the results can be correlated with information from other SEM imaging techniques.

The diameter of the beam at the surface of the sample is on the order of 100Å. High energy electrons penetrate the surface, dissipating their energy within the interaction volume. The size of the interaction volume depends on the energy of the beam and the composition of the sample. In GaAs, the penetration depth of a $10keV$ electron beam is about 0.5 μm. Some of the dissipated energy is spent in the generation of electron-hole pairs within this volume, which undergo intraband relaxation and diffusion/drift before recombining. The diffusion length in a semiconductor depends on the lifetime, which is sensitive to, for example, the presence of dopants. A typical value for the electron diffusion length in GaAs is 1 μm. Thus, the spatial resolution of cathodoluminescence measurements in bulk GaAs is limited to length scales on the order of one micron[2].

2.3 Collection of the cathodoluminescence signal

For many applications of importance, the available cathodoluminescence signal is quite weak. For this reason, a CL collection system must be as efficient as possible.

[2] Recently, efforts by other groups to improve this value, using time-resolved spectroscopy and high magnetic fields, have resulted in spatial resolution of approximately 0.1 μm.

The two important factors which determine the collection efficiency are the solid angle subtended by the collection apparatus, and the efficiency with which light is guided to the detector.

Systems which include wavelength dispersive elements for spectral resolution of the CL signal (e.g., a monochromator) require that the detector be located outside of the sample chamber. In order to guide the light out of the chamber, the collection optics either directs the light toward a window in the chamber or into a light pipe leading to the detection apparatus. In work reported to date, light collection systems for cathodoluminescence with a scanning electron microscope [2,3,4,5] and a scanning transmission electron microscope [6,7,8] have used collection optics with concave mirrors, planar mirrors, lenses, or some combination of these elements. Concave mirrors, while achieving the goal of subtending a large solid angle, restrict access to the sample. This limits the capabilities of the microscope when the mirror is in place by preventing detection of other signals from the sample.

The system which we have designed minimizes any restriction of access to the sample. Although the solid angle subtended by our collection system is smaller than can be achieved with a concave mirror, our efficiency in guiding the collected light to the detector is excellent. Comparison of our data with the literature indicates that our overall collection efficiency is comparable to the efficiency of systems utilizing a concave mirror. Steyn et al. have studied in detail the problem of optimizing the collection efficiency [3]. Using an elliptical mirror, they were able to collect as much as 86% of light emitted into 2π sr. However, the solid angle of collection is not the only

figure of merit for the efficiency of a cathodoluminescence system. Steyn et al. found that, using an optimized elliptical mirror system, only 1% of the light was guided to the entrance slit of the monochromator. Furthermore, efficient collection could only be obtained from an area of the sample approximately 10-100 μm on a side.

With the fiber at its optimum position, our system collects 2% of the light emitted into 2π sr. The fiber guides this light to the entrance slit of the monochromator with excellent efficiency, because there are few optical surfaces between the fiber and the monochromator, and the fiber losses are negligible. Light is collected efficiently from an area of the sample approximately 200 μm in diameter. Thus, without sacrificing performance, we have built a light collection system which retains maximal access to the sample for other detectors.

2.4 Cathodoluminescence apparatus and techniques

We have developed a novel optical fiber light collection system which is compact, inexpensive, and versatile (see Figure 2.2). A single optical fiber, mounted to a three axis translation stage, collects cathodoluminescence directly from the surface of the sample (see Figure 2.3). In addition to being compatible with concurrent operation of other detectors (e.g., x-ray and backscattered electron detectors), the system provides an independent, externally controlled translation stage which is adaptable for other applications [9]. The fiber manipulator can be installed without modification to the existing stage in the microscope, and it is fully retractable when not in use.

The system was designed for incorporation into the sample chamber of a scanning

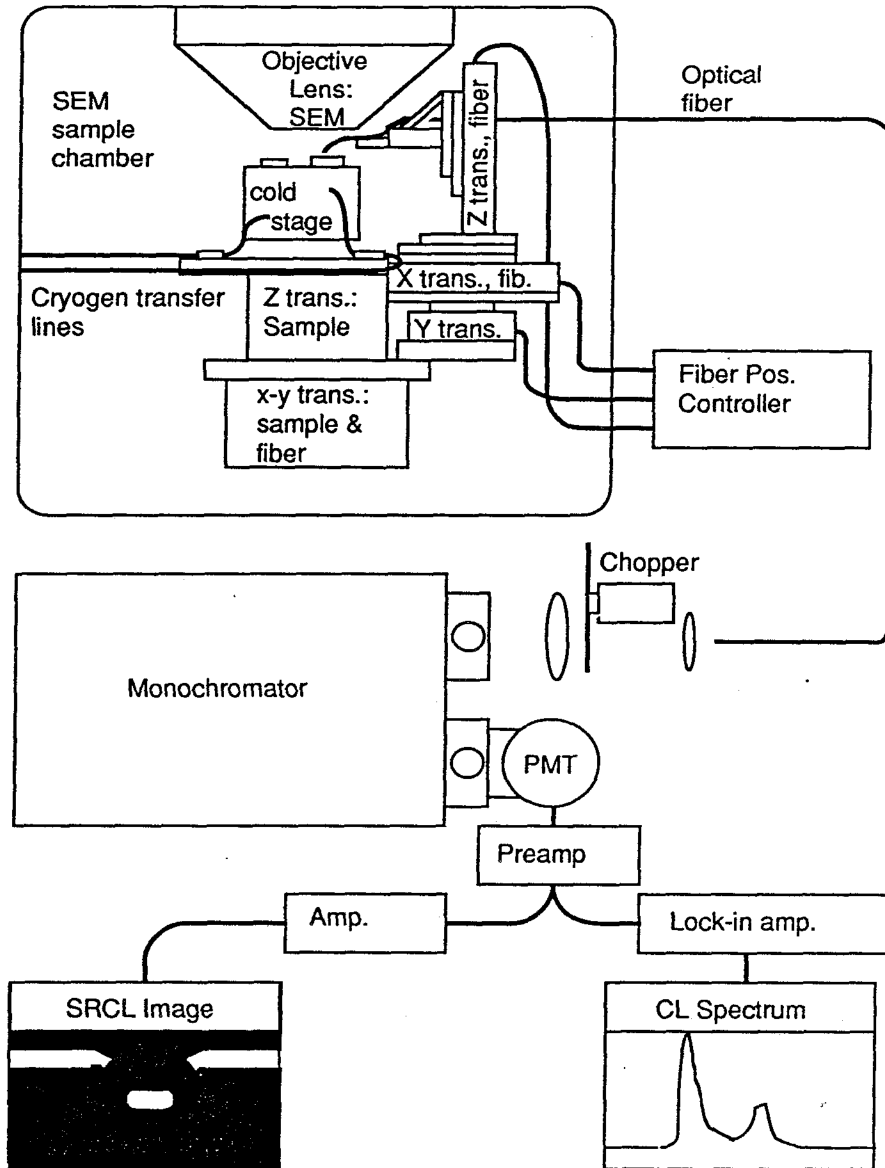

Figure 2.2: Schematic diagram of the experimental apparatus. The box at the top of the figure shows the optical fiber cathodoluminescence collection system as it appears inside the scanning electron microscope chamber. The lower half of the diagram is a schematic representation of the apparatus for producing cathodoluminescence images and spectra.

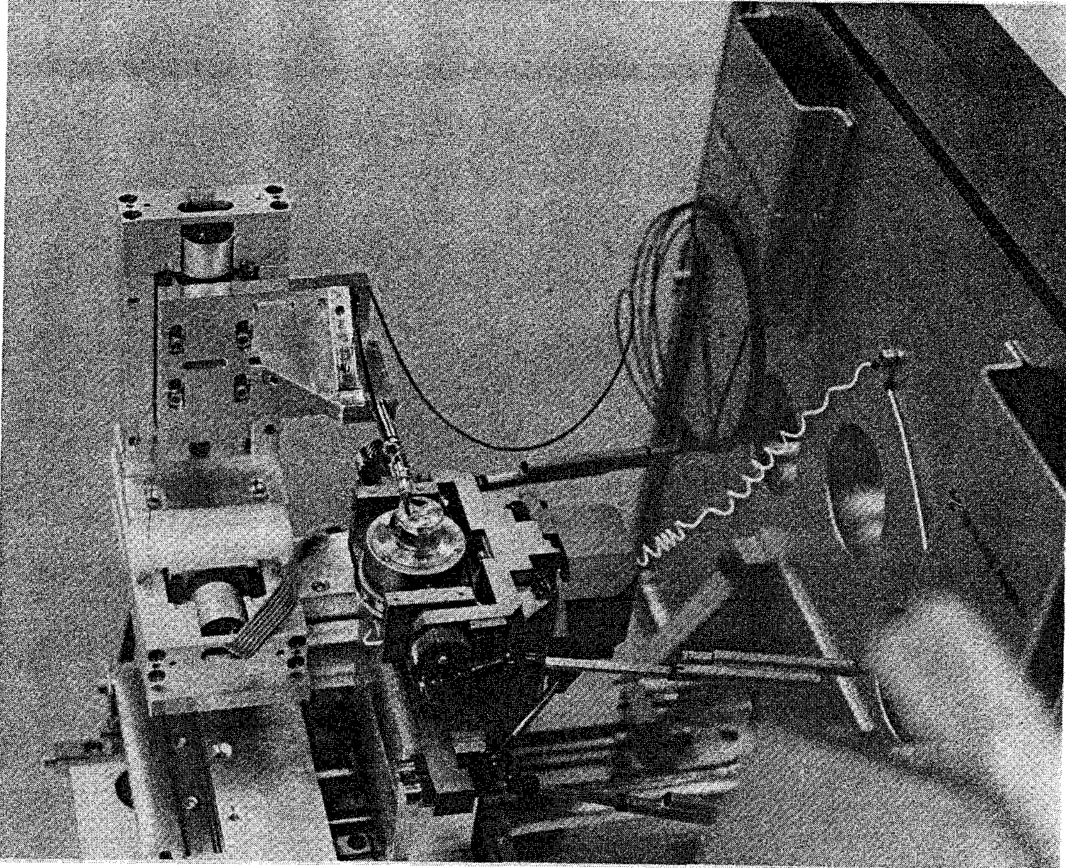

Figure 2.3: Photograph of the optical fiber translation stage used for collection of cathodoluminescence in a scanning electron microscope. A single optical fiber, mounted to a motorized, three-axis translation stage, is held within 0.5 mm of the sample.

electron microscope (see Figure 2.2). An optical fiber is used for direct collection of light from the surface of the sample. The numerical aperture of the fiber is 0.2, and the diameter of the core is 200 μm. Thus, for maximum collection efficiency, the fiber should be held 0.5 mm from the point of excitation. To prevent distortion of the image due to charging of the fiber, the fiber is shielded from the electron beam by a metal sheath, and the facet is coated with a thin layer of gold/palladium (< 50Å). The sheath consists of a $\frac{1}{16}$ in thin-walled stainless steel tube. The sheath is attached to the arm of a low profile mount, which extends from the three axis translation stage to a position adjacent to the sample, between the objective lens of the scanning electron microscope and the sample mount. This design allows a minimum working distance of $9mm$ between the sample and the objective lens. Positioning of the fiber is accomplished with three motorized translation stages, mounted to the x-y translation stage of the microscope. This allows the position of the fiber relative to the sample to be adjusted during operation of the cathodoluminescence system, and it provides the ability to retract the fiber.

The collected light is guided from under the objective lens of the SEM , through a vacuum feedthrough mounted to the door of the sample chamber. Exiting the far facet of the optical fiber, the light is focused onto the entrance slit of a monochromator. The CL intensity at the selected wavelength is detected with a cooled photomultiplier tube (PMT).

The signal from the PMT can be used to generate a spectrally resolved cathodoluminescence (SRCL) image (see Figure 2.2). This is accomplished by amplifying the

PMT signal and connecting it to the auxilliary input of the SEM. The SEM video electronics generate the SRCL image and display it on the video monitor. All of the image processing electronics of the SEM are available for manipulation of the SRCL image. The SRCL image can be compared directly with any of the other types of images which the SEM can produce. Especially useful is the signal mixing function (Cambridge S240 SEM), which allows the secondary electron image to be superimposed on the SRCL image. The noise can be reduced by slowing the scan rate of the electron beam and using a digital image store device to average the signal. SRCL micrographs can be taken with the video camera of the SEM.

By using the electron beam for local excitation and scanning the monochromator through an interesting region of the spectrum, local CL spectra can be measured (see Figure 2.2). Any point on the sample can be selected for local excitation, using either the secondary electron image or the SRCL image for determination of the area of interest. Reduction of the photomultiplier noise in local spectra is accomplished by lock-in detection, using a mechanical light chopper to modulate the signal. The scan is initiated by the computer, which collects digitized data from the lock-in amplifier.

2.5 Liquid helium cold stage

We have designed and built a compact cold stage for low temperature cathodoluminescence studies. The cryogenic system, which is capable of operating with a continuous flow of liquid nitrogen or liquid helium, consists of a commercially available transfer line, a right angle adapter for feedthrough of the cryogen into the vacuum system,

and a cold stage (see Figure 2.4). Cryogen, either liquid nitrogen or liquid helium, is supplied from a tank through the transfer line, and vented to atmosphere. Transfer is driven by pressure in the tank.

The adaptor is mounted to the transfer line with an indium seal, feeding the cryogen into a stainless steel tube ($\frac{1}{16}$ in outer diameter) inside the vacuum system (see Figure 2.5). The adaptor is designed to minimize transfer of heat from the room temperature flange and the ambient air to the cryogen flowing into the vacuum chamber. The transfer line is evacuated and insulated. In addition, the transfer line is inserted coaxially into a long, thin-walled stainless steel tube, which also serves as the passageway for the cold gas return. This minimizes thermal conduction to the end of the transfer line, and allows the returning cryogen to precool the outer jacket of the transfer line for more efficient cool down. This assembly is inserted coaxially into another stainless steel tube, which is bent by 90° and attached at one end to the vacuum flange, and sealed at the other end, so that the outer tube can be evacuated. Spacers, where required, are made from delrin, which minimizes thermal conduction and is compatible with the high vacuum environment.

The $\frac{1}{16}$ in thin-walled stainless steel tubes which carry cryogen to and from the cold stage are wrapped in several layers of aluminized mylar, to minimize radiative heating of the transfer lines in the vacuum system. Connection of lines from the adaptor to the lines from the cold stage is accomplished with VCR couplings and metal gaskets, which are compatible with cryogenic operation. Other than this coupling, all connections are welded or brazed to allow for cycling of the temperature.

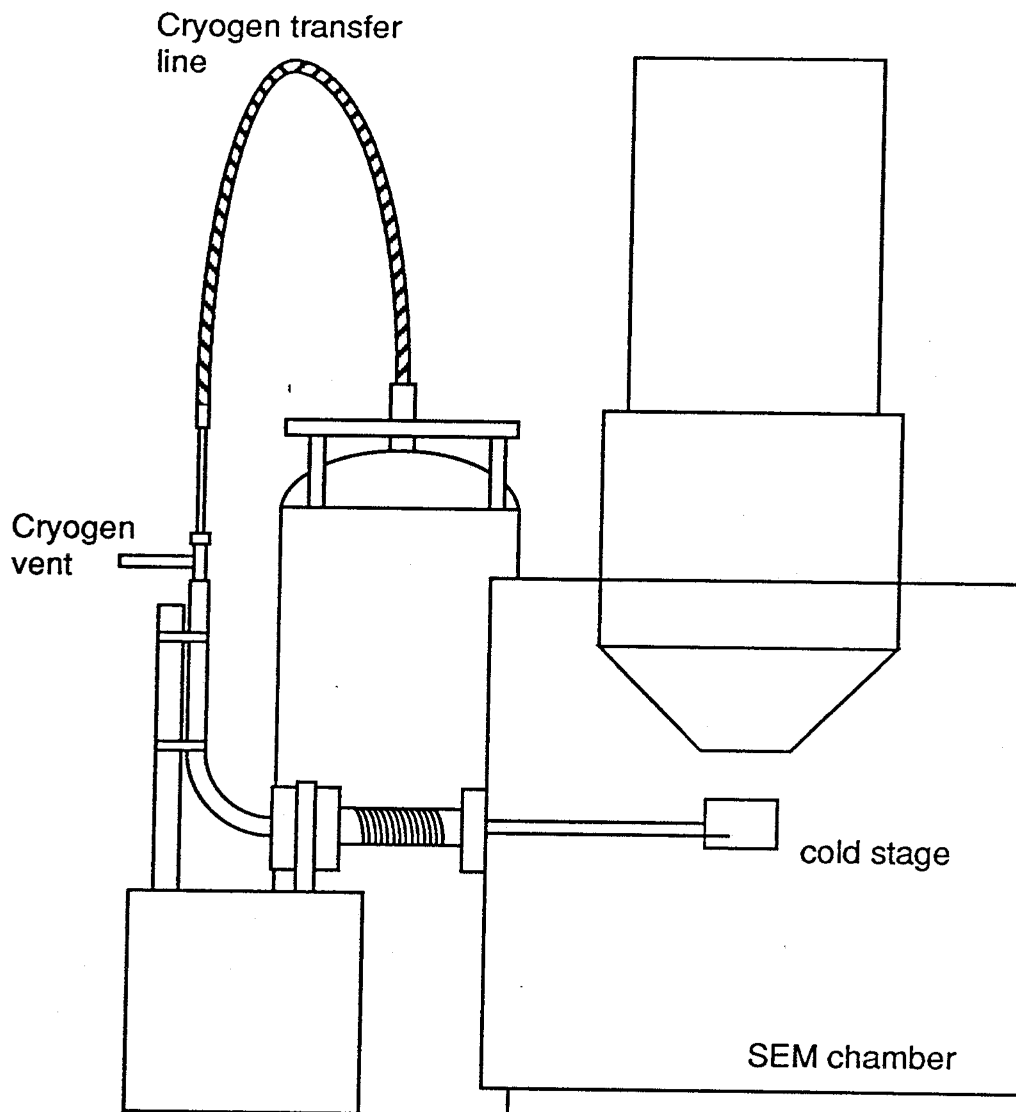

Figure 2.4: Schematic representation of the cryogenic system for low temperature cathodoluminescence. Cryogen from the tank flows continuously through the cold stage inside the sample chamber. The cryogenic feedthrough into the vacuum system is accomplished by an adaptor, which provides sufficient thermal isolation of the flowing cryogen to operate the cold stage with liquid helium.

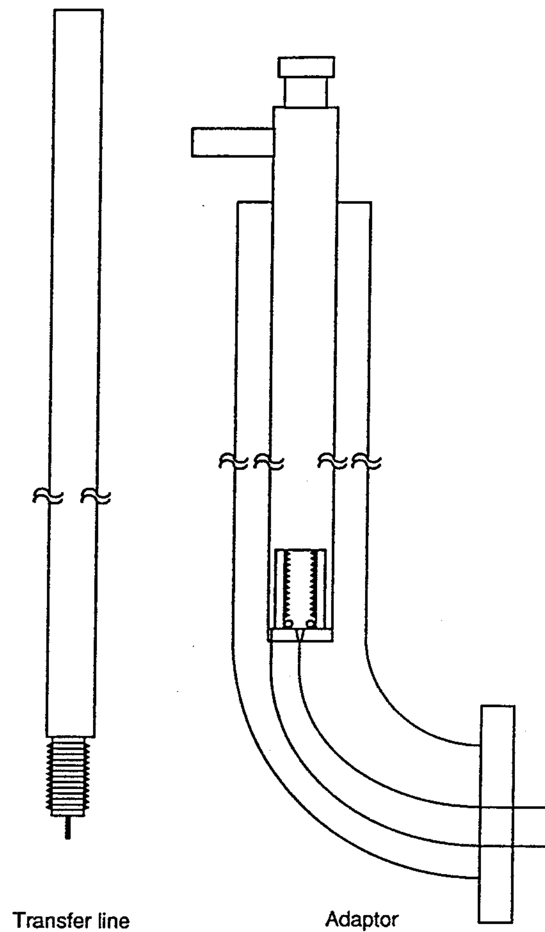

Figure 2.5: Schematic diagram of the cryogenic feedthrough. Thermal isolation of the flowing cryogen is accomplished by four coaxial stainless steel tubes. The inner tube contains the flowing cryogen, and is separated from the outer jacket of the transfer line by a high vacuum ($\approx 10^{-8}$ torr). The inner tube of the adaptor consists of a long, thin-walled stainless steel tube, which provides minimal thermal conduction along its length. Between the inner tube of the adaptor and the outer tube of the transfer line, the returning cryogen flows out of the system, allowing for better isolation and more efficient cool-down. The outer tube of the adaptor is evacuated, minimizing thermal conduction to the cold inner tube.

The cold stage consists of a hollow cylinder of oxygen-free high conductivity (OFHC) copper, which is filled with copper foam for more efficient transfer of heat to the cryogen and brazed closed (see Figure 2.6). The transfer lines are brazed to the cold stage, for continuous flow of cryogen during operation. Several tapped holes are machined into the top of the cold stage, for attachment of the sample holder, the heater, and the temperature sensor.

2.6 Application of cathodoluminescence: Study of a TJS laser

The cathodoluminescence system described in this chapter has been a valuable tool in the experiments which comprise the remainder of this thesis. In order to illustrate the power of cathodoluminescence analysis of heterostructures, results of measurements on a failed semiconductor laser are presented in this section. The laser, shown schematically in Figure 2.7, is a transverse junction stripe (TJS) laser, of the junction-up type [10,11,12,13]. The device consists of a Te-doped (n-type) epitaxial GaAs/AlGaAs heterostructure, grown by liquid phase epitaxy on a Cr-doped GaAs substrate. The layer structure consists of an $Al_xGa_{1-x}As$ active layer, approximately 0.2 μm thick, sandwiched between two Al_yGa_{1-y} layers. The active region is the p-type region of a p^+-p-n junction in the $Al_xGa_{1-x}As$ layer, defined by a two step zinc diffusion. Ohmic contacts are made to the surface of the device, straddling the p^+-p-n junction, so that carriers can be injected into the active region by forward-biasing the laser diode.

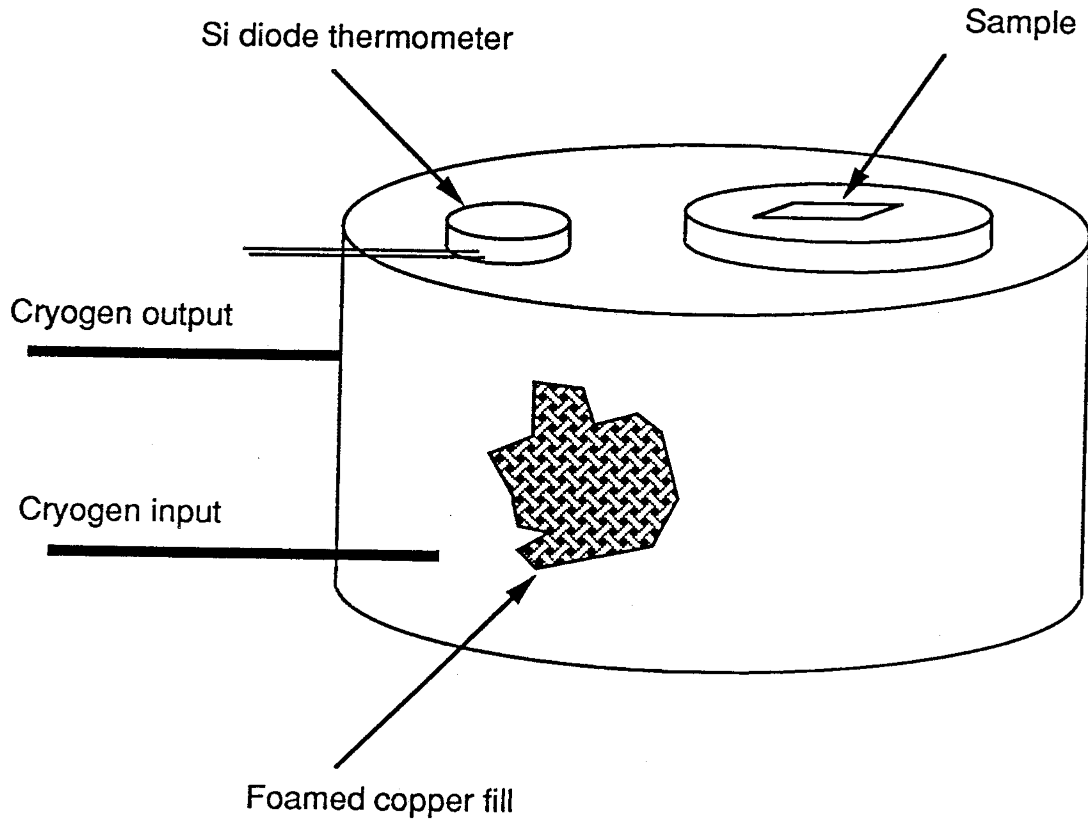

Figure 2.6: Schematic diagram of the cold stage. Cryogen flows into and out of the cold stage through thin-walled stainless steel tubes, with a $\frac{1}{16}$ in outer diameter. The cold stage is made from a hollow cylinder of oxygen-free high conductivity (OFHC) copper, which is filled with copper foam for more efficient transfer of heat to the cryogen and brazed closed. Several tapped holes are machined into the top of the cold stage, for attachment of the sample holder, the heater, and the temperature sensor.

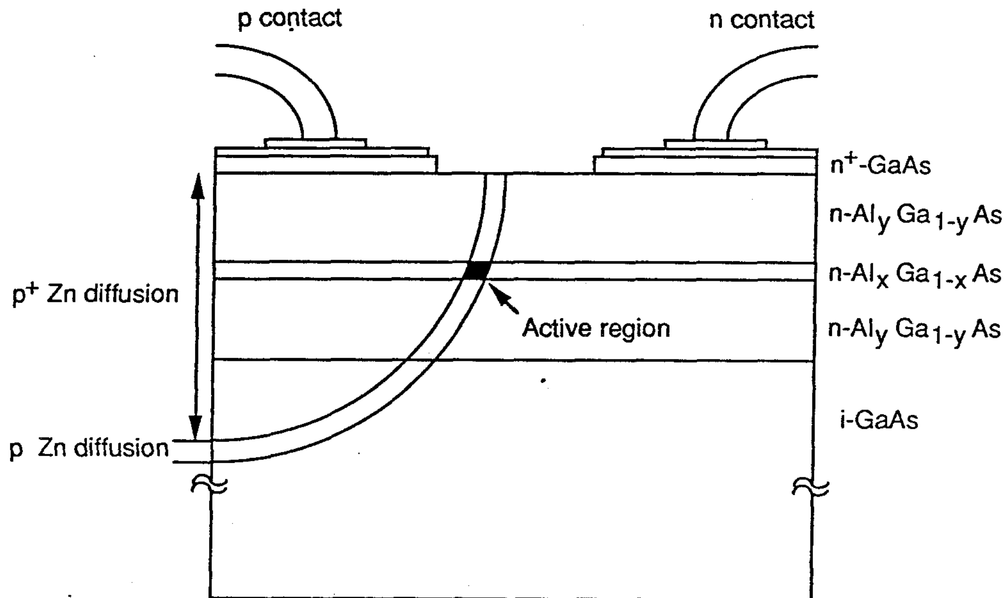

Figure 2.7: Schematic diagram of a junction-up TJS laser. The laser is formed by a two stage Zn diffusion into a four-layer heterostructure, grown by liquid phase epitaxy on a semi-insulating GaAs substrate. The active region is formed by the overlap of the Zn-doped p region with the $Al_xGa_{1-x}As$ layer. The contacts to the laser diode are on the top of the device.

Cathodoluminescence images of the TJS laser provide information about the spatial dependence of the luminescence, the position and dimensions of the diffusion front, and the location of the active region. Cathodoluminescence spectra provide information about the local composition, which can be correlated with the images to map out the structure.

A scanning electron micrograph of the device is shown in Figure 2.8. The laser was mounted on the cold stage of the cathodoluminescence system, oriented with the facet of the device facing the objective lens of the microscope. Excitation of the facet with the electron beam permitted a cathodoluminescence study of a cross section of the active region. Spectrally resolved cathodoluminescence images show the spatial pattern of luminescence from the device at several different wavelengths (see Figure 2.9). The cathodoluminescence images, taken at four different wavelengths, show the major features in the spectral emission of the laser diode. Strong luminescence at 7100Å is observed in the n-type region, in the vicinity of the active layer. At 7950Å, near the lasing wavelength, the active region of the device exhibits strong luminescence. At 8200Å, near the bandgap of GaAs at 77 K, luminescence is observed from the substrate, except in the zinc-diffused area. At 8450Å, strong luminescence is observed from the diffusion front, corresponding to a donor-acceptor transition in the highly doped material.

Information from the micrographs can be quantified by correlating it with cathodoluminescence spectra, taken using selective excitation of different areas of the laser. The areas of interest are chosen from the cathodoluminescence images. Three spec-

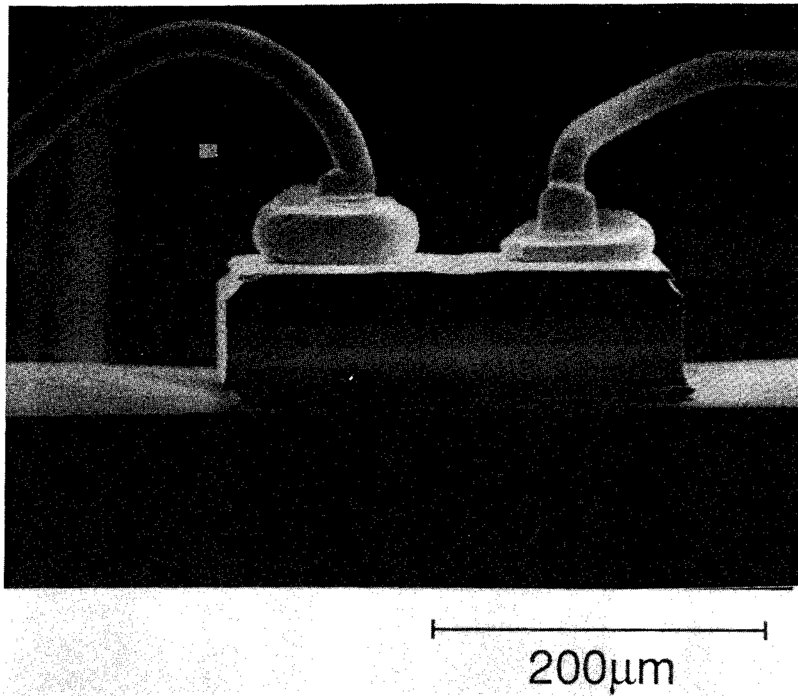

Figure 2.8: Secondary electron micrograph of the TJS laser, at low magnification. The laser is oriented so that the laser facet is in the plane of the micrograph, with the two gold leads located in the top portion of the micrograph. The active region of the laser is a stripe oriented orthogonally to the plane of the facet, located a few microns beneath the surface, between the gold leads.

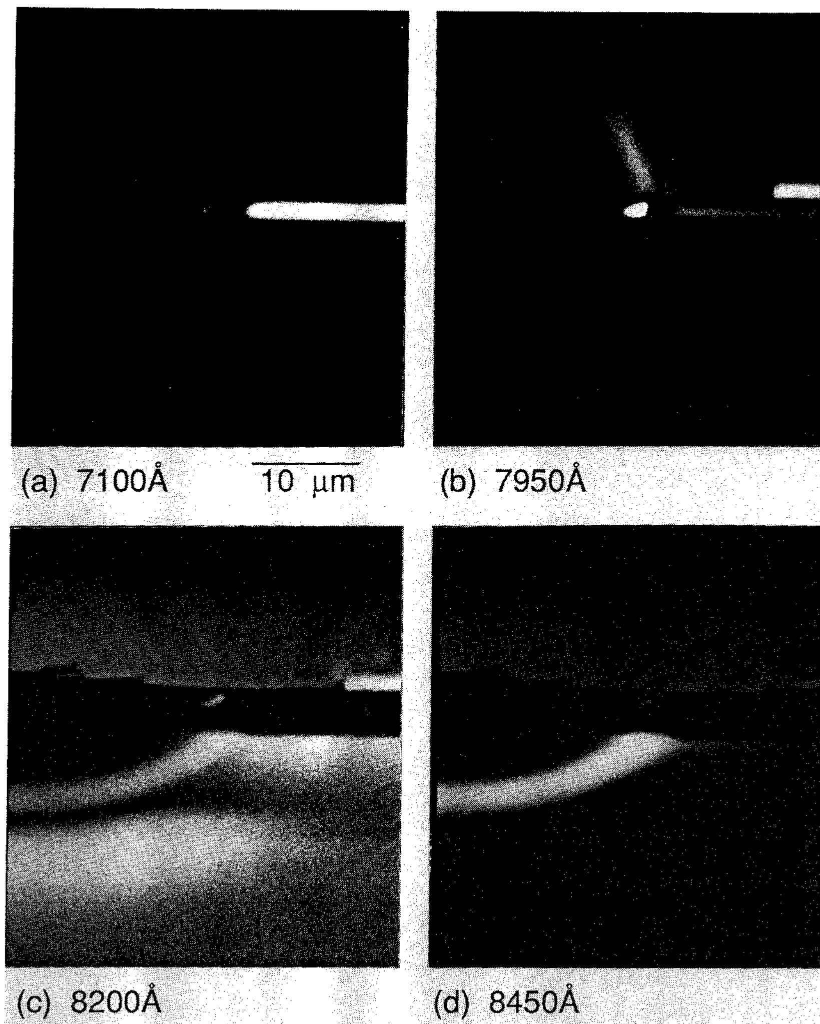

Figure 2.9: Spectrally resolved cathodoluminescence images of a cross section of the active region of a TJS laser, taken at 77 K, with a small admixture of the secondary electron signal for spatial reference. Information about the spatial dependence of the luminescence from the heterostructure can be obtained from these micrographs. The micrographs are taken at four different wavelengths, and show some of the main features in the luminescence from this structure.

tra are shown in Figure 2.10. The peaks near 6200Å correspond to the $Al_yGa_{1-y}As$ cladding layers in the waveguide, with $y \approx 0.36$. This peak is shifted in the active region, relative to the n-region of the active layer, due to the presence of a high concentration of zinc acceptors. Peaks near 8400Å correspond to donor to acceptor transitions in the GaAs substrate. The peak at 7921Å corresponds to the lasing transition in the $Al_xGa_{1-x}As$ region, with $x \approx 0.06$[3]. The origin of the peak at 7144Å in the n-type region of the active layer is not known.

[3] A small amount of aluminum is added to the active region to improve the reliability of the device.

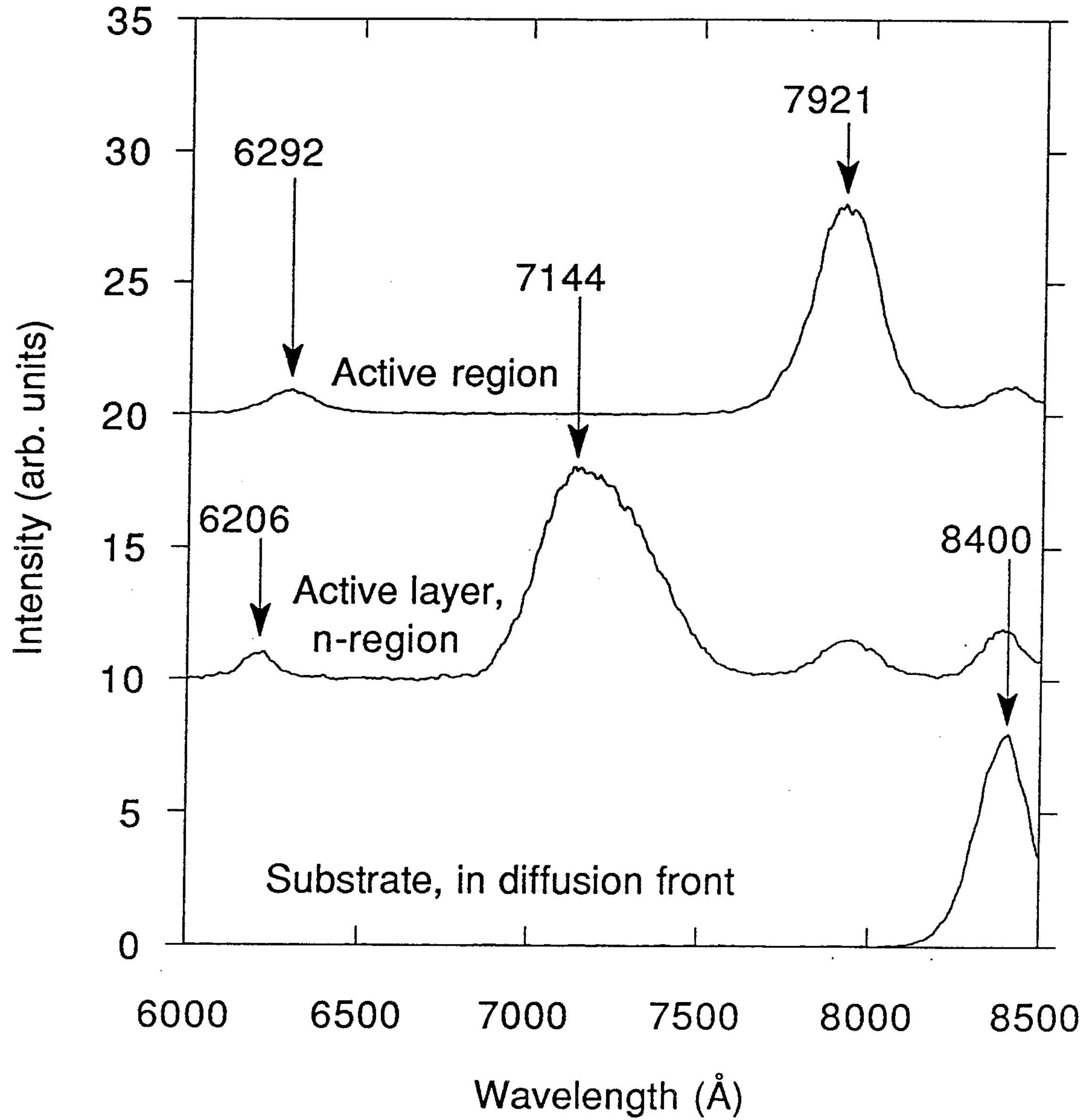

Figure 2.10: Cathodoluminescence spectra of a TJS laser at 77 K, taken with local excitation at various points in the laser structure.

Bibliography

[1] B. G. Yacobi and D. B. Holt, "Cathodoluminescence scanning electron microscopy of semiconductors," J. Appl. Phys., **59**, R1 (1986).

[2] E. M. Hörl, "Scanning electron microscopy of biological material using cathodoluminescence," Micron, **3**, 540 (1972).

[3] J. B. Steyn, P. Giles, and D. B. Holt, "An efficient spectroscopic detection system for cathodoluminescence mode scanning electron microscopy (SEM)," J. Microscopy, **107**, 107 (1976).

[4] S. M. Davidson and A. Rasul, "A high-resolution cathodoluminescence analysis system," J. Phys. E, **10**, 43 (1977).

[5] J. Beauvineau and J. Semo, "Improved spectrometer for cathodoluminescence studies in scanning electron microscopy," Rev. Sci. Instrum., **53**, 1573 (1982).

[6] P. M. Petroff, D. V. Lang, J. L. Strudel, and R. A. Logan, "Scanning transmission electron microscopy techniques for simultaneous electronic analysis and observation of defects in semiconductors," *Scanning Electron Microscopy/1978*, O. Johari, ed. (SEM Inc., Chicago, IL 60666), Vol. I, 325-352 (1978).

[7] S. Myhajlenko, "Near infrared cathodoluminescence assessment of semiconductors in a TEM," *Electron Microscopy and Analysis, 1983*, P. Doig, ed., Inst. Phys. Conf. Ser. No. 68 (Bristol, London: The Institute of Physics), 111 (1984).

[8] S. D. Berger and L. M. Brown, "Cathodoluminescence from dislocations in type II natural diamond," *Electron Microscopy and Analysis, 1983*, P. Doig, ed., Inst. Phys. Conf. Ser. No. 68 (Bristol, London: The Institute of Physics), 115 (1984).

[9] Peter C. Sercel, John A. Lebens, and Kerry J. Vahala, "Quantitative measurement of the composition of $Al_xGa_{1-x}As$ heterostructures using a simple backscattered electron detector," Rev. Sci. Instrum., **60**, 3775 (1989).

[10] Hirohumi Namizaki, Hisao Kumabe, and Wataru Susaki, "Spontaneous Emission Behavior in AlGaAs TJS Lasers," IEEE J. Quantum Electron., **QE-17**, 799 (1981).

[11] Shigeyuki Nita, Hirofumi Namizaki, Saburo Takamiya, and Wataru Susaki, "Single-Mode Junction-Up TJS Lasers with Estimated Lifetime of 10^6 Hours," IEEE J. Quantum Electron., **QE-15**, 1208 (1979).

[12] Hisao Kumabe, Toshio Tanaka, Hirofumi Namizaki, Makoto Ishii, and Wataru Susaki, "High temperature single-mode cw operation with a junction-up TJS laser," Appl. Phys. Lett, **33**, 38 (1978).

[13] Wataru Susaki, Toshio Tanaka, Hirofumi Kan, and Makoto Ishii, "New Structures of GaAlAs Lateral-Injection Laser for Low-Threshold and Single-Mode Operation," IEEE J. Quantum Electron., **QE-13**, 587 (1977).

Chapter 3

Orientation selective epitaxy

3.1 Growth on patterned substrates

Growth on a patterned substrate has been demonstrated to yield some lateral control of crystal composition. The promise of this technique in the fabrication of higher dimensional nanometer scale structures is exemplified by its use in the growth of the first quantum wire laser, using orientation dependent growth rates to define a single quantum wire at the bottom of a groove [1]. Recently, a lateral variation in the composition of $Al_xGa_{1-x}As$ grown over oriented grooves in a GaAs substrate has been observed [2,3,4,5]. Orientation selective epitaxy is a new phenomenon in growth on patterned substrates, in which the spontaneous, selective formation of a superlattice is observed [2]. This represents a new capability in crystal growth, with potential application for *in situ* growth of nanometer scale structures.

In this chapter, the phenomenon of orientation selective epitaxy will be introduced, and discussed for the case of growth on $[01\bar{1}]$ grooves in a GaAs substrate.

$Al_{0.25}Ga_{0.75}As$ epilayers were grown by molecular beam epitaxy on $[01\bar{1}]$ oriented grooves in a nonplanar (100) GaAs substrate. A quasi-periodic modulation of the aluminum concentration is observed to occur spontaneously in material grown on the sides of the grooves. The compositional modulation is associated with a reduction of the bandgap by 130 meV, with respect to that of the random alloy. While segregation of the AlGaAs alloy has been seen previously, this is the first observation of segregation of AlGaAs grown on a (111) surface. The compositional modulation terminates abruptly at the boundaries with adjacent facets in the groove, forming abrupt lateral junctions in the AlGaAs layers grown on a groove. This is the first observation of an abrupt lateral heterojunction formed spontaneously during crystal growth.

3.2 Growth of the crystal

Growth of the epilayers was done in a Riber 2300 molecular beam epitaxy machine, at a substrate temperature of 600°C. Grooves, approximately 15 μm wide, were etched parallel to the $[01\bar{1}]$ direction in an undoped, high resistivity GaAs (100) substrate. The substrate was rotated at 48 rpm during the growth. The structure in the unpatterned areas of the sample consists of a 1 μm GaAs buffer layer, a 1 μm $Al_{0.25}Ga_{0.75}As$ layer, a 100Å GaAs quantum well, and a 1000Å $Al_{0.25}Ga_{0.75}As$ cap layer. All layers are undoped. The quantum well was grown for a different purpose, and did not affect the results presented here. In order to verify this, cathodoluminescence measurements were done on a sample in which the quantum well had been removed with a wet chemical etch. No differences were observed in the AlGaAs spectra of the etched

and as grown samples.

3.3 Cathodoluminescence of AlGaAs in the groove

Epitaxial growth on the grooves produces well-defined facets (see Figure 3.1). Cathodoluminescence scanning electron microscopy [6] reveals a correlation between the facet orientation and the composition of AlGaAs epilayers grown on the grooves. Figure 3.2 shows spectrally resolved cathodoluminescence images taken of the cross section of a groove at two different wavelengths. Luminescence at 6700Å emanates from the unpatterned areas of the sample (facet e; see Figure 3.1), the top edge of the groove (facet c), and the bottom of the groove (facet a). Luminescence at 7000Å occurs exclusively on the sides of the groove (facet b). Emission peaks in the corresponding luminescence spectra occur at 6670Å (bottom of the groove and unpatterned region), and at 7160Å (side of the groove). This corresponds to a 130 meV reduction in the bandgap of material grown on the side of the groove relative to material on the bottom of the groove. A series of spectra were taken from points on the bottom of the groove to study the transition in the composition from the bottom of the groove to the side of the groove (see Figure 3.3). Two peaks appear in the spectra. The peak near 6700Å has its maximum intensity at the center of the groove. This peak decreases in intensity as the excitation is moved toward the side of the groove, while a peak at 7050Å appears. The intensity of the 7050Å peak continues to increase as the excitation is moved onto the side of the groove, while the peak at 6700Å disappears entirely (not shown). The two peaks remain distinct in cathodo-

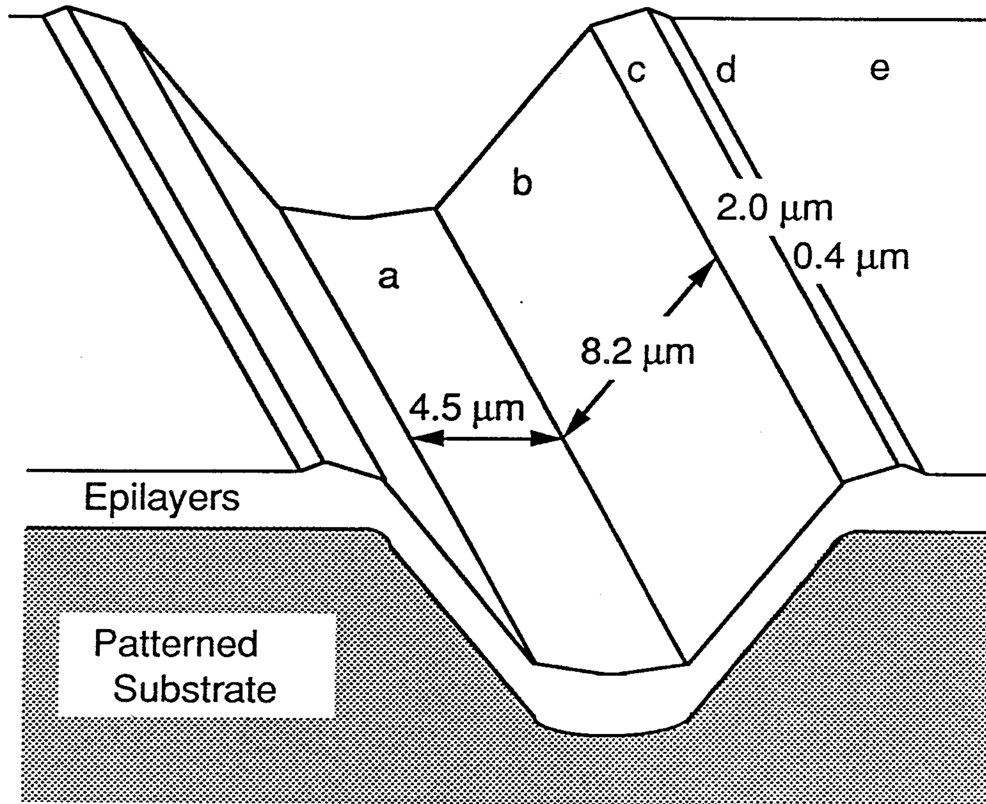

Figure 3.1: Diagram of the AlGaAs epilayers grown by molecular beam epitaxy on a non-planar substrate. Growth in the groove takes place on well-defined facets, which are labelled on the diagram, together with their dimensions.

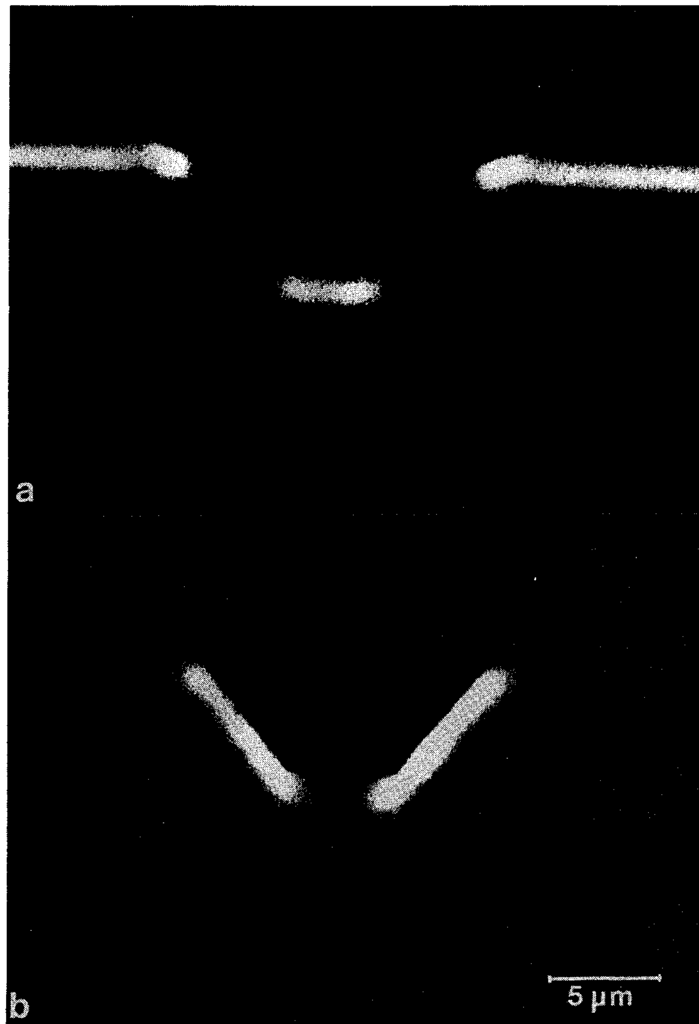

Figure 3.2: Spectrally resolved cathodoluminescence micrographs of a cross section of a groove in the surface. The micrographs represent spatially resolved luminescence at 6700Å (a), and 7000Å (b). Note that at 7000Å, only the sides of the groove luminesce, whereas at 6700Å, the other facets luminesce and the sides of the groove are dark.

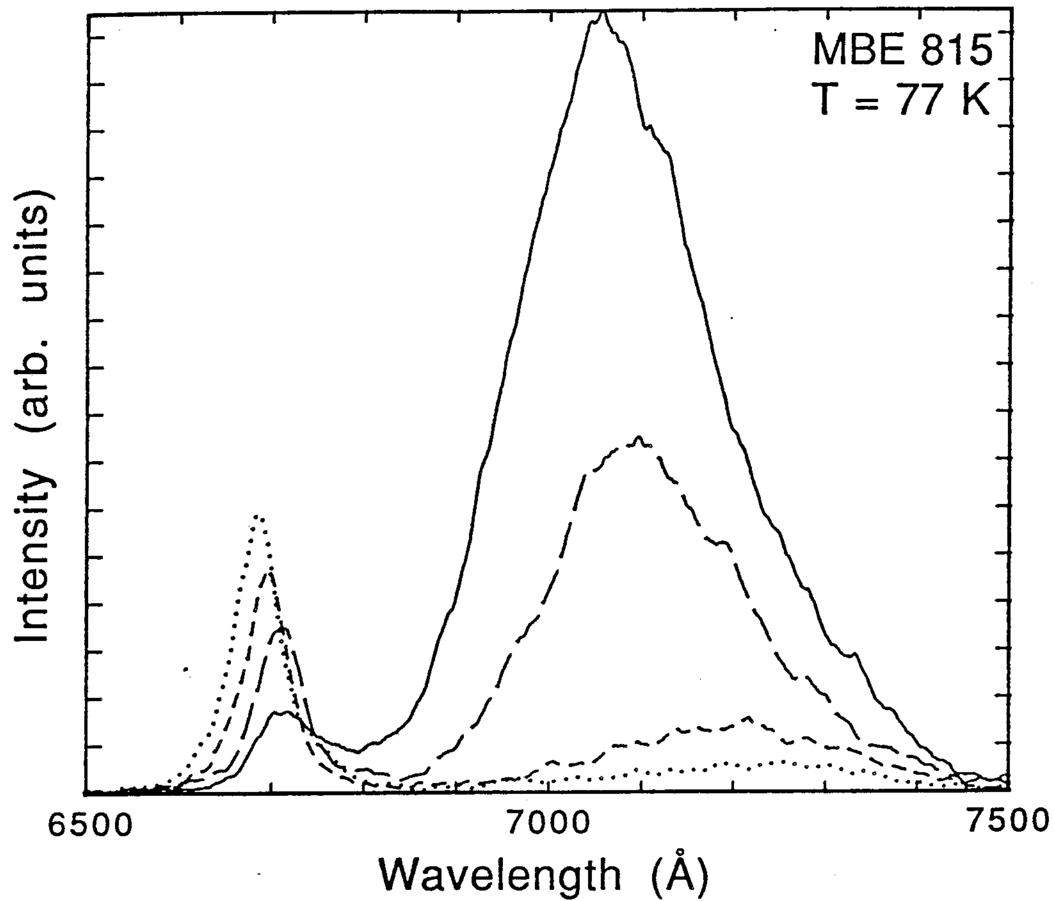

Figure 3.3: Cathodoluminescence spectra measured using spot excitation at various points around the border between the bottom of the groove (facet *a*) and the side of the groove (facet *b*) (see Figure 3.1). The two peaks remain distinct through the transition from facet *a* to facet *b*, consistent with an abrupt change in composition at the facet boundary. Dotted line: spot excitation of the center of facet *a*. Short dashes: excitation spot moved roughly 0.7 μm from the center of facet *a*. Long dashes: spot moved roughly 1.4 μm from the center of facet *a*. Solid line: excitation of the border between facets *a* and *b*.

luminescence spectra at all of the points sampled. This is consistent with an abrupt lateral change in the composition, from higher bandgap material on the bottom of the groove, to lower bandgap material on the side of the groove. The spatial resolution of cathodoluminescence, which is on the order of a micron in GaAs, is insufficient to measure the length scale on which the compositional transition takes place. In order to determine this, transmission electron microscopy was performed on a cross section of a groove.

3.4 Transmission electron microscopy of a groove

The sample was prepared for cross sectional transmission electron microscopy using the standard techniques of mechanical thinning and argon ion milling. The sample was cooled with liquid nitrogen during the final thinning. Dark field imaging of the sample was done with a Philips EM430 transmission electron microscope, using the (200) diffracted beam to reveal variations in the AlGaAs composition [7]. We observe a quasi-periodic modulation in the composition of AlGaAs grown on the side of the groove (see Figure 3.4). The modulation occurs in the side facets of the groove, which are misoriented (111)Ga facets. While not perfectly uniform, the layers are oriented approximately along the [111] direction. The period is typically in the range of 50-70Å. On the bottom [$\approx$ (811) orientation] and top [$\approx$ (411) orientation] facets, the AlGaAs composition is observed to be uniform. At the interface between these facets and the side facet, the composition undergoes an abrupt lateral transition from uniform to compositionally modulated AlGaAs (Figure 3.5).

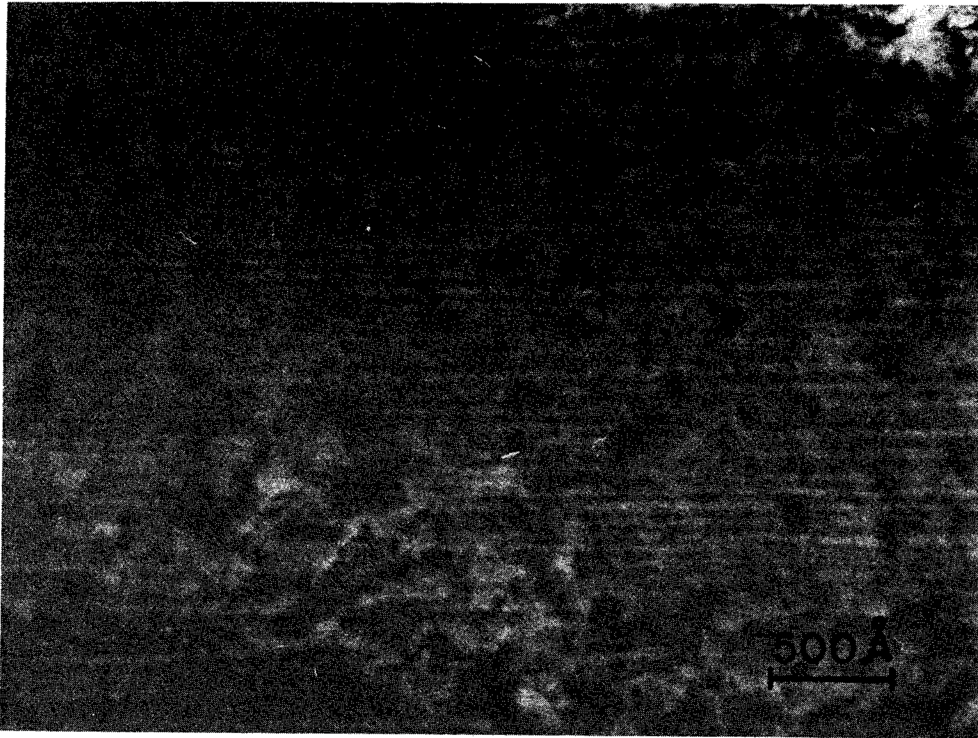

Figure 3.4: Dark field transmission electron micrograph of a cross section of the side of the groove, using the (200) reflection. The quasi-periodic contrast corresponds to compositional modulation of the AlGaAs grown on the side facet of the groove. The segregation of Al and Ga occurs spontaneously during the growth, forming layers of alternating Al concentration approximately along the [111] direction. The period in this area is about 70Å.

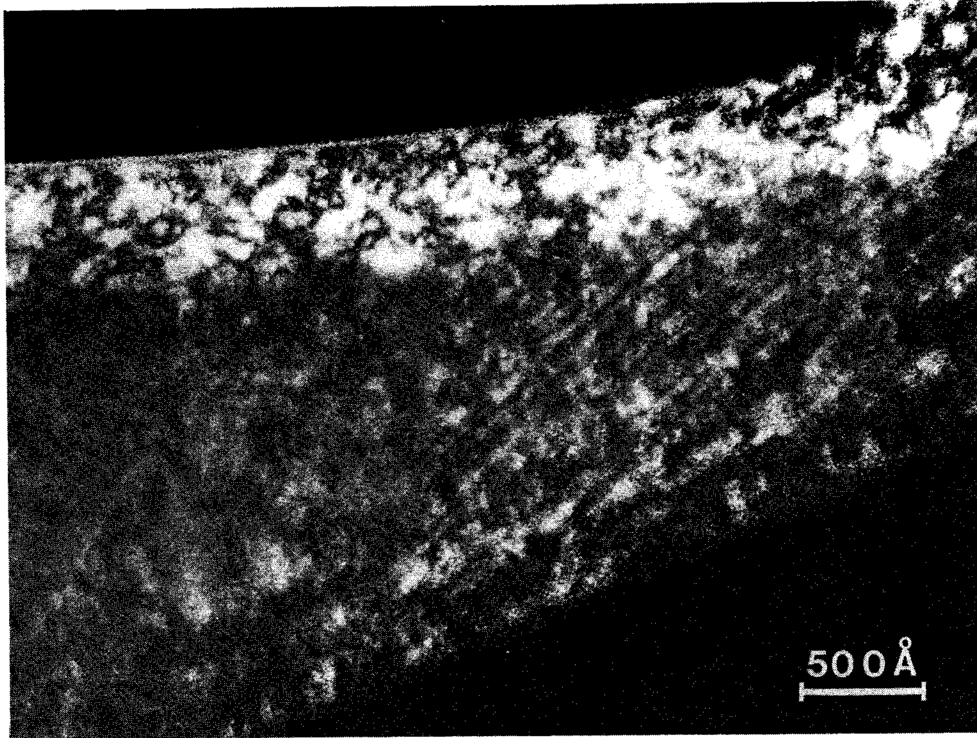

Figure 3.5: Dark field transmission electron micrograph of a cross section of the groove, showing the interface between material grown on the side of the groove and on the bottom of the groove. The left half of the micrograph shows material grown on the bottom of the groove. The right half, in which compositional modulation is seen along the [111] direction, shows material grown on the side of the groove. The compositional modulation is observed to terminate abruptly at the border between facets.

The period of the modulation is not correlated with the period of rotation of the substrate. Approximately 3-5Å of AlGaAs was deposited in the time required for one rotation of the sample holder. This is approximately the thickness of a single monolayer of growth.

Transmission electron microscopy was done on another growth to verify the existence of compositional modulation on the sides of the groove. The growth was done under the same conditions as were described above, and the results confirm the observations presented in this letter. Compositional modulation was observed to occur only on the side facets of the groove, along the [111] direction. The modulation was associated with a reduction in the bandgap observed by cathodoluminescence.

The compositional modulation observed in growth of AlGaAs on grooves in a GaAs substrate occurs selectively on particular facets in the growth. Furthermore, the abrupt termination of the modulation indicates that the mechanism responsible for the segregation is strongly dependent on the orientation of the surface. This constitutes a unique structure in III-V crystals. For this reason, we have named the growth technique *orientation selective epitaxy* (OSE), and refer to the compositional modulation as an *OSE superlattice.*

3.5 Zinc diffusion induced disordering of the OSE superlattice

In order to verify that the OSE superlattice observed by TEM is responsible for the facet dependence of the cathodoluminescence emission, zinc was diffused into the

sample. Zinc diffusion is known to disorder GaAs/AlGaAs superlattices by facilitating the intermixing of Ga and Al atoms within the column III sublattice. This technique has been shown to disorder the column III sublattice in other ordered alloys [8,9,10]. The sample was sealed in an evacuated quartz ampoule with $ZnAs_2$ as the diffusion source, and placed in a 650°C furnace for one hour. The diffusion parameters were chosen to completely disorder the compositional modulation. After the diffusion, cathodoluminescence spectra taken at 77 K showed that the emission peak occurred at 6920Å throughout the sample. The luminescence peak of the Zn-diffused AlGaAs is expected to be shifted toward longer wavelengths, due to band tailing and bandgap shrinkage [13]. Relative to the spectra taken from the sample before the diffusion, the luminescence peak from the unpatterned region shifted toward lower energies by 60 meV, and the peak from the sidewall shifted to higher energies by 67 meV. A similar diffusion, done at 600°C for one hour, resulted in only partial disordering of the superlattice.

The CL spectra of the sample after the 650°C diffusion indicate that the composition of the AlGaAs epitaxial layers was uniform. Thus, the OSE superlattice is responsible for the differences in the spectra from the various facets. Furthermore, the average aluminum concentration of the AlGaAs grown on the (111) facet is about the same as the aluminum concentration of uniform $Al_{0.25}Ga_{0.75}As$ grown on the (100) areas of the sample.

3.6 Discussion: Orientation selective epitaxy

Previous work has shown that compositional modulation due to alloy ordering is associated with a reduction in the effective bandgap of the material [8,9,10,11]. Thus, the TEM data are consistent with the cathodoluminescence data, which show that the peak in the luminescence spectrum of the side of the groove is shifted to lower energy by 130 meV relative to the corresponding peak in the spectrum of the bottom of the groove. A first order calculation, based on an envelope function calculation of the electronic states in a superlattice [12], indicates that the amplitude of the modulation is quite large ($\Delta x > 0.3$), with a minimum Al concentration near zero ($x_{min} < 0.1$). In Figure 3.6, the expected shift in the luminescence peak of a periodic superlattice, relative to the position of the spatially averaged potential, is plotted as a function of the minimum aluminum fraction. The increased linewidth of the AlGaAs peak from the side of the groove, relative to the peak from the bottom of the groove, is attributed to fluctuations in the amplitude and period of the OSE superlattice.

In III-V materials other than AlGaAs, ordering has been observed in the form of monolayer superlattices in the [111] direction, sometimes accompanied by compositional modulation along the [100] growth direction [8,11,14,15,16,17]. Bellon et al. showed that the compositional modulation occurs exactly along the [100] direction, even though the growth direction was tilted by 6° [17]. Monolayer superlattices in the [110] growth direction have been observed in InGaAs [18].

Segregation in $Al_xGa_{1-x}As$ is surprising because of the unique properties of this alloy. The sizes and electronegativities of Al and Ga are nearly identical, and the

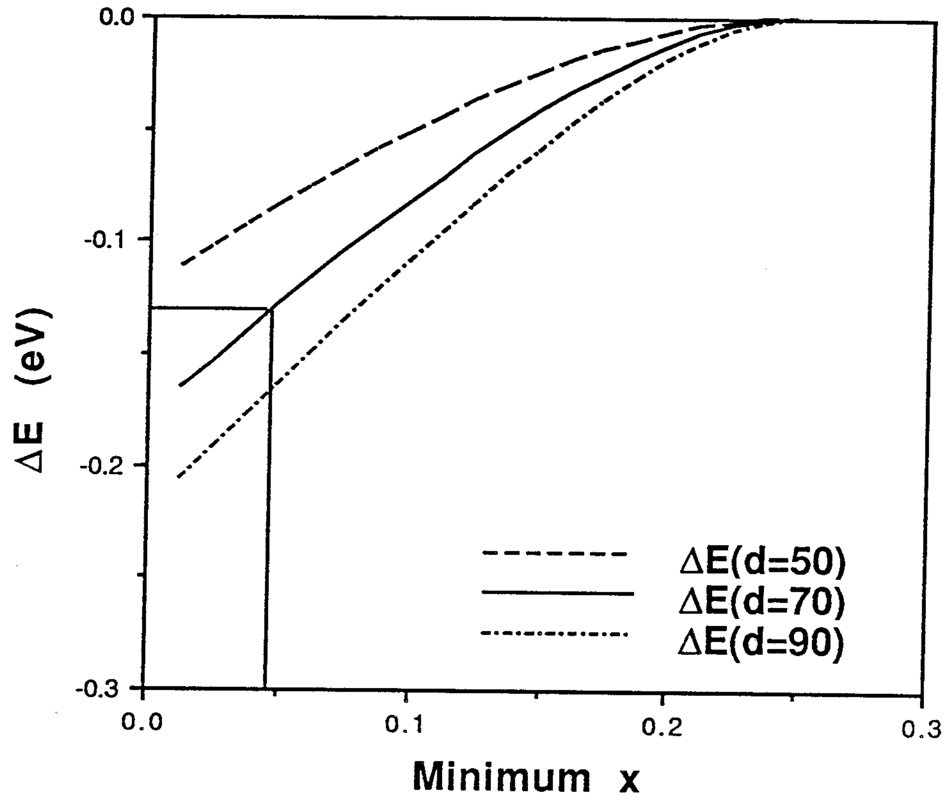

Figure 3.6: Calculation of the effect of compositional modulation on the effective bandgap energy in a superlattice, using the envelope function approximation.

bulk phase diagrams indicate that AlAs and GaAs should be fully miscible under normal growth conditions [19]. Nevertheless, long-range ordering of the $Al_xGa_{1-x}As$ alloy has been observed [20,21,22]. Compositional modulation of AlGaAs grown by conventional MBE has only been seen in the [110] and [100] directions [20,21]. In both cases, the modulation is observed to occur along the growth direction. Our observation of compositional modulation occurring spontaneously in growth on a (111) surface is new for the $Al_xGa_{1-x}As$ alloy.

The OSE superlattice bears some similarity to a tilted superlattice grown on vicinal (100) GaAs substrates [23]. There are several significant differences between these results and ours. First, the direction of growth is different. Second, in our work the molecular beams were on continuously, whereas the growth of tilted superlattices requires the use of alternating beam deposition to induce the segregation. Finally, the junctions formed between compositionally modulated material and uniform material are lateral to the growth plane in our work, whereas they occur in the growth plane in tilted superlattices. Still, there may be a connection between the mechanisms responsible for alloy segregation in the two experiments. This is investigated in Chapter 4.

3.7 Conclusions

The spontaneous, selective growth of a superlattice by orientation selective epitaxy represents a new capability in crystal growth, with potential application to *in situ* growth of higher dimensional nanometer scale structures. Our observation of an

abrupt lateral junction in a semiconductor alloy grown by MBE is new and potentially useful, because of the associated change in the bandgap. The termination of the OSE superlattice at the facet boundary effectively forms a lateral heterojunction, providing one way to use the orientation dependent properties of crystal growth to yield three dimensional control of the electronic states in a crystal. The theory and applications of OSE growth are discussed in Chapter 4, and the work is extended to growth on different surface orientations in Chapter 5.

Bibliography

[1] E. Kapon, D. M. Hwang, and R. Bhat, "Stimulated Emission in Semiconductor Quantum Wire Heterostructures," Phys. Rev. Lett., **63**, 430 (1989).

[2] Michael E. Hoenk, Howard Z. Chen, Amnon Yariv, Hadis Morkoç, and Kerry J. Vahala, "Cathodoluminescence measurement of an orientation dependent aluminum concentration in $Al_xGa_{1-x}As$ epilayers grown by molecular beam epitaxy on a nonplanar substrate," Appl. Phys. Lett., **54**, 1347 (1989).

[3] Michael E. Hoenk, Howard Z. Chen, Amnon Yariv, Hadis Morkoç, and Kerry J. Vahala, "Orientation dependence of the aluminum concentration in $Al_xGa_{1-x}As$ epilayers grown by molecular beam epitaxy on a nonplanar substrate," paper WA5, *Topical Conference on Quantum Wells for Optics and Optoelectronics*, Salt Lake City, Utah, March 6-8, 1989.

[4] E. Kapon, J. P. Harbison, C. P. Yun, and L. T. Florez, "Patterned quantum well semiconductor laser arrays," Appl. Phys. Lett., **54**, 304 (1989).

[5] H. P. Meier, E. Van Gieson, W. Walter, C. Harder, M. Krahl, and D. Bimberg, "Molecular beam epitaxy of GaAs/AlGaAs quantum wells on channeled

substrates," Appl. Phys. Lett. **54** 433 (1989).

[6] Michael E. Hoenk and Kerry J. Vahala, "Cathodoluminescence system for a scanning electron microscope using an optical fiber for light collection," Rev. Sci. Instrum., **60**, 226 (1989).

[7] P. M. Petroff, "Transmission electron microscopy of interfaces in III-V compound semiconductors," J. Vac. Sci. Technol., **14**, 973 (1977).

[8] F. P. Dabkowski, P. Gavrilovic, K. Meehan, W. Stutius, J. E. Williams, M. A. Shahid, and S. Mahajan, "Disordering of the ordered structure in metalorganic chemical vapor deposition grown $Ga_{0.5}In_{0.5}P$ on (001)GaAs substrates by zinc diffusion," Appl. Phys. Lett., **52**, 2142 (1988).

[9] A. Gomyo, T. Suzuki, K. Kobayashi, S. Kawata, I. Hino, and T. Yuasa, "Evidence for the existence of an ordered state in $Ga_{0.5}In_{0.5}P$ grown by metalorganic vapor phase epitaxy and its relation to band-gap energy," Appl. Phys. Lett., **50**, 673 (1987).

[10] W. E. Plano, D. W. Nam, J. S. Major, Jr., K. C. Hsieh, and N. Holonyak, Jr., "Column III and V ordering in InGaAsP and GaAsP grown on GaAs by metalorganic chemical vapor deposition," Appl. Phys. Lett., **53**, 2537 (1988).

[11] Akiko Gomyo, Tohru Suzuki, and Sumio Iijima, "Observation of Strong Ordering in $Ga_xIn_{1-x}P$ Alloy Semiconductors," Phys. Rev. Lett., **60**, 2645 (1988).

[12] G. Bastard, "Superlattice band structure in the envelope-function approximation," Phys. Rev. B, **24**, 5693 (1981).

[13] H. C. Casey, Jr., and Frank Stern, "Concentration-dependent absorption and spontaneous emission of heavily doped GaAs," J. Appl. Phys., **47**, 631 (1976).

[14] M. A. Shahid, S. Mahajan, D. E. Laughlin, and H. M. Cox, "Atomic Ordering in $Ga_{0.47}In_{0.53}As$ and $Ga_xIn_{1-x}As_yP_{1-y}$ Alloy Semiconductors," Phys. Rev. Lett., **58**, 2567 (1987).

[15] Osamu Ueda, Masahiko Takikawa, Junji Komeno, and Itsuo Umebu, "Atomic Structure of Ordered InGaP Crystals Grown on (001)GaAs Substrates by Metalorganic Chemical Vapor Deposition," Jpn. J. Appl. Phys., **26**, L1824 (1987).

[16] Y. E. Ihm, N. Otsuka, Y. Hirotsu, J. Klem, and H. Morkoç, "Summary Abstract: Ordering in $GaAs_{0.5}Sb_{0.5}$ grown by molecular-beam epitaxy," J. Vac. Sci. Technol. B, **6**, 743 (1988).

[17] P. Bellon, J. P. Chevalier, G. P. Martin, E. Dupont-Nivet, C. Thiebaut, and J. P. Andre, "Chemical ordering in $Ga_xIn_{1-x}P$ semiconductor alloy grown by metalorganic vapor phase epitaxy," Appl. Phys. Lett., **52**, 567 (1988).

[18] T. S. Kuan, W. I. Wang, and E. L. Wilkie, "Long-Range Order in $In_xGa_{1-x}As$," Appl. Phys. Lett., **51**, 51 (1987).

[19] A. Ourmazd and J. C. Bean, "Observation of Order-Disorder Transitions in Strained-Semiconductor Systems," Phys. Rev. Lett., **55**, 765 (1985).

[20] P. M. Petroff, A. Y. Cho, F. K. Reinhart, A. C. Gossard, and W. Wiegmann, "Alloy Clustering in $Ga_{1-x}Al_xAs$ Compound Semiconductors Grown by Molecular Beam Epitaxy," Phys. Rev. Lett., **48**, 170 (1982).

[21] T. S. Kuan, T. F. Kuech, W. I. Wang, and E. L. Wilkie, "Long-Range Order in $Al_xGa_{1-x}As$," Phys. Rev. Lett., **54**, 201 (1985).

[22] W. I. Wang, T. S. Kuan, J. C. Tsang, L. L. Chang, and L. Esaki, "Segregated AlGaAs(110) grown by molecular beam epitaxy," J. Vac. Sci. Technol. B, **4**, 517 (1986).

[23] J. M. Gaines, P. M. Petroff, H. Kroemer, R. J. Simes, R. S. Geels, and J. H. English, "Molecular-beam epitaxy growth of tilted GaAs/AlAs superlattices by deposition of fractional monolayers on vicinal (001) substrates," J. Vacuum Sci. Technol. **B6** 1378 (1988).

Chapter 4

Orientation selective epitaxy: Theory

4.1 Introduction

In the last chapter, growth on patterned substrates was shown to be capable of the selective growth of a superlattice on particular facet orientations. This capability, named orientation selective epitaxy, suggests the possibility of using substrate orientation as a tool for growing three dimensional structures *in situ.*

The optical and electronic properties of a nanometer scale structure depend on the nature of surrounding surfaces and interfaces. Using molecular beam epitaxy, it is possible to fabricate a heterojunction which is abrupt to within a few atomic layers. While this capability has made possible the growth of quantum wells with extremely high luminescence efficiency, the interfaces are not, in fact, perfect. Recent understanding of the mechanisms involved in MBE growth has resulted in improve-

ment of the quality of heterointerfaces through modification of the growth technique. The question therefore arises as to whether optimization of the growth parameters can improve the quality of superlattices, and other structures, grown by orientation selective epitaxy.

Monte Carlo simulations have been used to study molecular beam epitaxial growth, and to point toward techniques for improving the quality of crystals grown by molecular beam epitaxy. Interruption of the growth was predicted, and later shown, to reduce the roughness of heterointerfaces in the MBE growth of AlGaAs/GaAs quantum wells. Similar simulations, applied to orientation selective epitaxy, might provide information about the nature of the observed structures and interfaces, and suggest ways to modify the growth for improved characteristics.

In this chapter, the mechanism of orientation selective epitaxy will be discussed. The nature of MBE growth will be introduced, and issues relevant to orientation selective epitaxy will be discussed. Migration enhanced epitaxy and the growth of tilted superlattices will be presented, because the issues involved are directly applicable to orientation selective epitaxy. It will be shown that there is a connection between orientation selective epitaxy and the growth of tilted superlattices by migration enhanced epitaxy. This connection is based on the effect of the surface orientation in a patterned substrate on the fluxes of atoms and molecules arriving at the surface. Calculations of time dependent fluxes on patterned substrates and simulations of crystal growth will be presented in support of this model. Finally, applications of these techniques to the *in situ* growth of nanometer scale structures and devices will

be discussed.

4.2 Molecular beam epitaxy

Molecular beam epitaxial growth of crystals is accomplished through the deposition of atoms and molecules on a heated substrate in an UHV environment (Figure 4.1). The growth rate is sufficiently low that, by shuttering the fluxes, it is possible to control the composition with precision along the growth direction approaching one monolayer. Critical to the quality of heterointerfaces is the surface roughness during growth. If atoms and molecules were incorporated randomly into the crystal, the surface would become rough, and it would be impossible to grow abrupt heterojunctions. Because interface roughness affects the electrical and optical properties of heterostructures grown by MBE, the surface morphology during growth is important for device structures [1]. Therefore, MBE must promote planar growth if it is to produce optimized structures. This is highly dependent on the surface kinetics of adatoms during growth, which are related to the growth conditions.

4.2.1 Nucleation and growth

In MBE, atoms and molecules migrate on the surface before being incorporated into the crystal. Incorporation into the crystal occurs at kinks and steps in the surface, where the binding energy is higher and adatoms are stabilized against migration. Whether the surface becomes planar or rough depends on the nucleation and growth mechanism.

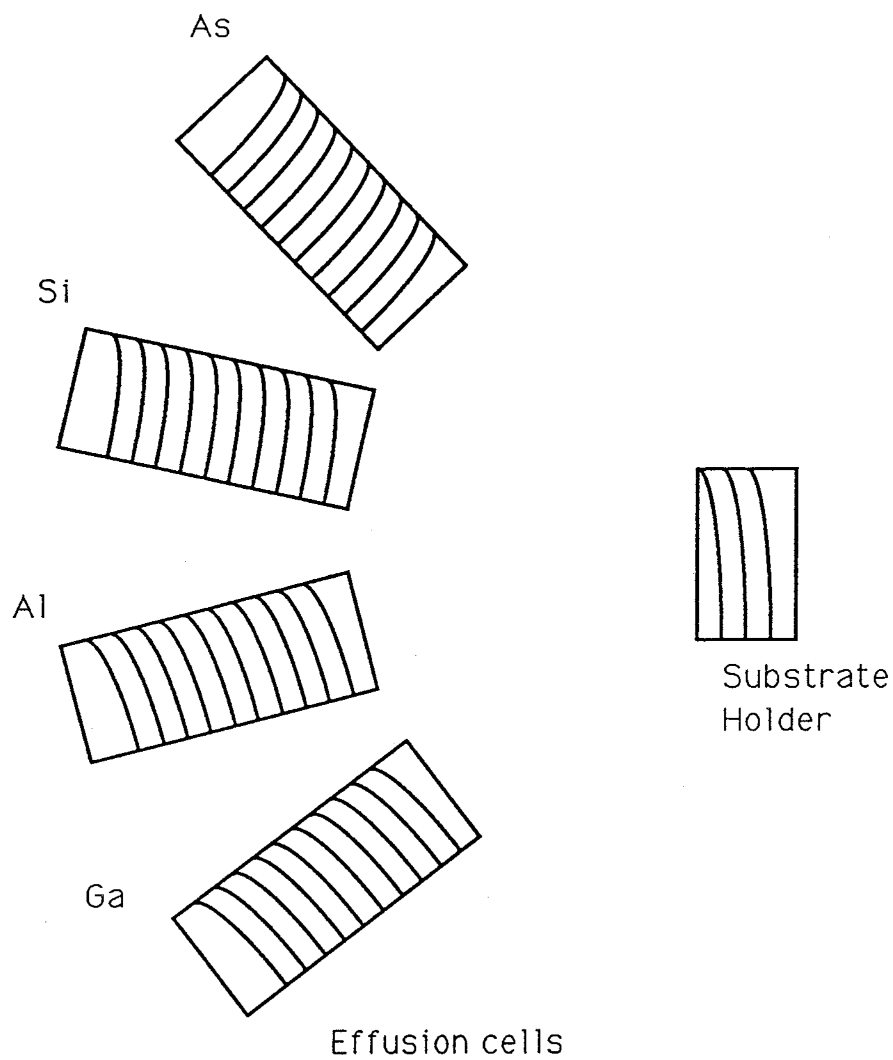

Figure 4.1: MBE growth chamber.

Much of what is known about GaAs nucleation and growth by MBE is determined by reflection high energy electron diffraction (RHEED). This method of monitoring the surface during growth is unique to MBE, because the growth is done in ultra-high vacuum conditions. During the growth, the RHEED electron beam impinges on the surface at a glancing incidence. Electrons, diffracted by the crystal surface, are imaged on a screen. The intensity of the RHEED signal is related to the surface roughness, so oscillations in the RHEED intensity are interpreted as oscillations in the step density on the surface [2,3].

For growth on a flat surface, atoms and molecules arriving at the surface will form islands, and growth will proceed via addition of atoms to the edges of the islands. The density of steps on the surface will then increase as islands start to form, and decrease as separate islands merge to form a complete layer. If the growth is done on a substrate which is misoriented from a low index crystalline plane, the surface will have terraces and steps, with a characteristic terrace width determined by the degree of misorientation. If the adatoms are sufficiently mobile, they will migrate to the steps at terrace edges, where they can be incorporated into the crystal. In this case, growth will occur by step flow, resulting in smooth, layer by layer growth [2] (see Figure 4.2). Otherwise, growth will occur by island nucleation, producing rough surfaces and interfaces. Whether island or step nucleation dominates is highly dependent on the conditions which affect the surface diffusion of adatoms.

Under some growth conditions, the RHEED oscillations have been observed to disappear. This phenomenon has been interpreted as a transition from 2-D nucleation

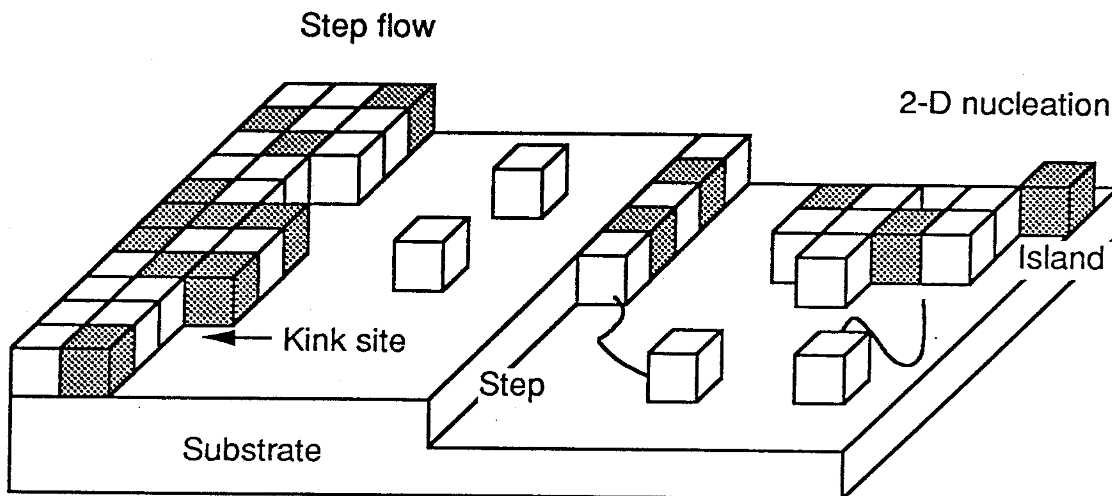

Figure 4.2: Growth by step flow and island nucleation.

to step flow, and has been used to estimate the surface diffusion length. Surface diffusion is found to be very sensitive to the growth conditions, depending on the Ga flux, the As flux, the substrate temperature, and the surface reconstruction [2,3].

4.2.2 Kinetics of GaAs/AlGaAs growth

The growth of a crystal by MBE involves the deposition of atoms and molecules from the vapor phase. Subsequent rearrangement of atoms on the surface can occur by surface migration, desorption, reactive incorporation of molecules, and exchange reactions. However, these processes occur far from thermodynamic equilibrium, so that the composition of the crystal is determined by configuration dependent *kinetic* rates, rather than by thermodynamic stability [4]. Once the crystal is formed, the bulk diffusion parameters are far too slow to allow relaxation into the lowest energy state. For this reason, it is possible to grow epitaxial layers which have a significant amount of excess strain energy and a low defect density. Furthermore, uniform alloys can be grown, in spite of the presence of a miscibility gap in the mixture.

In the application of MBE to GaAs/AlGaAs growth, the group III atoms, Ga and Al, are supplied as atomic species, and the group V element, As, is supplied as either diatomic or tetratomic molecules. At substrate temperatures below 650°C, Ga and Al have sticking coefficients of essentially unity, meaning that desorption of these atoms is negligible. Upon arrival at the surface, Ga and Al atoms bind to atoms in the layer beneath. They subsequently migrate on the surface, until encountering a step, a kink site, or other unbound group III atoms, whereupon reaction with arsenic can stabilize them against further migration. Arsenic, on the other hand, is much more volatile,

and desorbs fairly readily, unless it finds a suitable site for incorporation. For this reason, growth is usually done with an excess of arsenic to ensure that stoichiometry is maintained. The fluxes of Ga and Al, in this case, determine the growth rate, and the incorporation of arsenic is determined by the time dependent atomic configuration of the surface.

Arsenic plays a significant role in determining the kinetics of growth. Growth of a crystal by step flow requires that the Ga and Al atoms be able to migrate to step edges, before reacting with arsenic. If this is not possible, islands will form on the surface, and the growth will occur by 2-D nucleation. Arsenic, which arrives as diatomic or tetratomic molecules, undergoes a dissociative reaction with Ga and Al on the surface, to form GaAs and AlAs molecules. Whereas Ga and Al atoms migrate readily on the surface, GaAs and AlAs migrate more slowly [5].

In the absence of As, migration of Ga and Al is significantly enhanced. Island formation is reduced, because the islands are less stable against breaking up. The surface roughness decreases significantly, because the group III atoms, in the absence of arsenic, will form a single monolayer on the As-stabilized substrate. Gallium or aluminum atoms are only weakly bound to a Ga-stabilized surface, and quickly migrate until they encounter a step edge, where they can bind to an arsenic atom. The kinetics of growth under these conditions have been used to advantage in migration enhanced epitaxy, which will be discussed in section 4.4.

Incorporation rates for arsenic, and hopping rates for gallium and aluminum, have a significant dependence on the configuration of atoms on the surface. Therefore, the

evolution of the surface is determined by the interaction of these kinetic processes. The rates for various processes depend on user-defined parameters, such as atomic and molecular fluxes, substrate temperature, and substrate orientation. Unfortunately, these configuration dependent rates are essentially unknown. Measurements of such parameters as surface diffusion length have been made, but these represent an average over all atomic processes, and may depend on parameters such as impurity concentration and the condition of the substrate. In order to simulate the kinetic nature of MBE growth, rates for these processes must be estimated from bulk crystal parameters and whatever measurements are available [4].

4.2.3 Monte Carlo simulation of MBE growth

Lack of knowledge of the configuration dependent rates limits the quantitative accuracy of Monte Carlo simulations of growth, particularly with regard to specific material systems and growth conditions. Nevertheless, the surface kinetic nature of atomistic growth, which is essential to the MBE growth process, is inaccessible to other forms of simulation. The usefulness of these simulations lies in developing a conceptual framework for understanding MBE growth, in which the relative importance of various processes can be understood, related to the growth conditions, and applied to improve the quality of crystals grown under modified conditions. This has been demonstrated by the advent of growth interruption as a technique for obtaining smoother heterojunctions and improved optical properties of heterostructures [6].

Growth of a crystal by molecular beam epitaxy takes place far from thermodynamic equilibrium. The crystal composition and surface roughness during growth are

determined by kinetically controlled atomic processes, with rates which depend on user-defined growth conditions. For the purposes of Monte Carlo simulation, these atomic processes, which include the migration of adatoms on the surface, reactive dissociation of molecular species, desorption of atoms and molecules from the surface, and Ga-Al exchange reactions, can be modeled as Arrhenius processes with configuration dependent activation energies [4]. A representative process, with an activation energy, E_a, and a rate constant, R_0, will occur with a rate, R, defined by

$$R = R_0 exp \frac{-E_a}{kT} \tag{4.1}$$

where k is Boltzman's constant, and T is the substrate temperature during the growth. The configuration dependence of the rates can then be incorporated into the values of R_0 and E_a.

A simulation begins with the random arrival of an atom on the substrate surface. The times for the various processes are calculated, based on configuration dependent rates, and events are allowed to occur in temporal order. Whenever the arrival or departure of an atom from a site in the crystal affects the rate of processes for a nearby atom, the times for the processes are recalculated. In this way, all of the configuration dependent processes can be tracked through the history of the growth. Before proceeding to the application of such a simulation to orientation selective epitaxy, the kinetic nature of ordering and segregation in the AlGaAs alloy will be discussed.

4.3 Alloy growth in III-V epitaxy: Ordering and segregation

Semiconductor III-V alloys, such as $Al_xGa_{1-x}As$, exhibit a composition dependent bandgap. This has been used for bandgap engineering in heterostructure device design and fabrication, by applying crystal growth techniques to control the alloy composition. In AlGaAs, the aluminum and gallium are incorporated into (nominally) random sites in the group III sublattice. This random distribution affects electrical transport in the alloy, by causing scattering of electrons and holes. Local variations in the composition, which would result from alloy clustering, have an effect on the electrical and optical properties of the crystal. Nonrandom distribution of atoms in the alloy is, therefore, important to the performance of devices fabricated from these crystals.

Recently, there has been a lot of research on ordering effects in semiconductor alloys. Ordering, in the sense of preferential incorporation of the different atomic species at specific sites in the crystal lattice, has been observed in several material systems. This often takes the form of a monolayer superlattice, in which two components of the alloy are incorporated in alternate monoatomic layers of the growth [7]. This type of superlattice is detectable by electron diffraction from the crystal, causing the appearance of forbidden reflections in TEM diffraction patterns. Compositional modulation has also been observed, in which the alloy segregates into layers several unit cells thick, which alternate in composition. This has been observed by imaging the layers with transmission electron microscopy [8].

In several of these alloys, spinodal decomposition of the alloy into separate phases occurs, as a result of a miscibility gap in the alloy under the growth conditions employed. In some cases, spinodal decomposition has been observed under conditions which would not give rise to a miscibility gap for the bulk material. The observation of spinodal decomposition in these cases was attributed to strain in the growing layer imposed by a lattice mismatch between the epitaxial layer and the substrate. Petroff et al. observed compositional modulation in AlGaAs grown by MBE on (110)GaAs [8]. The compositional modulation was oriented approximately along the (110) direction of growth, exhibiting small deviations from that orientation. This was the first such observation of compositional modulation in AlGaAs, and it was attributed to spinodal decomposition of the alloy. The authors proposed that a miscibility gap exists in AlGaAs grown on (110)GaAs, due to an orientation dependent phase diagram in MBE [8]. Compositional modulation in AlGaAs growth on (110)GaAs was later verified by Kuan et al., in a seminal paper published in 1985 [7]. The primary purpose of this paper was to show the existence of long-range order in AlGaAs grown by MBE and OMVPE on both (100) and (110) substrates. This was the first observation of long-range ordering in any III-V semiconductor ternary alloy. The order, which took the form of a monolayer superlattice, was asserted to be the equilibrium phase of AlGaAs below 800°C. Kinetic effects, as an explanation for the ordering, were ruled out by the authors on the basis of observed ordering in the [010] and [001] directions for [100] growth [7].

The existence of spinodal decomposition in AlGaAs would be very surprising. Al-

GaAs is unique in that the sizes and electronegativities of aluminum and gallium are nearly identical, so that there is very little strain involved in the formation of the alloy. In this case, the free energy which could drive the alloy into a segregated equilibrium state would not be expected to overcome the entropy of mixing. In fact, AlAs and GaAs are expected to be completely miscible under normal growth conditions. Calculations of the effect of strain on the phase separation of alloys were done by Zur and McGill, who concluded that the strain in AlGaAs is too small to open a miscibility gap [9]. They further concluded that a negative enthalpy of mixing, induced by charge transfer from weaker Ga-As bonds to stronger Al-As bonds [10], is not sufficient to stabilize an ordered state of AlGaAs at the growth temperatures employed [9]. Cohen and Schlijper [11] explicitly recognize that the bulk interdiffusivity of aluminum and gallium is too small for thermodynamic phase separation to occur, and that the material will probably be out of global thermodynamic equilibrium. For this reason, they do not consider phase separation. With regard to the ordering observed by Kuan et al., they argue that surface diffusion can generate an ordered state, and that strong multiatom interactions can account for stability of long-range order without invoking strain. Having concluded that the ordered state is thermodynamically stable under the growth conditions used by Kuan et al., and that the arrangement of atoms can be modified by diffusion on the surface, they conclude that the ordering observed by Kuan et al. is thermodynamic in origin [11].

The arguments based on thermodynamic stability of ordered states do not adequately demonstrate the relevance of thermodynamic stability to MBE growth. Fur-

thermore, Gaines et al. [12] have grown AlGaAs under conditions which maximize surface diffusion of gallium and aluminum, and rather than ordering, they find that the gallium and aluminum exhibit *kinetic* segregation on terraces in the substrate (see section 4.4.2). Thermodynamically driven segregation and ordering in AlGaAs were contested by Madhukar, who contended that MBE growth occurs far from thermodynamic equilibrium, and that segregation of aluminum and gallium is caused by kinetic effects in MBE growth [4,13]. Madhukar suggested that the orientation dependent surface geometry, based on tetrahedral bonding in GaAs/AlGaAs, should play a significant role in interlayer diffusion during growth. Furthermore, exchange reactions should play a greater role in [110] growth than [100] growth [13]. Finally, Madhukar has stated that the nearly periodic Al concentration fluctuation, observed by Petroff et al. [8], may be explained by a strain dependent activation barrier for Al-Ga exchange reactions [4]. If segregation were caused by thermodynamics, then decreasing the growth rate would be expected to enhance the effect [4,14]. This experiment was performed by Wang et al., in a study of segregation in AlGaAs growth on GaAs(110) [15]. Reduction of the growth rate from 1 μm/h to 0.3 μm/h reduced the 10 nm scale compositional modulation, contrary to expectations based on thermodynamic segregation, but a monolayer superlattice existed under all growth conditions employed [15]. On the basis of this observation, Van Vechten introduced a model for kinetic segregation of aluminum and gallium into a monolayer superlattice. The model, which is based on Ga-Al exchange reactions driven by the energy release in bond formation, predicts that steps in the surface can give rise to the type

of segregation reported by Wang et al. [14,15].

The ordering observed by Kuan et al. [7] has been explained by Ogale et al. in terms of the surface reconstruction during growth [16]. In particular, Ogale et al. were able to reproduce long-range ordering, both in-plane and normal to the growth plane, using Monte Carlo simulations of $Al_{0.33}Ga_{0.67}As$ growth on a reconstructed (100) surface. The kinetically based in-plane ordering, demonstrated by this calculation, serves to refute the statement made by Kuan et al. that long-range order must be thermodynamic in origin [7], thus resolving the theoretical difficulty presented by observed long-range ordering in nonequilibrium MBE growth of AlGaAs. There is yet another mechanism for spontaneous segregation in AlGaAs, which is explicitly kinetic in origin. This involves the growth of tilted superlattices, via migration enhanced epitaxy, and will be discussed in section 4.4.

4.4 Migration enhanced epitaxy

Migration enhanced epitaxy (MEE), a modification of molecular beam epitaxy, produces crystals with interfaces smooth to within a monolayer. In MEE, the surface of a growing crystal exhibits a self-flattening effect, resulting from the kinetics of Ga migration in an arsenic-free environment [5]. By shuttering the atomic and molecular beams, Ga and As are supplied to the surface in cycles. The period of the cycle is typically chosen so that one complete monolayer is deposited per cycle.

The cyclic deposition scheme used in the growth of GaAs by migration enhanced epitaxy is shown in Figure 4.3. Ga is deposited in an As-free environment during

the first part of the cycle. When enough Ga has been deposited for one complete monolayer of coverage, the Ga flux is turned off. For a short period of time, none of the beams are active. Ga atoms may migrate freely during this half of the cycle. The kinetics of growth in the absence of arsenic are such that the Ga atoms form a single monolayer on the As-stabilized substrate. During the final part of the cycle, As is deposited to complete the growth of the monolayer. Because Ga is deposited in an As-free environment, the effective diffusion length of Ga atoms is significantly longer than would be the case in conventional molecular beam epitaxy at the same substrate temperature. Consequently, one of the applications of this technique is to grow high quality GaAs epitaxial layers at considerably lower temperatures than are normally required.

4.4.1 Tilted superlattices

Migration enhanced epitaxy can be applied to the growth of AlGaAs as well. By arranging the shutter sequence so that Al and Ga are deposited during different parts of the cycle, layer by layer growth is possible, in which the Al and Ga are deposited on different parts of terraces on a vicinal substrate. Such a deposition scheme was proposed by Petroff et al. [17], prior to the development of migration enhanced epitaxy, in order to grow superlattices oriented at an angle with respect to the substrate. The idea was to deposit partial layers of GaAs and AlGaAs, which would, in growth by step flow, be incorporated at steps in the surface. Such a deposition scheme would, ideally, result in the formation of a superlattice, $(\mathrm{GaAs})_m(\mathrm{AlGaAs})_n$, with a tilt angle that depends on the total amount of surface coverage per cycle, $m+n$. Initial

efforts to grow such structures failed, because of a stated inability to grow ordered superlattices with $m + n <= 1.7$ [17]. The failure was probably due to nonuniform growth at step edges, related to the relatively short diffusion lengths of Ga and Al at the growth temperatures employed. Fractional layer superlattices were successfully grown using MOVPE [18], a technique which has a higher surface diffusion rate than conventional molecular beam epitaxy.

Tilted superlattices (TSL) were successfully grown by MBE only after the alternating deposition technique of migration enhanced epitaxy was utilized to increase the surface diffusion length [12,19]. By introducing another stage into the MEE cycle, in which Al atoms are deposited and allowed to migrate, Gaines et al. succeeded in getting kinetic segregation of Al and Ga on the terraces (see Figure 4.4). During each of the group III deposition stages, the Ga and Al atoms are preferentially deposited at steps in the surface. The existence of the TSL, which was observed directly by transmission electron microscopy, shows that the layer by layer growth via step flow is of sufficient quality to form periodic structures lateral to the growth direction.

The role of the arsenic flux in TSL growth is not as important as that of the group III fluxes. In the experiments of Gaines et al., this was tested by attempting TSL growth without shuttering of the arsenic beam. No difference in the TSL growth was observed [12].

One very interesting result was the formation of a TSL on substrates misoriented toward the [011] direction on a (100) substrate, but not on substrates misoriented toward the $[01\overline{1}]$ direction [12]. This was attributed to differences in the structure

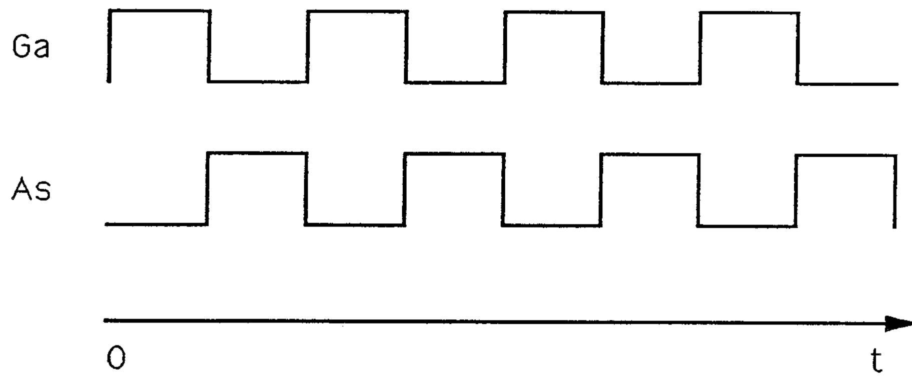

Figure 4.3: Shutter sequence used in migration enhanced epitaxial growth of GaAs.

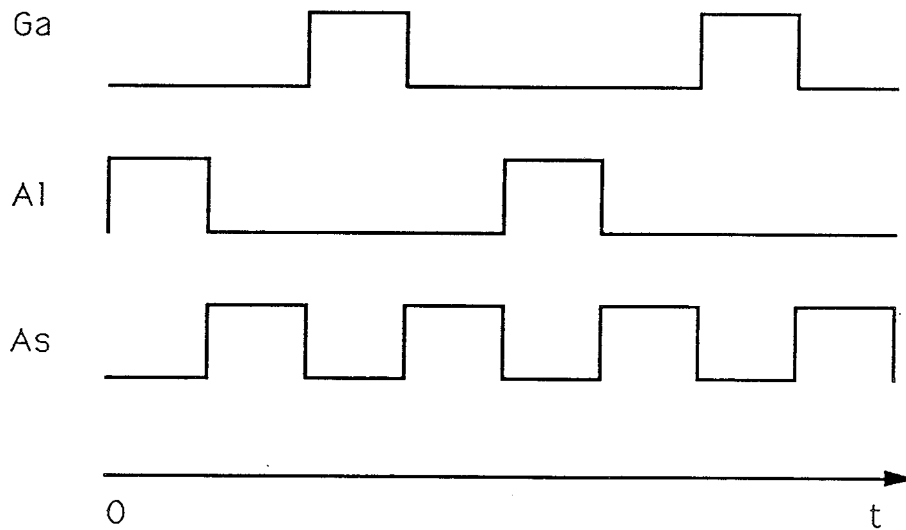

Figure 4.4: Deposition scheme for tilted superlattice growth. (After Gaines et al., 1988.)

of steps on a (100) substrate for the different misorientations, observed by Pukite et al. [20]. Steps on substrates misoriented toward the [011] direction have a large variation in step width and a low density of kinks, whereas substrates misoriented toward $[01\bar{1}]$ have regularly spaced steps and a high density of kinks. These differences would be evident in the TSL growth, because the period of a TSL originates from the period of steps in the surface. Based on Pukite's observations, misorientation toward [011] would result in TSL's which have relatively straight boundaries, but which are not very periodic. Misorientation toward $[01\bar{1}]$ would result in a periodic TSL, which does not have straight boundaries. The second case may not be conducive to observation by transmission electron microscopy, because transmission of electrons through a TSL with crooked boundaries would result in a reduction of contrast. The first case corresponds to the observations of Gaines et al. It is possible that growth of a GaAs layer by MEE results in regular terrace widths, accounting for the periodic nature of the TSL growth reported by Gaines et al. [12].

4.4.2 Coherent tilted superlattices

TSL growth has also been achieved with coherent deposition of Ga and Al during MEE growth [21] (see Figure 4.5). The resulting coherent tilted superlattice (C-TSL) resembles the TSL reported by Gaines et al. [12]. C-TSL growth was only observed for misorientation toward the [011] direction. By comparison of the phases of segregation in the growth of TSL on C-TSL, and vice versa, it was determined that Al is deposited preferentially at the step riser, and Ga is deposited at the step edge. This was attributed to the difference in the kinetics of Ga and Al migration during

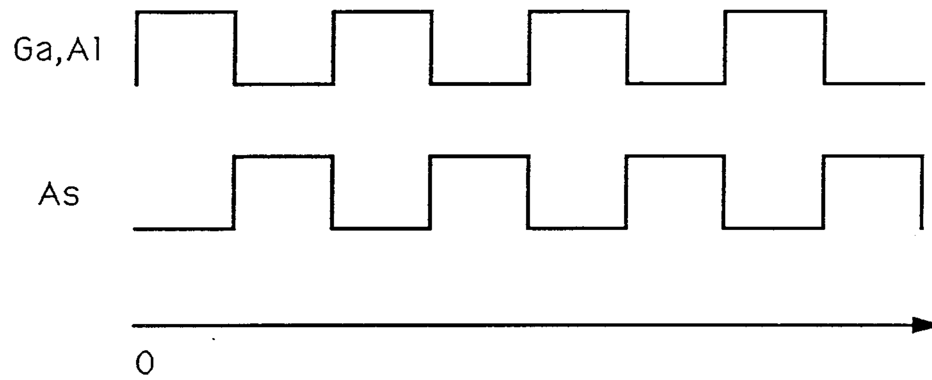

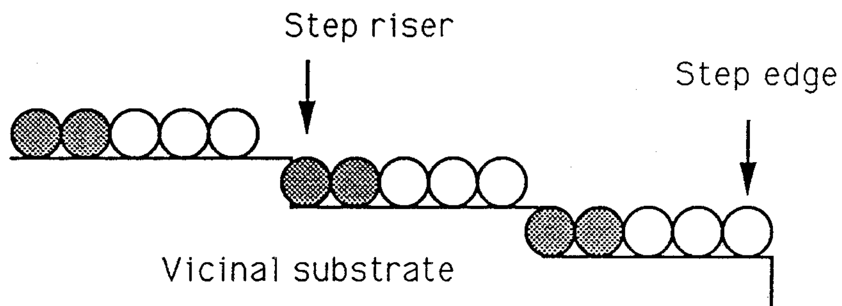

Figure 4.5: Deposition scheme for growth of a coherent tilted superlattice (after Tsuchiya et al., 1989).

crystal growth, in the following manner. As the growth of the layer proceeds, Ga atoms which encounter the step risers are weakly bound, relative to aluminum atoms. Therefore, aluminum atoms displace the gallium atoms at the steps, so that after one monolayer is deposited, aluminum is concentrated at the step riser, and gallium at the step edge. The modulation amplitude of the C-TSL, as expected, is not as strong as for the TSL.

4.5 Orientation selective epitaxy

Orientation selective epitaxy, as we have shown in previous chapters, produces a superlattice selectively on particular crystal facets in AlGaAs grown on a patterned substrate. Growth on unpatterned areas of the same crystal do not exhibit the superlattice structure. We propose that orientation selective epitaxy can be attributed to the kinetics of MBE growth on stepped surfaces, using time dependent fluxes induced by rotation of the substrate. In support of this hypothesis, we will present the results of calculations of the time dependent fluxes in the growths discussed in this thesis, and of Monte Carlo simulations based on these calculations.

4.5.1 Surface chemistry

The chemistry on the growing surface, which determines the growth kinetics, is a function of the surface orientation. The geometry of bonds, the surface interatomic distance, and the surface reconstruction are facet dependent, so that kinetic rates vary from facet to facet. An example of this orientation dependence is given by

grooves oriented in the $[01\bar{1}]$ and [001] directions. The sides of the grooves in these cases are {111}Ga and {101} planes, respectively. The former is a polar surface, consisting of alternate layers of group III and group V atoms, whereas the latter is a nonpolar surface, consisting of layers containing equal numbers of group III and group V atoms. Clearly, the chemistry of these two radically different surfaces will affect the nature of growth. These effects were cited by Madhukar as potential causes of the Al-Ga segregation observed in AlGaAs grown on (110)GaAs [13] (see section 4.3). In particular, growth on {101} planes is susceptible to the formation of facets, creating local changes in the surface orientation.

As we have seen in the case of the tilted superlattice, the chemistry can be manifested in subtle ways as well. TSL growth was observed in growth on (100) substrates misoriented toward the [011] direction, but not on substrates misoriented toward the $[01\bar{1}]$ direction, due to a difference in the structure of steps on the misoriented surfaces. In the same way, growth on the sides of grooves can be expected to depend on subtle misorientation of the side facets, as well as on gross changes in the activation barriers for migration on different crystal planes. The degree of misorientation, the direction of the steps, and the step roughness will depend on the preparation of the substrate, and on the growth conditions during deposition of the buffer layer.

4.5.2 Geometry of MBE growth on nonplanar surfaces

The effect of the geometry of the MBE chamber on growth on patterned substrates has long been recognized [22]. The atomic and molecular beams, impinging on the substrate at an angle dictated by the relative orientation of the effusion cells and

the substrate, will have different effective fluxes on variously oriented crystal facets. It was believed, however, that rotation of the substrate compensates for this effect, because the time averaged flux arriving at the surface is proportional to the cosine of the angle between the surface normal and the rotation axis, assuming that the Ga and Al beams are incident at a sufficiently shallow angle that the fluxes do not go to zero during any part of the rotation. In this case, the relative fluxes averaged over time would be independent of surface angle. We have seen, however, that time dependent fluxes can have an important effect on the kinetics of crystal growth.

4.5.3 Time dependent fluxes

In the MBE growth chamber, the effusion cells are located on the periphery of the chamber. The atomic and molecular beams impinge on the substrate surface at an angle with respect to the rotation axis (see Figure 4.6).

The time dependence takes the form of

$$F(t) = F_0[cos\Phi_{Ga,Al}cos\theta - sin\Phi_{Ga,Al}sin\theta cos(\omega t - \gamma_{Ga,Al})] \quad (4.2)$$

where $F_0 cos\theta$ is the time averaged flux, θ is the angle between the surface normal and the rotation axis, ω is the angular frequency of substrate rotation, $\gamma_{Ga,Al}$ is the projection of the effusion cell position on the plane of the substrate, and $\Phi_{Ga,Al}$ is the azimuthal angle of the effusion cell. Because this equation gives a negative flux if $\theta + \Phi > \pi/2$, it is understood that the flux is zero in this case. When $\theta + \Phi = \pi/2$, equation 4.2 takes the simpler form

$$F(t) = 2F_0 cos\Phi_{Ga,Al}cos\theta sin^2(\frac{\omega t}{2} - \frac{\gamma_{Ga,Al}}{2}). \quad (4.3)$$

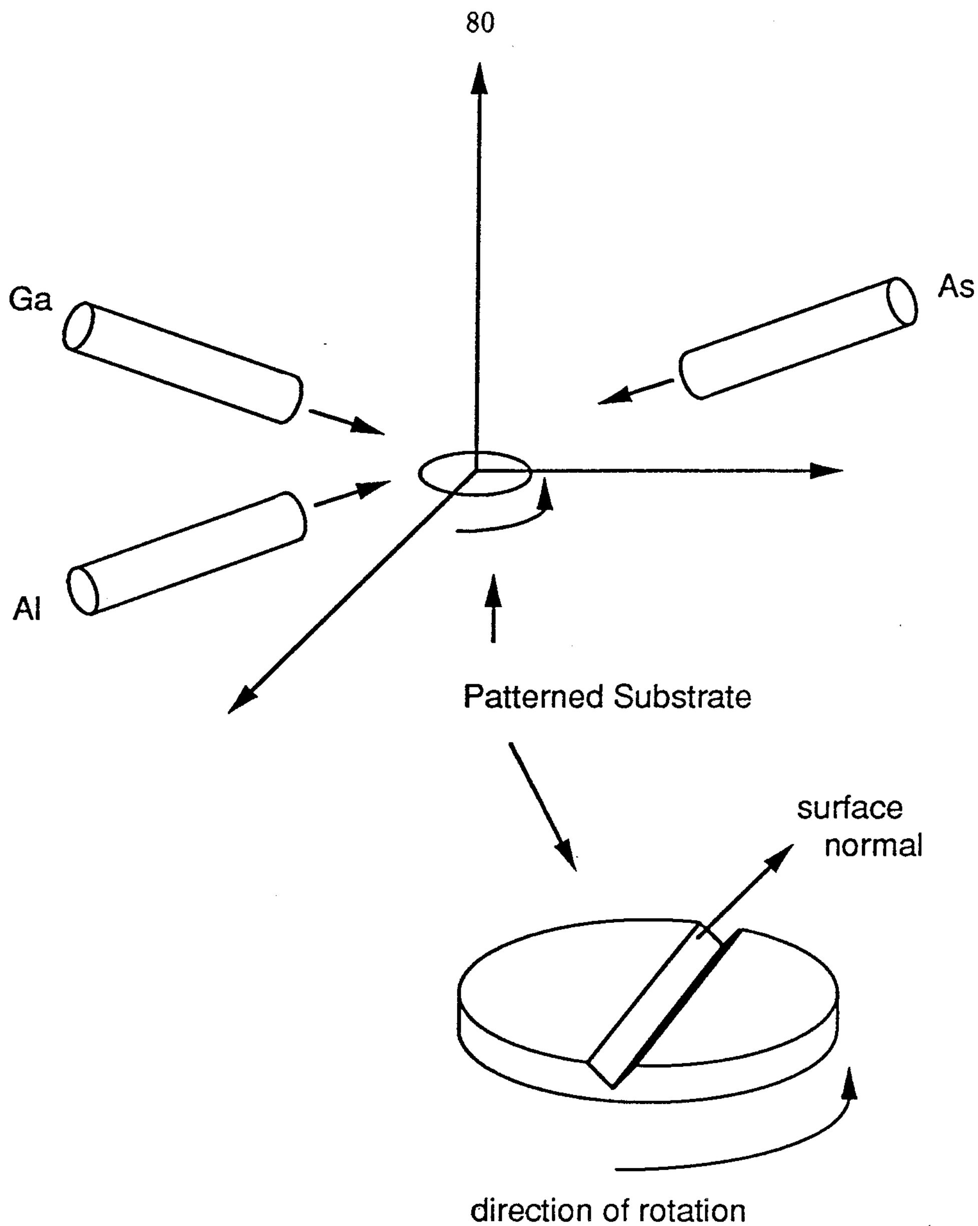

Figure 4.6: Relative geometry of the effusion cells and the rotating substrate, showing also the effect on a nonplanar surface.

There are two important points to be made here. First of all, if the $\theta + \Phi < \pi/2$, then the time averaged flux is given by

$$\overline{F} = F_0 cos\Phi_{Ga,Al} cos\theta. \tag{4.4}$$

Therefore, each of the atomic and molecular beams has the same $cos\theta$ dependence of the time averaged flux. If interfacet diffusion were neglected[1], the growth rate on the different facets would be proportional to $cos\theta$. This implies that the average composition should be independent of facet orientation. The second point is that the time dependent fluxes may give rise to compositional modulation, in spite of the average composition being independent of facet angle. In the following sections, we will consider the various ways in which this can occur.

4.5.4 Substrate rotation induced compositional modulation

Substrate rotation has been cited as the cause of periodic variation of alloy composition along the growth direction [24,25]. This effect results from time dependent fluxes due to inhomogeneities in the beams arriving at the substrate. The spatial period of the compositional modulation was shown to be equal to the temporal period of the substrate rotation during growth, multiplied by the growth rate. For several reasons, this effect could not be responsible for the compositional variations observed in our experiments. The primary evidence for this is that the observed period of compositional modulation in our experiments is much larger than the product of the rotation period and the growth rate. With a growth rate of 0.88μm/h, and a rotation

[1]It is reasonable to neglect interfacet diffusion for the growth temperature used in our experiments (600°C), but at higher growth temperatures the interfacet diffusion becomes very important [23].

rate of 26 rpm, approximately 5.6Å of AlGaAs was deposited on the (100) facets per revolution, corresponding to two monolayers of growth. Because the growth rate is smaller on angled facets, compositional modulation with the observed period of 70Å could not originate from this mechanism. Furthermore, compositional modulation in our samples is observed to intersect with the substrate/epilayer interface, which rules out mechanisms that predict compositional modulation along the growth direction.

4.5.5 Beat frequency compositional modulation

If the period of rotation were different than the time required for the growth of a single monolayer, then the composition of the monolayers may exhibit modulation due to the beat frequency between the rotation frequency and the monolayer growth rate. This could result in periodic compositional modulation, with a spatial period similar to that observed in our experiments.

The beat frequency modulation can be parameterized in terms of a frequency mismatch parameter, M, which is defined as the ratio of number of atoms in a monolayer to the number of atoms deposited in one rotation period. This is approximately equivalent to the time to grow a monolayer, t_{ml}, divided by the rotation period of the substrate, t_{rot}:

$$M = \frac{\#\ of\ atoms\ in\ a\ layer}{\#\ of\ atoms\ in\ one\ rotation} \approx \frac{t_{ml}}{t_{rot}}. \tag{4.5}$$

With this definition of M, and a specified geometry of the MBE growth chamber, the fluxes can be integrated to get the expected composition of successive layers in the growth. In Figure 4.7, the compositional modulation for two different geometries,

with $M = 1.05$, has been plotted. The amplitude of the modulation is not very large, however. For a mismatch of $M = 1.05$, we calculate that the aluminum fraction will vary in the range of approximately $x = 0.25(+0.02, -0.01)$, with a spatial period of approximately 56Å. An effect of this magnitude would have a negligible effect on the spectral emission, and it would be at the very limits of detection by transmission electron microscopy. Compared to the in-plane compositional modulation discussed in section 4.5.6, beat frequency compositional modulation is a small effect, and would only be expected to dominate in the two dimensional nucleation and growth regime. In this case, a multilayer growth front would reduce the amplitude still further, and clustering effects [26] would probably have a more significant impact on the bandgap than beat frequency compositional modulation. If the mismatch parameter were larger, the spatial period of the modulation would be shorter, with a corresponding increase in the amplitude. This would, possibly, improve the ease of detection by transmission electron microscopy, but it would not alter the spectral emission significantly, because the effects of amplitude and period on the bandgap offset one another.

To the extent that the growth rate does not fluctuate, beat frequency compositional modulation would be expected to be perfectly periodic and aligned to the growth direction, which does not correspond to our observations. Changing the geometry, by increasing the angular separation between the group III effusion cells, increases the amplitude by a small amount, and increases the thickness of the gallium-rich layers. This would improve the robustness of the compositional modulation

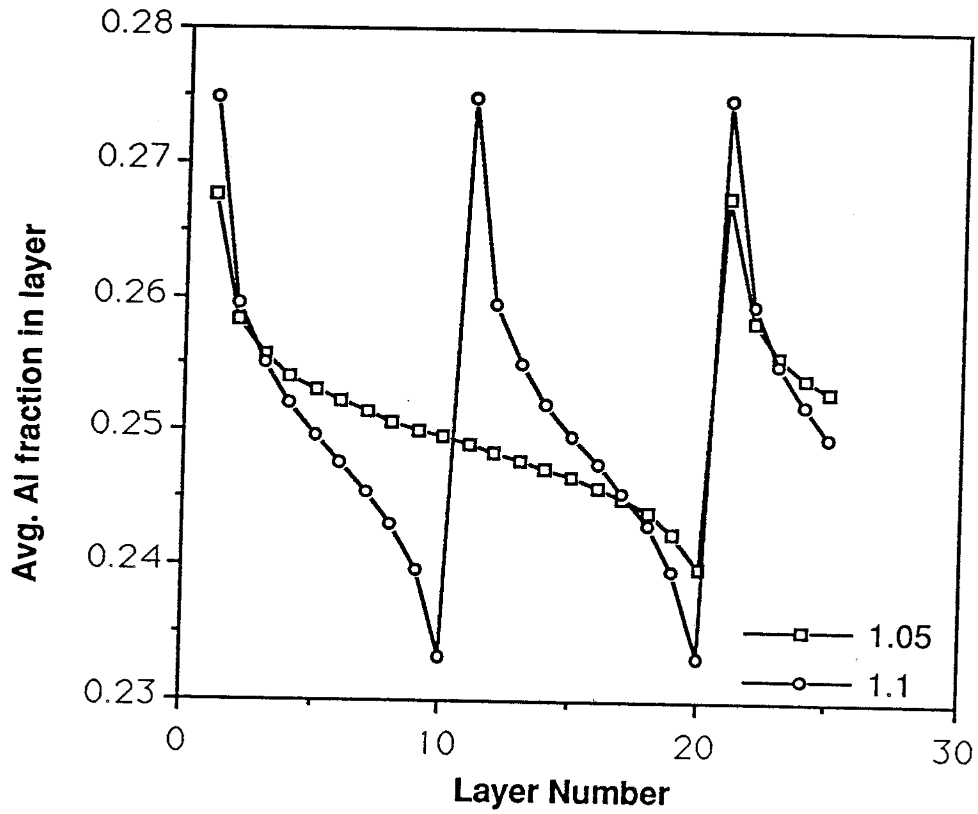

Figure 4.7: Beat frequency compositional modulation for $M = 1.05$, plotted for Ga and Al separated by $\frac{\pi}{4}$ and π radians.

against being smeared out by a rough growth front. The modulation can be tuned, to a certain extent, by changing the rotation rate of the substrate. However, the amplitude of the compositional modulation is related to the period in a way which is fixed by the geometry and the mismatch parameter, so that the amplitude and period cannot be changed independently. Furthermore, as we have mentioned, changes in amplitude and period tend to offset one another with respect to the bandgap of the resulting superlattice structure.

For the reasons outlined in the preceding discussion, beat frequency compositional modulation is not likely to be responsible for the compositional modulation observed in our experiments. A more likely candidate is a mechanism which is related to the growth of tilted superlattices by migration enhanced epitaxy, which is the subject of the next section.

4.5.6 Orientation selective epitaxy and the OSE superlattice: Selective migration enhanced epitaxy

In the last section, we considered the effect of time dependent fluxes on the composition of layers grown in the nucleation and growth regime of MBE. We found that there could be compositional modulation induced by a beat frequency between the rotation rate and the monolayer growth rate. This type of modulation would appear in the nucleation and growth regime, because atoms in a given layer would be deposited randomly. However, the form of the beat frequency compositional modulation does not match our observations, so we have to look elsewhere for the origin of the OSE superlattice.

When growth proceeds by step flow, we have seen that time dependent fluxes can have a significant effect on the in-plane composition (see section 4.4). In fact, if the growth proceeds strictly by step flow, the entire growth can be viewed as the propagation of individual steps across the surface, and periodic variation of the composition can take place in the plane of growth. In this section, we will calculate the impact of substrate rotation on the in-plane composition, in the step flow growth regime. Finally, in section 4.6, we will compare the results of a Monte Carlo simulation to this calculation.

For the experiments presented in this thesis, the aluminum and gallium cells were separated by approximately 45° in the (100) projection, and the arsenic cell was located opposite these two cells. Furthermore, the nominal aluminum fraction was approximately 0.25. The azimuthal angle of the effusion cells, Φ, is approximately 33° Given these parameters, we can use equation 4.2 to calculate the total group III flux, the group V flux, and the V-III flux ratio as a function of time, for the (111) facet (Figure 4.8). From this, we find that the V-III flux ratio is quite low during the time in which most of the group III deposition occurs. This is to be compared with the deposition scheme for migration enhanced epitaxy, in which the group V flux is shut off during the group III deposition (see section 4.4).

Based on the kinetics of growth during migration enhanced epitaxy, we expect that the migration of adatoms will be enhanced in orientation selective epitaxy, for highly inclined facets[2]. Even if the gallium and aluminum were deposited in phase,

[2]According to the experimental measurements of diffusion length [2,3], the diffusion of adatoms is enhanced for low V-III ratio at a given group III flux, and for low group III flux at a given V-III ratio. From

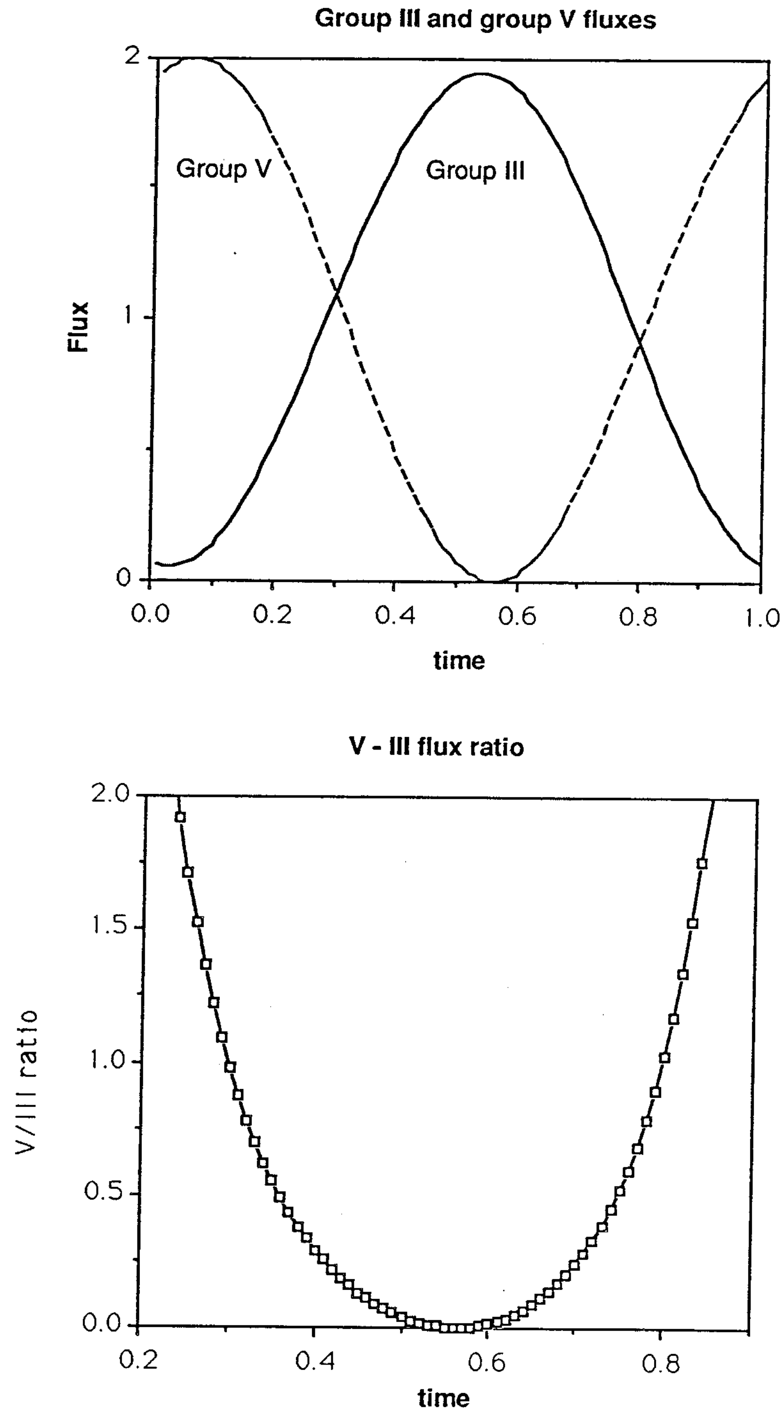

Figure 4.8: Group III and group V fluxes, and the V-III ratio, plotted vs. time for growth on the (111) facet of a rotating, patterned (100) substrate.

we might expect segregation to occur on steps in the growing surface, producing a structure analogous to a C-TSL (see section 4.4.2) selectively on the (111) facets. The angular separation between the group III cells produces a phase difference between the deposition of gallium and aluminum, so that the amplitude of compositional modulation in orientation selective epitaxy will be significantly larger than that of a C-TSL.

Continuing with the calculation, we can plot the gallium and aluminum fluxes, and the instantaneous aluminum fraction for deposition of a single monolayer, as functions of time (see Figure 4.9). The aluminum fraction in the incoming beams varies between 0 and 1 during the growth of a monolayer. If the growth occurs by step flow, this will result in a significant in-plane variation of the aluminum fraction. By integrating the flux in equation 4.2, we can convert the instantaneous aluminum fraction in Figure 4.9 to a function of the fraction of the layer grown. The resulting function can be integrated to calculate the average aluminum concentration for each column of atoms in a step, for a given terrace width. This is shown in Figure 4.10. We find that, for ideal growth by step flow, the composition of the layer will have a large in-plane variation, with an amplitude which is nearly independent of terrace width.

The expected in-plane variation of the aluminum concentration depends on the relative orientation of the group III effusion cells, the facet orientation, and the orientation of the group V cell. For facets which are not as highly inclined with respect

a combination of these considerations, the migration rate will be enhanced through most of the growth on highly angled facets (see Figure 4.8).

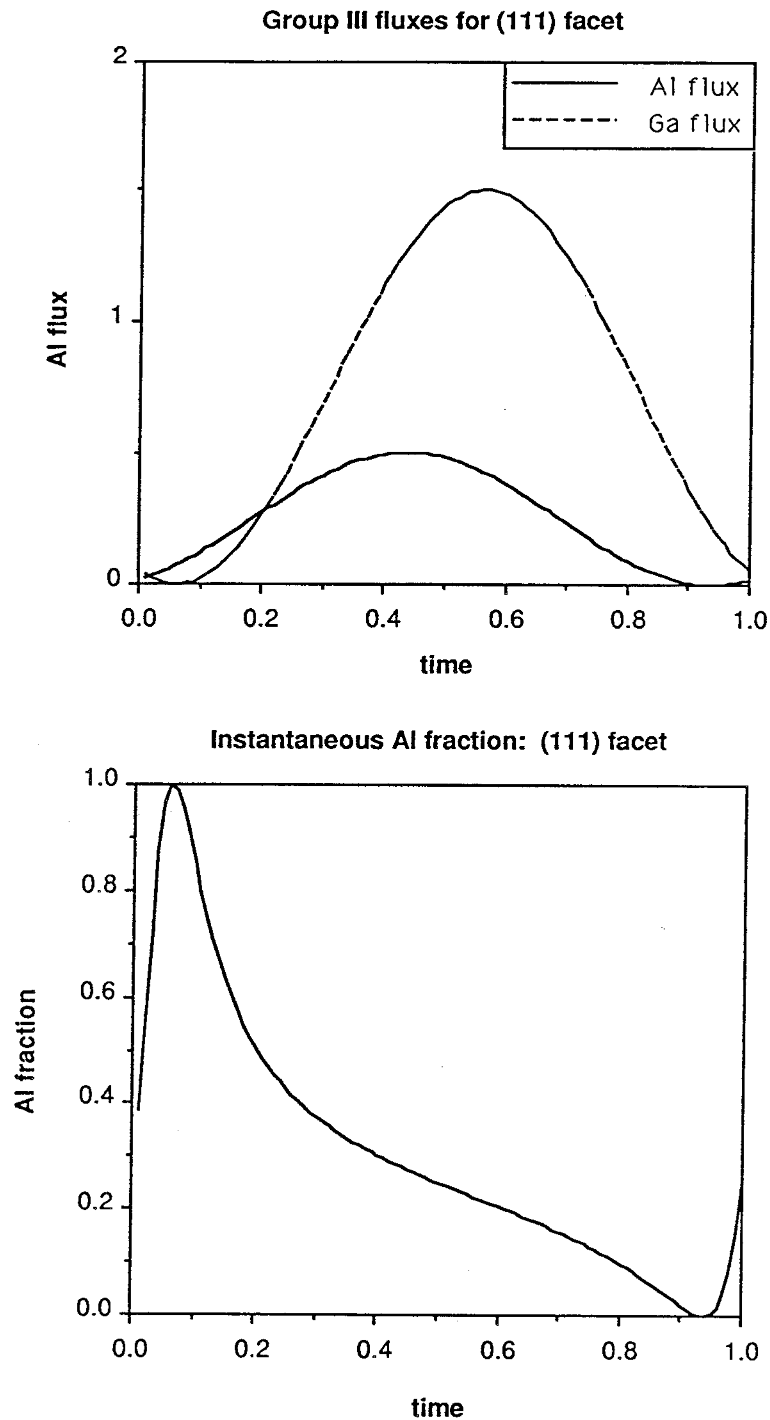

Figure 4.9: Group III fluxes for growth on the (111) facets of a rotating (100) substrate. The top graph shows the gallium and aluminum fluxes, plotted vs. time, for growth on the (111) facets of grooves in a rotating (100) substrate. The bottom graph shows the instantaneous aluminum fraction impinging on the surface, as a function of time.

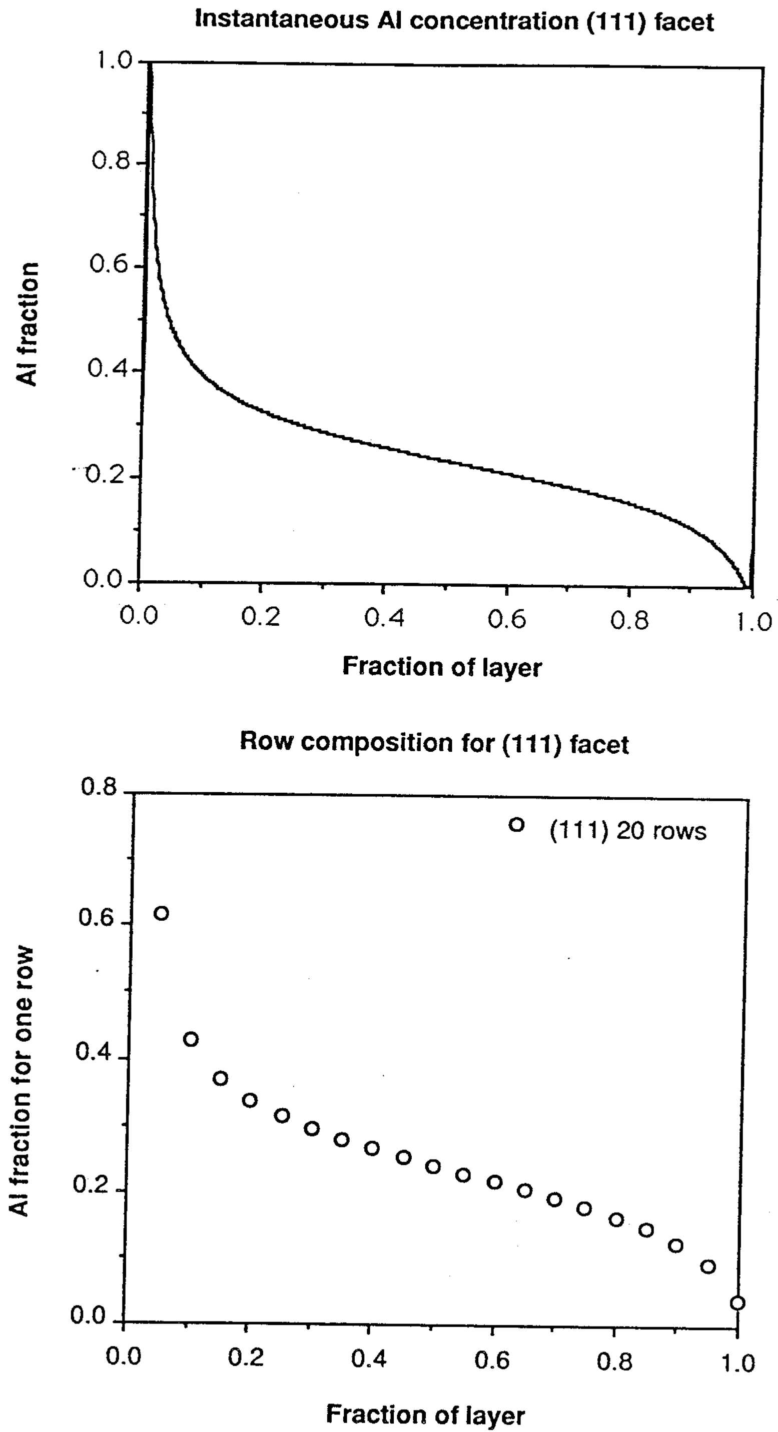

Figure 4.10: In-plane variation of the composition in orientation selective epitaxy. The top graph shows the instantaneous aluminum fraction as a function of the fraction of layer grown. The bottom graph shows the average composition of successive columns, for a terrace width of 20 atoms.

to the (100) surface, the amplitude of the OSE superlattice would be correspondingly smaller. Calculation of the expected amplitude for the (211) facet, for the same geometry as was used for the (111) facet, gives a composition which varies from 0.18 to 0.33, within a 20 column terrace width. The amplitude may be further reduced, because the smaller modulation of the arsenic flux will reduce the mobility of adatoms on the (211) facet. However, near a local perturbation in the surface orientation, there may be an enhancement of the OSE superlattice in the shadow of the perturbation. This is a possible explanation for the observed enhancement of the compositional modulation in the (211) facet of sample NSI2, near small (111) facets (see Chapter 5).

In-plane variation of the aluminum concentration results in an OSE superlattice when successive layers are grown (see Figure 4.11). The angle between the OSE superlattice planes and the substrate is determined by the magnitude of the mismatch parameter, M, discussed in section 4.5.5. The quality of the OSE superlattice is determined by the kinetic rates during growth, which are in turn related to the growth conditions and the facet orientation. In section 4.6, a Monte Carlo simulation of the growth of an OSE superlattice will be presented to explore some of these considerations.

The geometrical dependence of OSE superlattice growth suggests methods for optimization and manipulation. Increasing the angular separation of the group III cells would increase the expected amplitude of the OSE superlattice. The use of larger azimuthal angles for the effusion cells would extend the range of facet orientations which exhibit an OSE superlattice. If a group V cell with an azimuthal angle near

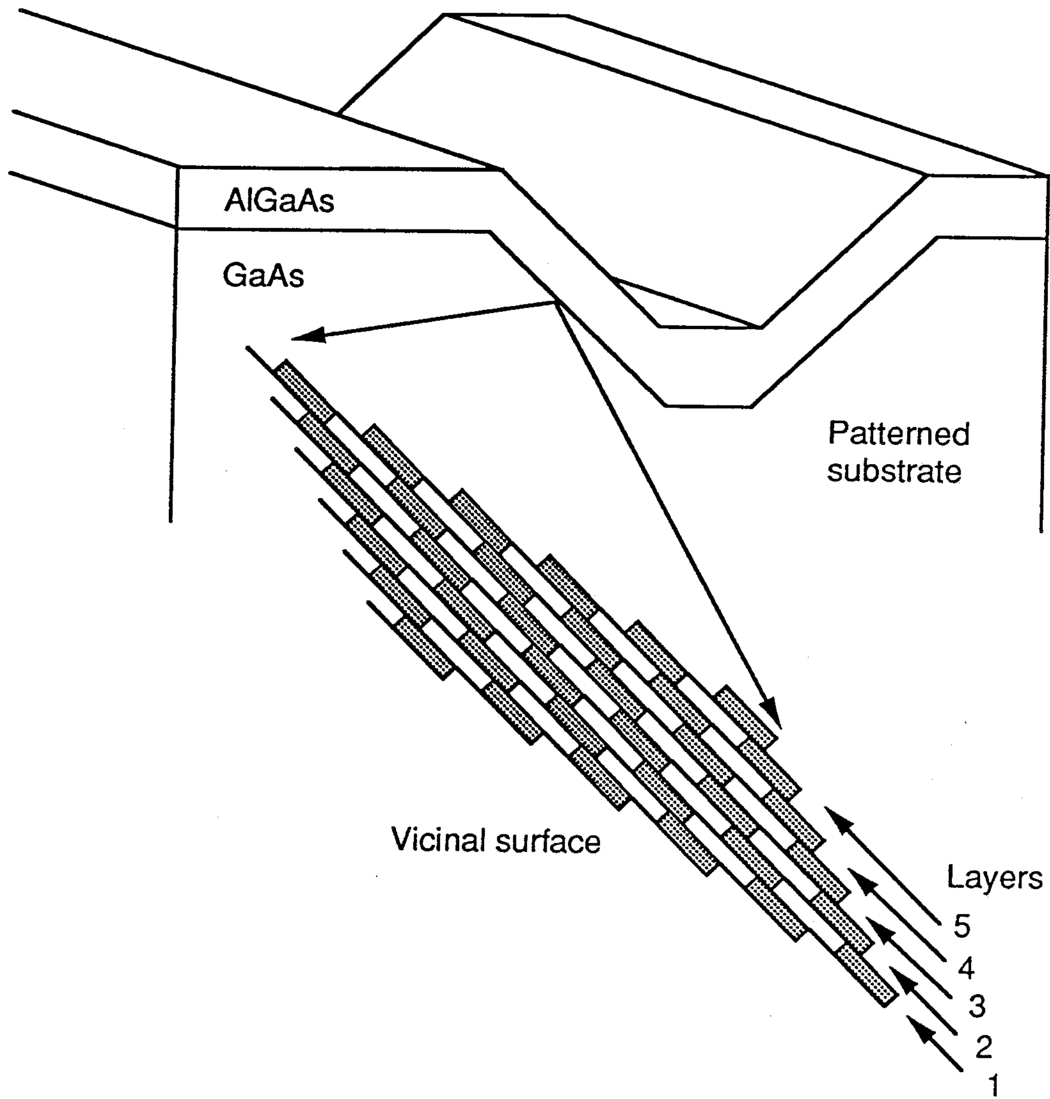

Figure 4.11: Diagram showing deposition of an orientation selective epitaxy superlattice.

$0°$ were installed into the MBE growth chamber, its use would reduce the effective migration length of adatoms on all of the facets, thus reducing or eliminating the appearance of an OSE superlattice. The tilt angle of the OSE superlattice could be varied by adjusting the rate of substrate rotation. This suggests a technique for fabricating a two dimensional array of quantum wires. By periodically increasing the rotation rate, the OSE superlattice could be sharply bent at regular intervals, in such a way as to provide two dimensional confinement of electrons and holes. A more sophisticated variation of the rotation rate might provide a complicated variation of the two dimensional composition. It should be possible to grow an OSE superlattice on a flat substrate by tilting it with respect to the rotation axis. This would require a modification of the substrate holder, which should not be difficult to implement. Finally, the assumptions of the model are not specific to the growth of AlGaAs on patterned substrates. Therefore, it should be possible to apply orientation selective epitaxy to other material systems.

It should be noted that the use of RHEED, a powerful method for monitoring MBE growth, is not possible for an inclined, rotating surface. This will make it more difficult to do a controlled growth of an OSE superlattice. Nevertheless, the experimental results in this thesis show that OSE growth is possible, even under non-optimized conditions. In section 4.6, the feasibility of the model presented in this section will be examined with a Monte Carlo simulation.

4.6 Monte Carlo simulation of orientation selective epitaxy

In section 4.5.6, a mechanism for the growth of an OSE superlattice was presented. Rotation of the substrate was predicted to result in an in-plane variation of the aluminum concentration, during growth by step flow. In this section, results of a Monte Carlo simulation of OSE growth on a step will be presented. We will attempt to address the question of whether or not this mechanism can produce a superlattice, when random variations in the deposition and migration of atoms are allowed.

The purpose of these simulations is to present a model of the growth, in which the kinetic processes relevant to OSE growth can be evaluated in terms of their qualitative importance to the OSE superlattice. We do not intend to derive quantitative conclusions about OSE growth. Quantitative results are precluded by lack of knowledge of the configuration dependent kinetic rates (see section 4.2.3). The simulations presented here are similar to those presented in references [4] and [27]. As in all such simulations, a number of simplifying assumptions are made in order to make the problem tractable. We attempt to retain the kinetic processes which are important for the growth conditions employed in the experiments presented in this thesis.

4.6.1 Parameters of the simulation

The simulations are done on a cubic lattice, with isotropic nearest neighbor hopping probabilities (i. e., nearest neighbor hopping of adatoms is done with the same rate for the two orthogonal directions). This geometry is similar to that of a (100) surface, although the assumption of isotropic hopping is probably not accurate [28]. Surface

reconstruction, neglected in these simulations, may have an effect on the formation of steps and on the kinetic rates [16,29,30]. Simulations of (111) growth, and especially (110) growth, would have to be modified to represent the geometry of the bonds, and the kinetic rates, more accurately.

We consider the growth of a single monolayer at a time. This approximation is justifiable by the conditions of growth, in which the substrate rotation-induced modulation of the beams reproduces the conditions of migration enhanced epitaxy, which has been shown to produce layer by layer growth [5] (see section 4.4). For the same reason, the group V incorporation kinetics are not included explicitly in the simulations. At the growth temperatures employed, desorption of the group III elements is negligible, so these events are also neglected [31].

The kinetic processes considered are random deposition of group III atoms, random migration of group III atoms, and, in some of the simulations, exchange reactions between group III species, stimulated by the release of chemical binding energy during incorporation into the lattice [14]. Kinetic processes are modelled by Arrhenius processes with configuration dependent activation energies, as discussed in section 4.2.3.

The arrival of group III atoms, which is the limiting process determining the growth rate, is governed by the fluxes

$$\overline{F}_i = G_i A, \tag{4.6}$$

where $\overline{F}_i$ is the time-averaged flux of element i, and A is the area of the substrate. The value of G_i is proportional to the arrival rate for element i, and is chosen so that the time for completion of a monolayer corresponds to a specified growth rate for

the crystal. Therefore, for the control growths, in which the fluxes are chosen to be independent of time, the arrival rates are given by $\overline{F}_i$, $i = Ga, Al$ (see equation 4.4). For time dependent fluxes, equations 4.4 and 4.2 determine the instantaneous fluxes, together with the values of $\overline{F}_i$, $i = Ga, Al$. The technique for converting the fluxes into arrival times is discussed in section 4.6.2.

The hopping rates used in our simulations are chosen to correspond to growth on the GaAs (100) surface, because this is the only surface for which the rates have been measured. After Neave et al. and Madhukar et al. [2,4], we choose the hopping to be governed by the rate

$$R_{hop} = h_0 exp[-\frac{(E_{hop} - \Delta)}{kT}]. \tag{4.7}$$

The rate constant, h_0, is chosen to be equal to 8.9×10^{11}, and the activation energy is given by the configuration dependent

$$E_{hop}(i) = N_{As}V_{i-As} + N_{Ga}V_{i-Ga} + N_{Al}V_{i-Al}. \tag{4.8}$$

The interatom binding energies, V_{i-j}, are chosen to give an activation energy of 1.3-1.5 eV for migration on an arsenic (100) plane, with an additional 0.2-0.3 eV for each group III nearest neighbor. The values of N_i are the configuration dependent number of group III and V nearest neighbors present when the hopping event is to occur.

Exchange reactions have been cited as possible causes for segregation in AlGaAs [13,14,4]. For this reason, we have included exchange reactions in some of the simulations, to see what effect they have on the resulting composition. The exchange reactions in our simulations are based on the prescription laid out by Van Vechten [14]. The release of chemical binding energy when an atom is incorporated

into a kink site is presumed to leave the site in an excited state. For a characteristic time, $\tau = 1.0 \times 10^{-7}$ s, the arrival of another atom at the kink site will be affected by this energy release. Gallium atoms, arriving during this time, will also have a high probability of being rejected from the site. Aluminum atoms, arriving at an excited kink site occupied by another aluminum atom, will have the same probability of being rejected. Aluminum atoms, arriving at an excited kink site occupied by a gallium atom, can eject the gallium atom from the kink site, and bind there instead. After the characteristic time expires, the kink site will have dissipated its excess energy.

4.6.2 Simulation algorithm

The simulation follows the prescription outlined in section 4.2.3, which is based on the method of Madhukar and coworkers [4]. Growth is done on a 20×10 substrate, with a step edge at one of the boundaries, and a kink site at the corner. Therefore, the terrace width on the substrate is 10 times the interatomic spacing, and the mean distance between kink sites on the substrate is 20 times the interatomic spacing. Periodic boundary conditions are applied for atoms which migrate out of the area of simulation, so that no atoms are lost or created in the simulation by hopping events. Atoms bind more strongly to the step riser in the first column than in subsequent columns, because of the presence of an extra arsenic bond at these sites. This corresponds to growth on a (100) substrate, with steps aligned to the $[01\bar{1}]$ direction.

The geometry of the MBE chamber is chosen to simulate the growth of the samples in this thesis. The azimuthal angles of the effusion cells, $\Phi_{Ga,Al}$, are chosen to be 33°. The angle of the surface normal is chosen to correspond to growth on a (111) plane,

$\theta = 54.7°$, so that $\theta + \Phi \approx \frac{\pi}{2}$. The in-plane angles of the effusion cells are chosen to be $\gamma_{Al} = -\frac{\pi}{8}$, and $\gamma_{Ga} = \frac{\pi}{8}$, so that the angular separation of the group III cells is $\frac{\pi}{4}$ radians (see section 4.5.3). When the simulations are started, at time $t = 0$, the instantaneous fluxes are equal, and the aluminum flux initially increases, while the gallium flux initially decreases.

The simulation begins at time $t = 0$. The times for arrival of the next gallium and aluminum atoms are selected randomly according to the time dependent fluxes, and these two events are put into an event list. Throughout the growth, events are calculated according to their respective rates, and put into the event list in temporal order. With each iteration of the growth, the first event on the list is done, and the event list is modified by recalculating all events which are thereby affected, and adding any new events to the list which are made possible by the new surface configuration. Therefore, the first event to occur will be the random incorporation of either a gallium or aluminum atom. A hopping event for the new atom will be calculated and added to the list. Every time a new group III atom is incorporated, an event corresponding to the next incorporation of the same type of atom is calculated and added to the list. As each event occurs, the simulation time is incremented to the time at which the current event was scheduled. Thus, group III incorporation events with time dependent rates are calculated based on the current simulation time. Hopping events are calculated based on the local configuration of atoms. When the configuration changes, affected hopping events must be recalculated. This process of iteration allows the surface to evolve, with kinetic rates determined by the local environment.

The simulation is terminated when one monolayer is completed. Because the times for deposition are chosen randomly, the time for termination will vary from simulation to simulation. This corresponds to statistical variation of the local growth rate, which has an important effect on the quality of the interfaces in an OSE superlattice.

In order to select the time at which an event will occur, the time dependent rate must be known. Suppose that the rate governing the occurrence of an event is a function of time, so that at a time, t, the probability that the event will occur during an infinitesimal time, dt, is given by $r(t)dt$. It can easily be shown that, starting from time t_0, the probability, $p(t)dt$, that the next event will occur in the time interval $[t, t + dt]$ is given by

$$p(t)dt = r(t)exp(-\int_{t_0}^{t} r(\tau)d\tau)dt. \tag{4.9}$$

Using a random number generator, a number, x, can be generated with uniform probability, $q(x)dx = dx$, in the interval $[0, 1]$. This can be converted to a time, generated with probability distribution given in equation 4.9, using

$$\int_{x}^{1} q(X)dX = \int_{t_0}^{t} p(T)dT. \tag{4.10}$$

The limits of the integrals were chosen to put the result in its simplest form. Solving equation 4.10 for t, we get

$$\int_{t_0}^{t} r(\tau)d\tau = -ln(x). \tag{4.11}$$

For the calculation of hopping rates, the rate is given by $r(t) = R$, where R is dependent on the configuration, and independent of time. To calculate the group III arrival rates according to time dependent fluxes, we use $r(t) = F_i(t)$, where $F_i(t)$ is

given by equation 4.2, and the time averaged fluxes, defined in equation 4.4, are given by equation 4.6.

If exchange reactions are to be included in the simulation (see section 4.6.1), then the arrival of an atom into a site must be accompanied by a check to see if (1) the site is adjacent to an excited kink site, in which case an exchange or rejection may take place, or (2) the site is a kink site, and should be labeled as excited. In the second case, adjacent sites must be checked to see if they contain atoms which may be affected by the excitation. Furthermore, whenever a site is excited, a de-excitation event must be entered into the event list, to model the dissipation of energy from the excited site.

4.6.3 Results of OSE simulations

Using the algorithm outlined in section 4.6.2, Monte Carlo simulations of OSE growth were carried out. We find that, qualitatively, the results are relatively insensitive to changes in the kinetic rates. The spatial dependence of the aluminum concentration is determined, primarily, by three features of the simulation. First, it is important that the substrate temperature be sufficiently high to allow growth by step flow, as opposed to 2-D nucleation [3]. Second, the time dependence of the fluxes determine the average spatial variation of the aluminum concentration. Third, statistical variations, induced by roughness of the growing step, random variations in the arrival rates, and island

[3] Large differences in the kinetic rates of the two group III species might preclude growth by step flow. Therefore, as in the case of tilted superlattices, an OSE superlattice may not be possible for all material systems [27].

formation, cause local variations in the aluminum concentration which deviate from the average spatial dependence of the composition. Minimization of these clustering effects, by optimization of the growth conditions, may be important to improving the quality of the OSE structures and interfaces.

For each set of parameters, 20 layers were grown in independent simulations. The substrate size was 20×10, with 10 atom wide terraces bounded by steps, as described in section 4.6.2. Average aluminum concentrations were calculated for each of the 10 columns in the terraces. The results of a typical simulation are shown in Figure 4.12, together with a table of the input parameters. For comparison, the aluminum concentration variation for the ideal case is plotted on the same graph, as calculated in section 4.5.6 (see Figure 4.10). For this set of parameters, growth occurs by step flow, and the resulting average composition is close to the ideal value. The composition of columns 9 and 10 are somewhat higher than in the ideal case, because of statistical averaging of the composition of adjacent columns, due to variation of the growth rate and roughness of the steps. We can model this in our calculation of the expected column composition, by extending the limits of the time integral of the fluxes to allow for spatial averaging. Figure 4.13 shows the same data as the last figure, with the averaged column composition. Columns 9 and 10 are consistent with this averaged composition. Column 1, because the simulations are always started at $t = 0$, matches the original plot.

As the roughness of the steps increases (because, for example, the growth temperature in the simulation is reduced), the extent of averaging between adjacent columns

Potentials (hop rates) (eV)						Rotation period (sec)	Growth rates (sec^{-1})	
V_{GaGa}	V_{GaAl}	V_{AlAl}	V_{GaAs}	V_{AlAs}	Δ		Ga	Al
0.20	0.22	0.24	0.65	0.70	0.15	1.2	132	44

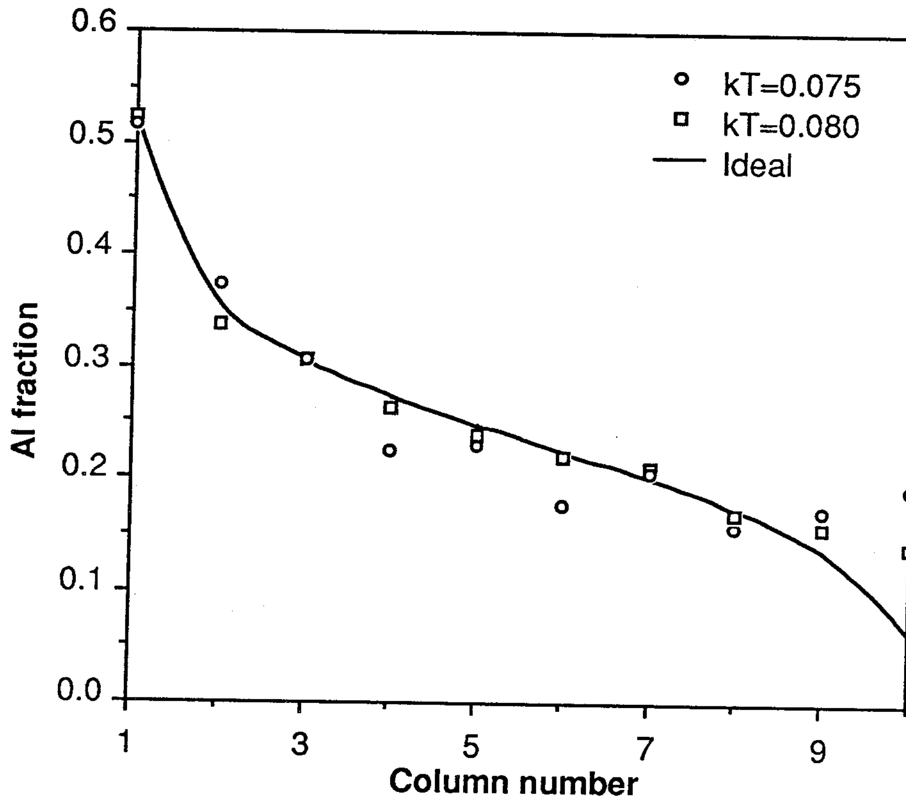

Figure 4.12: Simulated variation of the aluminum concentration in the growth of AlGaAs on a 10 column wide terrace, averaged over 20 independent layers, using the time dependent fluxes expected for orientation selective epitaxy. A plot of the 'ideal' variation of the average aluminum concentration is given for comparison (see text).

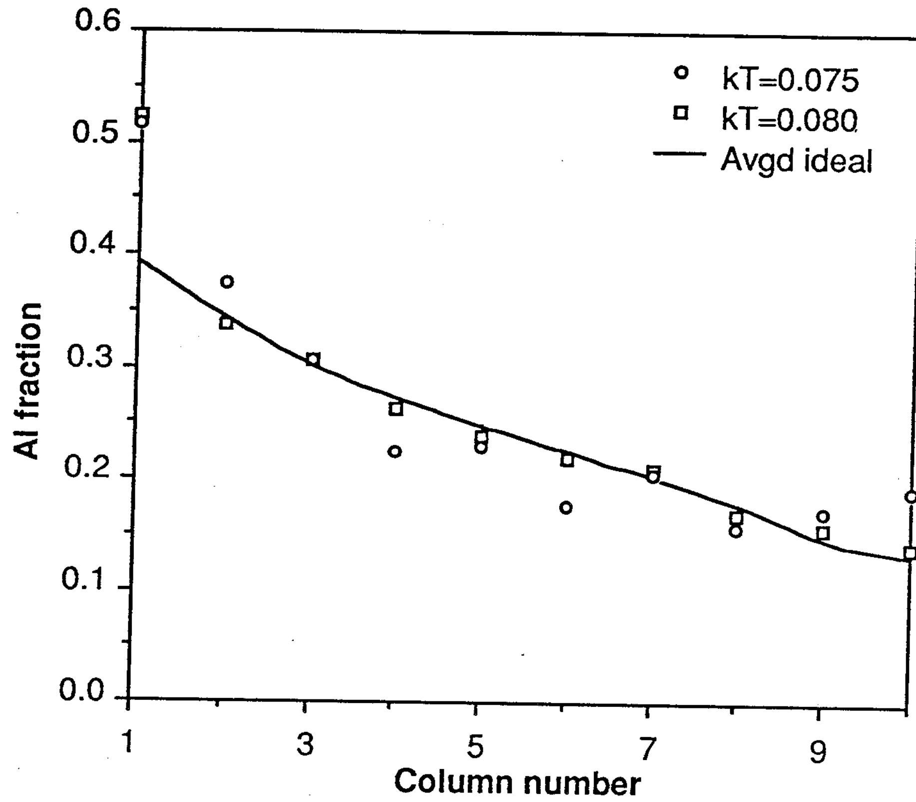

Figure 4.13: Plot of simulation results, compared to an averaged ideal plot, which has been modified to include averaging effects between adjacent columns. The simulation data in columns 9 and 10 match the averaged ideal plot much better than the unaveraged ideal plot.

increases, until islands begin to form. The growths then undergo a transition from step flow to 2-D nucleation, and the averaged composition of the columns becomes uniform across the terrace. In Figure 4.14, the results of simulations in the 2-D nucleation and step flow regimes are shown, in comparison with an averaged ideal plot.

As mentioned in section 4.6.1, some simulations were done which included gallium-aluminum exchange reactions. The exchange reactions made no noticable difference in the qualitative conclusions presented here, and very little difference in the quantitative results. Exchange reactions may play a more significant role in the absence of time dependent fluxes, which dominate the spatial dependence of the composition in these simulations.

When time dependence of the fluxes is neglected, there can still be a small spatial variation of the aluminum concentration, due to the difference in kinetic rates for aluminum and gallium, but the amplitude of the variation is far too small to account for the observed luminescence properties of the OSE growths. This has been observed experimentally in growth of coherent tilted superlattices, as discussed in section 4.4.2. The simulations show a small tendency for aluminum to be incorporated preferentially near the step riser, while the gallium gets pushed toward the step edge (Figure 4.15), but the amplitude of the resulting modulation in composition is insignificant compared to the results of simulations using time dependent fluxes. The amplitude of the compositional modulation resulting from coherent deposition of group III atoms on a stepped surface is not sufficient to have a significant impact on the luminescence

Potentials (hop rates) (eV)						Rotation period (sec)	Growth rates (sec^{-1})	
V_{GaGa}	V_{GaAl}	V_{AlAl}	V_{GaAs}	V_{AlAs}	Δ		Ga	Al
0.25	0.25	0.25	0.70	0.84	0.15	1.2	132	44

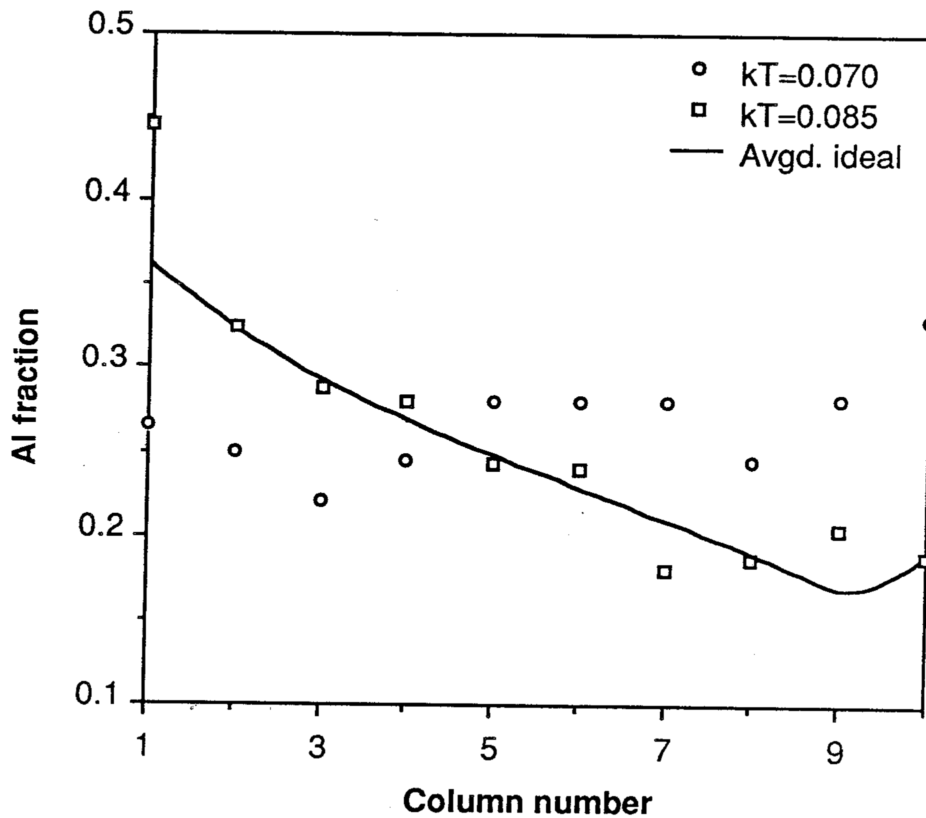

Figure 4.14: Plot of simulations done at two different temperatures, compared to an averaged ideal plot. The lower temperature simulation corresponds to growth by 2-D nucleation, while the higher temperature simulation corresponds to growth by step flow. Note that the appearance of compositional modulation in the growth depends on the conditions being conducive to growth by step flow.

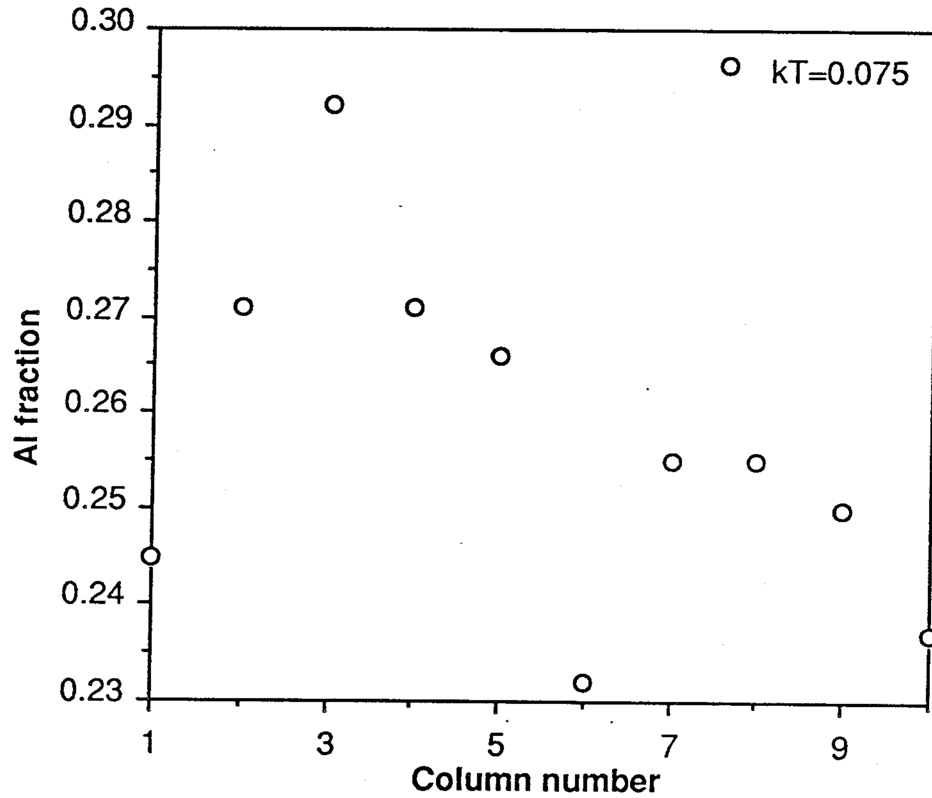

Figure 4.15: Simulation results showing the average spatial dependence of the aluminum fraction, for the case of time independent fluxes. There is a small tendency for aluminum to be incorporated nearer the step riser than gallium.

properties of the AlGaAs alloy. No luminescence data on coherent tilted superlattices have been reported.

4.7 Conclusions

In this chapter, we have presented a model for the growth of a superlattice by orientation selective epitaxy. Based on the nature of molecular beam epitaxy, we concluded that segregation of aluminum and gallium in the growth of AlGaAs is caused by the growth kinetics. We then presented calculations of the time dependence of the arrival of atoms on a surface tilted with respect to the substrate rotation axis, and suggested a mechanism for the growth of an OSE superlattice based on the kinetic consequences of the time dependent fluxes when steps are present on the surface. Finally, the consequences of this mechanism were addressed by a Monte Carlo simulation of growth on a terrace with time dependent fluxes.

The geometrical dependence of OSE superlattice growth suggested several methods for optimization and manipulation of OSE growth. Increasing the angular separation of the group III cells, using larger azimuthal angles for the effusion cells, and varying the rate of substrate rotation are potential methods for controlling the parameters and properties of OSE growth. This suggests a technique for fabricating a two dimensional array of quantum wires. By periodically varying the rotation rate, the OSE superlattice could be sharply bent at regular intervals, in such a way as to provide two dimensional confinement of electrons and holes. More sophisticated variation of the rotation rate might provide a complicated variation of the composition

in two dimensions. It should be possible to grow an OSE superlattice on an unpatterned substrate, by tilting the substrate with respect to the rotation axis. Finally, the assumptions of the model are not specific to the growth of AlGaAs on patterned substrates. Therefore, it should be possible to apply orientation selective epitaxy to other material systems.

The perfection of the interfaces in superlattices grown by orientation selective epitaxy is related to the statistical variations in the growth rate, step roughness, and island formation during the growth. In addition, variation of the step width will have an effect on the period of the superlattices. These issues have a direct effect on the optical properties of the resulting crystal. We have seen in the experimental chapters that the luminescence peak is relatively broad. This is to be expected when there is a significant roughness of the interfaces and variation of the period of a superlattice. In order to improve the quality of structures grown by orientation selective epitaxy, the substrate preparation and crystal growth must be optimized, to ensure that the terrace width is uniform, the step edges are straight, and the growth occurs by step flow. Absolute control of these features is probably impossible, so that the interfaces in OSE superlattices and structures will not be of the same quality as planar heterojunctions grown by MBE. However, the unique capability of OSE for the selective growth of superlattices tilted with respect to the substrate makes OSE a viable candidate for the growth of three dimensional nanometer scale structures.

Bibliography

[1] Masaaki Tanaka and Hiroyuki Sakaki, "Interface roughness of GaAs-AlAs quantum wells grown by molecular-beam epitaxy: Misorientation effects," J. Appl. Phys., **64**, 4503 (1988).

[2] J. H. Neave, P. J. Dobson, B. A. Joyce, and Jing Zhang, "Reflection high-energy electron diffraction oscillations from vicinal surfaces - a new approach to surface diffusion measurements," Appl. Phys. Lett., **47**, 100 (1985).

[3] J. M. Van Hove and P. I. Cohen, "Reflection high energy electron diffraction measurement of surface diffusion during the growth of gallium arsenide by MBE," J. Cryst. Growth, **81**, 13 (1987).

[4] Anupam Madhukar and Subhash V. Ghaisas, "The nature of molecular beam epitaxial growth examined via computer simulations," CRC Crit. Rev. Solid State and Mat. Sci., **14**, 1 (1988).

[5] Yoshiji Horikoshi and Minoru Kawashima, "Growth Mechanism of GaAs during Migration-Enhanced Epitaxy at Low Growth Temperatures," Jpn. J. Appl. Phys., **28**, 200 (1989).

[6] F. Voillet, A. Madhukar, W. C. Tang, M. Thomsen, J. Y. Kim, and P. Chen, "Growth kinetics of molecular beam epitaxially grown GaAs/$Al_{0.3}Ga_{0.7}As$ (100) normal and inverted interfaces in thin single quantum well structures examined via photoluminescence studies," Appl. Phys. Lett., **50**, 194 (1987).

[7] T. S. Kuan, T. F. Kuech, W. I. Wang, and E. L. Wilkie, "Long-Range Order in $Al_xGa_{1-x}As$," Phys. Rev. Lett., **54**, 201 (1985).

[8] P. M. Petroff, A. Y. Cho, F. K. Reinhart, A. C. Gossard, and W. Wiegman, "Alloy Clustering in $Ga_{1-x}Al_xAs$ Compound Semiconductors Grown by Molecular Beam Epitaxy," Phys. Rev. Lett., **48**, 170 (1982).

[9] A. Zur and T. C. McGill, "Theoretical investigation of the effect of strain on phase separation in epitaxial layers," J. Vac. Sci. Technol., **B3**, 1055 (1985).

[10] G. P. Srivastava, Jose Luis Martins, and Alex Zunger, "Atomic structure and ordering in semiconductor alloys," Phys. Rev. B, **31**, 2561 (1985).

[11] J. S. Cohen and A. G. Schlijper, "Long-range order in $Al_xGa_{1-x}As$," Phys. Rev. B, **36**, 1526 (1987).

[12] J. M. Gaines, P. M. Petroff, H. Kroemer, R. J. Simes, R. S. Geels, and J. H. English, "Molecular-beam epitaxy growth of tilted GaAs/AlAs superlattices by deposition of fractional monolayers on vicinal (001) substrates," J. Vac. Sci. Technol., **B6** 1378 (1988).

[13] A. Madhukar, "Far from equilibrium vapour phase growth of lattice matched III-V compound semiconductor interfaces: some basic concepts and monte-carlo

computer simulations," Surface Science, **132**, 344 (1983).

[14] J. A. Van Vechten, "Kinetic segregation of AlAs-GaAs during $< 110 >$ MBE," J. Cryst. Growth, **71**, 326 (1985).

[15] W. I. Wang, T. S. Kuan, J. C. Tsang, L. L. Chang, and L. Esaki, "Segregated AlGaAs(110) grown by molecular beam epitaxy," J. Vac. Sci. Technol. B, **4**, 517 (1986).

[16] S. B. Ogale, M. Thomsen, and A. Madhukar, "Role of surface reconstruction and external ion beam in the growth kinetics of III-V molecular beam epitaxy," *Initial Stages of Epitaxy*, Vol. 94, MRS Proceedings, Hull, R., Ed., pp. 83-90 (1987).

[17] P. M. Petroff, A. C. Gossard, and W. Wiegmann, "Structure of AlAs-GaAs interfaces grown on (100) vicinal surfaces by molecular beam epitaxy," Appl. Phys. Lett., **45**, 620 (1984).

[18] Takashi Fukui and Hisao Saito, "$(AlAs)_{0.5}(GaAs)_{0.5}$ fractional-layer superlattices grown on (001) vicinal surfaces by metalorganic chemical vapor deposition," Appl. Phys. Lett., **50**, 824 (1987).

[19] P. M. Petroff, J. Gaines, M. Tsuchita, R. Simes, L. Coldren, H. Kroemer, J. English, and A. C. Gossard, "Band gap modulation in two dimensions by MBE growth of tilted superlattices and applications to quantum confinement structures," J. Cryst. Growth, **95**, 260 (1989).

[20] P. R. Pukite, G. S. Petrich, S. Batra, and P. I. Cohen, "The meandering of steps on GaAs(100)," J. Cryst. Growth, **95**, 269 (1989).

[21] M. Tsuchiya, P. M. Petroff, and L. A. Coldren, "Spontaneous growth of coherent tilted superlattice on vicinal (100)GaAs substrates," Appl. Phys. Lett., **54**, 1690 (1989).

[22] W. T. Tsang and A. Y. Cho, "Growth of GaAs-$Ga_{1-x}Al_xAs$ over preferentially etched channels by molecular beam epitaxy: A technique for two-dimensional thin-film definition," Appl. Phys. Lett., **30**, 293 (1977).

[23] H. P. Meier, E. Van Gieson, W. Walter, C. Harder, M. Krahl, and D. Bimberg, "Molecular beam epitaxy of GaAs/AlGaAs quantum wells on channeled substrates," Appl. Phys. Lett., **54**, 433 (1989).

[24] S. N. G. Chu, N. Chand, D. L. Sivco, and A. T. Macrander, "Substrate rotation-induced composition modulation in epitaxial AlGaAs grown by molecular-beam epitaxy," J. Appl. Phys., **65**, 3838 (1989).

[25] K. Alavi, P. M. Petroff, W. R. Wagner, and A. Y. Cho, "Substrate rotation-induced compositional oscillation in molecular beam epitaxy (MBE)," J. Vac. Sci. Technol., **1**, 146 (1983).

[26] I. Sela, V. V. Gridin, R. Beserman, R. Sarfaty, D. Fekete, and H. Morkoç, "Distribution of atoms in mixed III-V compounds," J. Appl. Phys., **63**, 966 (1988).

[27] K. J. Hugill, S. Clarke, D. D. Vvedensky, and B. A. Joyce, "Quantum-well-wire growth by molecular-beam epitaxy: A computer simulation study,"

J. Appl. Phys., **66**, 3415 (1989).

[28] Kimihiro Ohta, Takeshi Kojima, and Tadashi Nakagawa, "Anisotropic surface migration of Ga atoms on GaAs (001)," J. Cryst. Growth, **95**, (1989).

[29] D. L. Rode, "Crystal growth terraces and surface reconstruction," J. Cryst. Growth, **27**, 313 (1974).

[30] D. K. Choi, T. Halicioglu, and W. A. Tiller, "Surface stress tensor mediation of the ledge nucleation/growth process with the surface reconstruction process in GaAs," *Initial Stages of Epitaxy*, Vol. 94, MRS Proceedings, Hull, R., Ed., pp. 91-96 (1987).

[31] R. Fischer, J. Klem, T. J. Drummond, R. E. Thorne, W. Kopp, H. Morkoç, and A. Y. Cho, "Incorporation rates of gallium and aluminum on GaAs during molecular beam epitaxy at high substrate temperatures," J. Appl. Phys., **54**, 2508 (1983).

Chapter 5

Orientation selective epitaxy: Dependence on groove orientation

5.1 Introduction

We have seen in Chapter 3 that orientation selective epitaxy can be used to selectively grow a superlattice on the sides of grooves in a (100) GaAs substrate. In addition, an abrupt heterojunction was observed oriented lateral to the growth direction, at the boundary between adjacent facets. These results suggested possible application of growth on patterned substrates to achieve *in situ* growth of two or three dimensional structures, with bandgap modulation on a nanometer scale.

The experimental results thus far have been limited to growth on grooves parallel to the $[01\bar{1}]$ direction. In this chapter, we present results of measurements on the dependence of the bandgap on groove orientation. The purpose of this measurement is to more fully characterize orientation selective epitaxy. In particular, we want to

test the possibility of bandgap tuning by varying the substrate orientation.

5.2 Orientation selective epitaxy: Variation of groove orientation

Three new growths will be discussed in this chapter, NSI1, NSI2, and NSI3. The geometry and conditions in the growth of MBE 815, discussed in Chapter 3, are most closely duplicated in NSI1. The relative orientations of the effusion cells are similar, the layer thicknesses are the same, and the growth rate has been adjusted so that the ratio of the growth rate to the substrate rotation rate is roughly the same as for MBE 815. Measurements on the new samples confirm the results of Chapter 3, and provide additional information on the nature of OSE growth.

5.2.1 Sample preparation

In order to study in detail the dependence of orientation selective epitaxy on the groove orientation, substrates were prepared with grooves varying in orientation between $[01\bar{1}]$ and $[011]$, using the procedure outlined in Chapter 3 (see Figure 5.1). Growth of the epilayers was done in a Varian GEN II molecular beam epitaxy machine, with a substrate temperature of 600°C. The $Al_{0.25}Ga_{0.75}As$ growth rate was 0.88 μm/h. The growth of sample NSI1 consists of a 1 μm GaAs buffer layer, followed by a 1 μm $Al_{0.25}Ga_{0.75}As$ layer. Samples NSI2 and NSI3 consist of a 0.5 μm GaAs buffer layer, followed by 0.5 μm $Al_{0.25}Ga_{0.75}As$ layer. In these growths, the gallium and aluminum cells were separated by $\frac{\pi}{4}$ radians, in the projection onto the

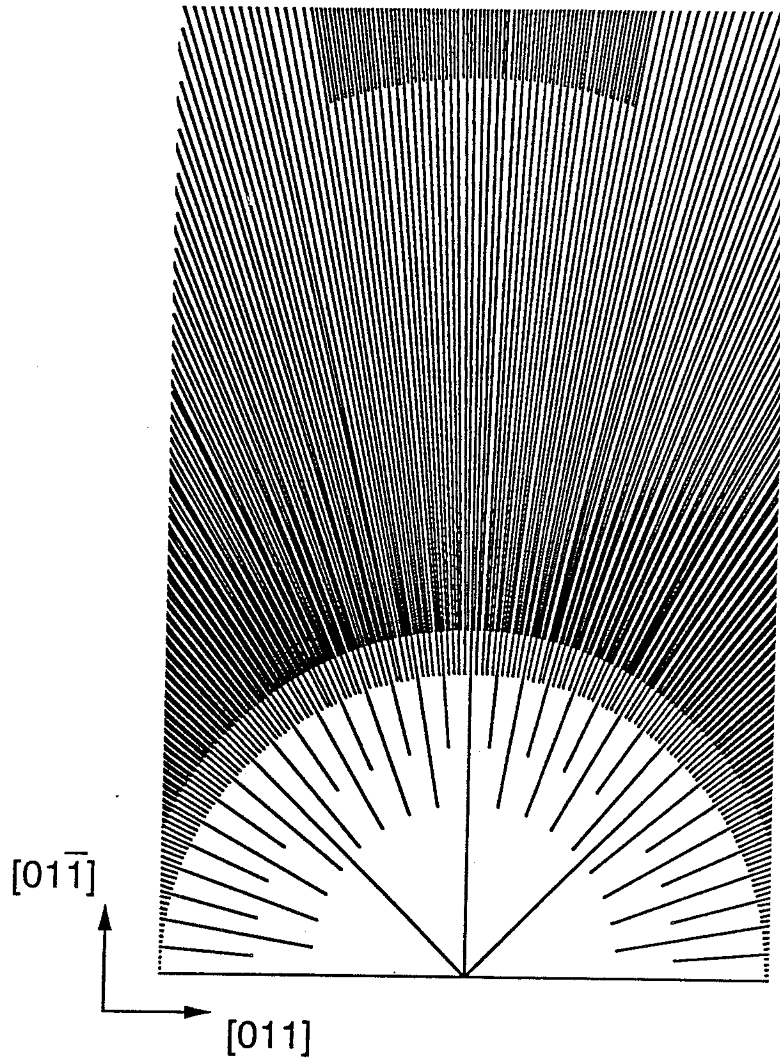

Figure 5.1: Schematic representation of the pattern of grooves etched into samples NSI1, NSI2, and NSI3. The grooves are approximately 15 μm wide and 5 μm deep. This arrangement of grooves provides the means for a systematic study of the dependence of OSE growth on groove orientation.

(100) plane. All layers were undoped.

5.2.2 Orientation considerations

As the angle of the groove, relative to the $[01\bar{1}]$ groove, changes from 0° to 90°, the facets exposed by the chemical etch change orientation. The facets which appear depend on the chemical etchant, and on the conditions and duration of the etch. Because selective etches tend to cause pitting of the surface, the etchant which we have chosen is a slow, nonselective etch. The cross section of grooves oriented near 0° and 90° has a flattened "V" shape, with straight sides and a flat bottom. This is a similar profile to that observed in the growths of Chapter 3. Grooves oriented near 45° have a more rounded profile, with a gradual transition between the sides and bottom of the grooves.

The growths exhibit some variation of the surface morphology in the grooves, and in luminescence characteristics. The differences in morphology of the three samples, and the differences in luminescence characteristics, may be due to variation in either the etch conditions or the MBE growth conditions. Orientation selective epitaxy is sensitive to the surface profile in the groove, which may in turn depend upon the conditions of the etch. In particular, small misorientations can have a significant effect on the quality of epitaxial growth on a {110} surface [1]. The etch rate is quite sensitive to the concentration of H_2O_2, which changes as the etchant ages. Uncertainty in adjusting the substrate temperature and growth rate in MBE may result in a slight variation of the growth conditions for the samples studied.

5.3 Cathodoluminescence of grooves: Dependence on surface orientation

Cathodoluminescence scanning electron microscopy of these samples reveals a dependence of the peak AlGaAs emission on surface orientation. The position of the cathodoluminescence peak, as a function of groove angle, is shown in Figure 5.2, for NSI1. The epitaxial layers luminesce strongly, indicating that the quality of the growth is good. The positions of the luminescence peaks are to be compared to the luminescence peak from the unpatterned (100) AlGaAs, which occurs at 669 nm for NSI1, 672 nm for NSI2, and 663 nm for NSI3. Emission from the sides of the grooves is, in general, considerably stronger than emission from the unpatterned (100) AlGaAs epilayers. Red shifts, relative to luminescence from the unpatterned regions, are observed on the side facets of most groove orientations. The largest shifts, and the strongest luminescence, are observed in grooves oriented between 40° and 45°. In addition, some grooves exhibit strong blue shifts in NSI3.

For all three samples, the position of the luminescence peak from the side facets is nearly independent of groove orientation from 0° to 20° and from 70° to 90°. Between 20° and 60°, the position of the luminescence peak depends on the groove orientation. The samples exhibit different faceting characteristics in this range of angles. Samples NSI1 and NSI2, in which the faceting is similar, have a similar dependence of the luminescence on groove angle. Sample NSI3 has both different faceting behavior and different luminescence characteristics.

Monotonic dependence of the bandgap on surface orientation is observed for some

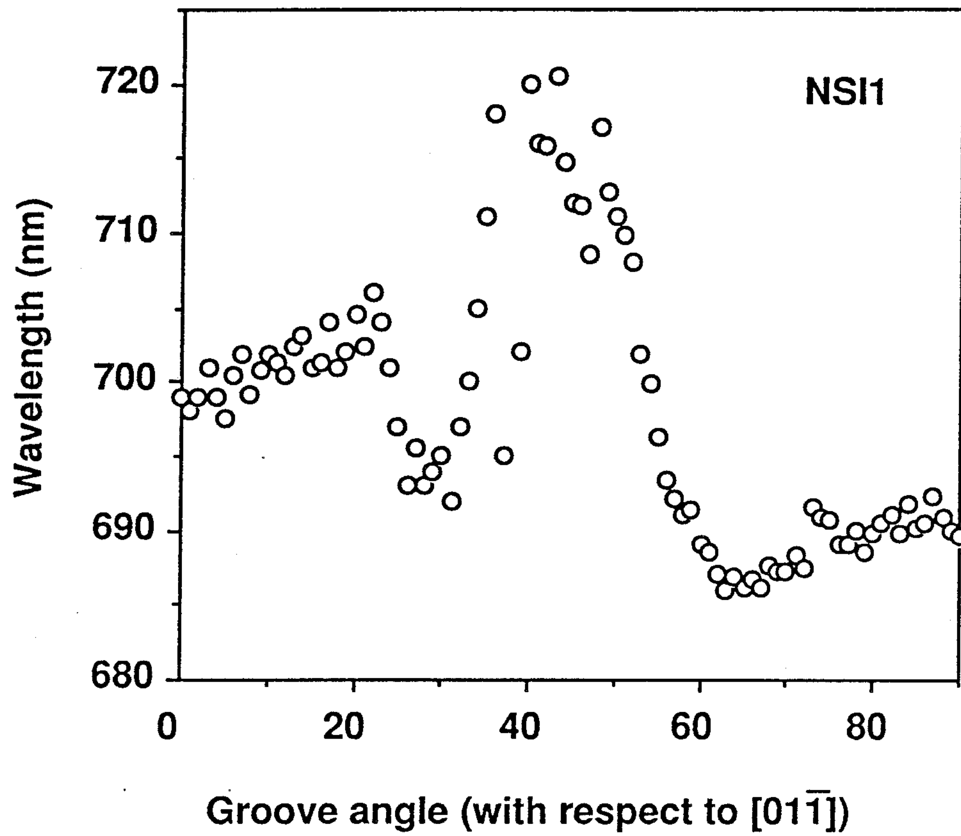

Figure 5.2: Plot of the AlGaAs peak as a function of groove orientation, relative to the [01$\bar{1}$] groove, for sample NSI1. The unpatterned AlGaAs luminesces at 669 nm in this sample.

ranges of groove angles in these samples. For the side facets, NSI1 shows a shift in the luminescence peak from 687 nm in the 62° groove, to 717 nm in the 48° groove. The surface morphology in this range of groove angles is very good. Similarly, NSI2 exhibits a dramatic shift in the luminescence peak for grooves between 50° and 45°. In the 50° groove, the peak occurs at 687 nm and by the 45° groove, the peak has shifted to 745 nm. This represents a difference of 140 meV in the effective bandgap for a mere 5° change in groove angle. Grooves in the range 46°-55° have good surface morphology, but in the 45° groove, some faceting is evident. Sample NSI3 has a much smaller dependence of the luminescence peak on groove orientation in this range of angles. As indicated by the lack of faceting characteristic of growth on misoriented (110) surfaces, which was observed in NSI1 and NSI2, this is probably due to a different groove profile in NSI3.

The top facet, which is distinct from the side facet in grooves from 0° to approximately 40°, also exhibits a strong dependence of the bandgap on groove orientation. Again, NSI1 and NSI2 are similar, while NSI3 has markedly different properties. In the 30° groove of NSI1, the top facet exhibits peak luminescence at 660 nm. As the groove angle changes from 30° to 39°, the luminescence peak shifts to 697 nm. In NSI2, from the 27° to the 33° grooves, the luminescence peak shifts from 662 nm to 687 nm. In NSI3, the top facet first appears in the 41° groove, where it has a luminescence peak at 621 nm. Compared to the 663 nm peak of AlGaAs grown on unpatterned regions of this sample, this is the strongest blue shift observed in any of the growths. From the 41° to the 35° grooves, the luminescence shifts to 650 nm.

Between 35° and 25°, the peak shifts toward 638 nm.

Because luminescence from low bandgap material is expected to dominate in cases of adjacent areas of low and high bandgap, it is interesting that emission from the top facet in NSI3 is blue-shifted relative to unpatterned growth, from groove angles 0° to 40°. NSI1 and NSI2 emit blue-shifted luminescence for some of the grooves in this range of angles, but the magnitude of the shifts is much smaller, and occurs in a limited range of groove angles (25° to 30°). In some cases, the peak in NSI3 is shifted by 40 nm (120 meV) to shorter wavelengths, relative to luminescence from unpatterned areas of the sample. In addition, the blue-shifted emission appears to emanate uniformly from the top facet, rather than being localized to growth near perturbations in the surface. In fact, the diagonal facets crossing the surface are associated with localized emission at longer wavelengths. Because the dominant emission is blue-shifted, the aluminum fraction must be higher than the nominal value in a significant fraction of the AlGaAs in the top facets. This suggests that surface diffusion is responsible for the low aluminum concentration in the top facet of grooves in NSI3. Significant surface diffusion at this growth temperature, 600°C, is surprising. The excess gallium may be accumulating at the edge of the facet or in the diagonal facets, where localized red shifts are observed.

Significant scatter in the position of the luminescence peak is associated with rough surfaces and/or faceting in the corresponding grooves. This is the case, for example, for grooves between 25° and 45° in NSI1 and NSI2, between 60° and 90° in NSI2, and between 0° and 20° in NSI3. Faceting of growth is particularly important to consider

in orientation selective epitaxy. In addition to the dependence of orientation selective epitaxy on the azimuthal angle of the surface normal (see Chapter 4), the chemistry on different facet orientations may affect the composition, and interfacet diffusion may affect the relative composition of adjacent areas in the growth. Luminescence from a faceted surface is expected to be dominated by the facets with the lowest bandgap. In our cathodoluminescence measurements, differences in the surface morphology are associated with different luminescence characteristics. This association can be dramatic, as in the case of diagonal facets crossing the sides of grooves in samples NSI1 and NSI2, for grooves between 35° and 45°. Such facets can have emission peaks red-shifted by as much as 1000Å, relative to luminescence from AlGaAs grown on the unpatterned (100) substrate.

A dramatic illustration of the spatial dependence of the luminescence in the presence of faceting is given by the 38° groove in NSI2, and the 39° groove in NSI3. Both samples exhibit faceting which is associated with strong red shifts of the luminescence. The facets are accompanied by localized, very bright luminescence. CL images show bands of red-shifted luminescence following diagonal facets in these grooves. In NSI2, spectra taken from adjacent areas have peaks at 707 nm and 770 nm, representing a difference in bandgap energy of 144 meV. In NSI3, the luminescence from a diagonal facet has a peak at 689 nm, while luminescence away from this facet has a peak at 642 nm. This represents a shift in energy of 132 meV. The magnitude of the shifts in these samples is about the same.

5.4 Transmission electron microscopy

Transmission electron microscopy was used to look at the composition of samples NSI1, NSI2, and NSI3. The sample preparation and diffraction conditions are described in Chapter 3. Because of practical considerations regarding sample preparation and imaging in the microscope, only grooves oriented roughly along the $[01\bar{1}]$ and [010] directions were studied. The results of the TEM measurements confirm the results of Chapter 3. Two new results will be discussed in this section.

The sides of $[01\bar{1}]$ grooves in NSI2 are observed to consist of a wide (211) facet, and a narrow (111) facet adjacent to the bottom of the groove. Strong compositional modulation is observed on the (111) facet, similar to that observed in Chapter 3. The (211) facet shows some interesting features. Compositional modulation in other samples has been observed to intersect the substrate/epilayer interface, but at a relatively shallow angle. In the (211) facet, there is a 22° angle between the planes of compositional modulation and the substrate/epilayer interface (see Figure 5.3). Furthermore, the contrast is observed to be stronger for compositional modulation in the vicinity of small (111) facets in the surface. A possible explanation for this enhancement of the modulation, based on the model discussed in Chapter 4, is that the amplitude of the rotation-induced flux modulation is larger near the (111) facets, due to locally enhanced shadowing of the fluxes.

In the side facet of a groove oriented approximately along the [010] direction in NSI3, we observe quantum wire-like structures showing very strong contrast, with a width of approximately 60Å (see Figure 5.4). Narrow bright bands, oriented ap-

proximately parallel to the (101) facet, run through the epilayers. The bands are continuous for length scales of up to a micron, and they appear to terminate at perturbations, or small facets, in the substrate/epilayer interface and the surface. The contrast indicates that these bands are aluminum rich; however, their origin is unknown. Wire-like structures are observed as an array of Ga-rich and Al-rich layers, which are terminated by the narrow Al-rich bands. The phase between wire structures in adjacent layers varies during the growth.

In the bottom of the groove, and in AlGaAs grown on unpatterned (100)GaAs, we observe a weak superlattice, which is due to an external modulation of the fluxes. The external modulation is attributed to a small fluctuation in the temperature(s) of one or both of the group III effusion cells. The period of the external modulation is short (approximately 25Å on the bottom of the groove). One possible explanation for the wire-like structures is superposition of the external modulation and the Al-rich bands discussed in the last paragraph.

5.5 Discussion

The results presented in this chapter have verified the observations in Chapter 3, regarding orientation selective epitaxy in a $[01\bar{1}]$ groove. The dependence of orientation selective epitaxy on the substrate orientation was examined by changing the orientation of the grooves. We found that the bandgap of AlGaAs grown in a groove depends on surface orientation for grooves between 20° and 60° (relative to the $[01\bar{1}]$ groove), but outside this range, the bandgap is relatively independent of groove ori-

entation. Both red-shifted and blue-shifted luminescence is observed in the samples, with the strongest shifts occuring in grooves oriented between 40° and 45°. Faceting in the surface has a strong effect on the luminescence of AlGaAs. This is probably due to a combination of differences in Al-Ga segregation on the differently oriented facets, and interfacet diffusion during growth. The bandgap of AlGaAs exhibits a monotonic shift with respect to groove angle, in some ranges of groove orientations. This shows that it is possible to tune the bandgap of OSE growth by varying the surface orientation.

Transmission electron micrographs of sample NSI2 show compositional modulation which intersects the substrate at an angle of 22°. While the modulation has been observed to intersect with the substrate in other grooves, this is the largest misorientation between the compositional modulation and the growth plane which we have observed. Misorientation with respect to the growth plane rules out mechanisms for orientation selective epitaxy which would produce modulation along the growth direction. This misorientation is consistent with the predictions of the model presented in Chapter 4.

Quantum wire-like structures were observed in sample NSI3, in a groove oriented approximately along the [010] direction. The structures, which are approximately 60Å in size, are well defined and exhibit strong contrast between the gallium- and aluminum-rich regions. The formation of these structures is not yet understood. The existence of quantum wire-like structures on this size scale, with strong, well-defined variation in the aluminum concentration, demonstrates that orientation selective epi-

taxy is a viable technique for the fabrication of higher dimensional nanometer scale structures.

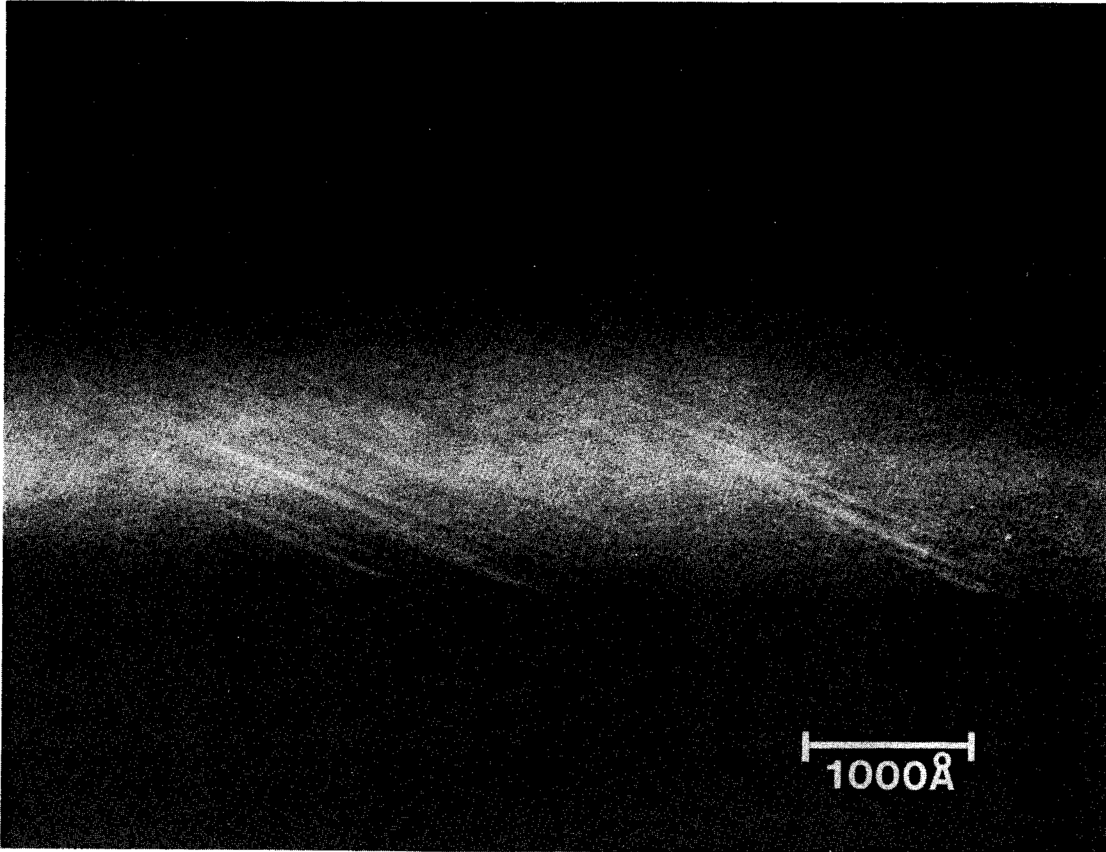

Figure 5.3: Transmission electron micrograph, taken using the (200) dark field condition, of AlGaAs grown on the (211) facet of an $[01\bar{1}]$ groove, in sample NSI2. Compositional modulation in these layers is observed to intersect the substrate at an angle of 22°. The substrate/epilayer interface contains small (111) facets, approximately 250 μm in length, which are associated with an enhancement in the amplitude of the compositional modulation (see text).

Figure 5.4: Transmission electron micrograph, taken using the (200) dark field condition, of AlGaAs grown on the side of a [010] groove. Quantum wire-like structures are observed, with a width of approximately 60Å.

Bibliography

[1] L. T. P. Allen, E. R. Weber, J. Washburn, Y. C. Pao, and A. G. Elliot, "Characterization of surface faceting on (110)GaAs/GaAs grown by molecular beam epitaxy," J. Cryst. Growth, **87**, 193 (1988).

Chapter 6

Orientation selective epitaxy in oval defects

6.1 Introduction

There has been a great deal of interest recently in MBE growth on different substrate orientations. This interest was fueled by the discovery that growth on substrates which were slightly misoriented from (100) yielded material with improved electronic and optical properties, and additionally by the discovery that (111) oriented quantum wells were significantly better than (100) quantum wells for laser diode applications. Growth on nonplanar substrates, which involves simultaneously several surface orientations, has generated some interesting results, and is a promising technique for introducing lateral variation into epitaxial growth (see Chapters 3, 4, and 5). Because the formation of oval defects involves growth on nonplanar surfaces and the formation of facets, the properties of oval defects are relevant to these issues in MBE

growth.

In this chapter, we present cathodoluminescence data on oval defects in five different samples. The defects studied are of the α_3 and α_4 types, as described by Fujiwara et al. [1]. We examine the spatial variation of the luminescence of $Al_xGa_{1-x}As$ epilayers within oval defects. Comparison of the luminescence of oval defects with growth on a patterned substrate reveals some similarities in the spectral emission of AlGaAs in oval defects and grooves. We therefore consider the possibility that orientation selective epitaxy is responsible for some of the observed spectral characteristics of AlGaAs in faceted MBE growth, and, in particular, oval defects.

6.2 Oval defects in $Al_xGa_{1-x}As$ grown by MBE

In crystal growth by molecular beam epitaxy, the most common macroscopic defects are oval shaped hillocks (oval defects), appearing in an otherwise planar surface. Oval defects are common in crystals grown by molecular beam epitaxy, and pose a serious problem in the fabrication of circuits and devices. The characteristic shape of an oval defect results from facet dependent growth rates on a nonplanar surface [2]. The defects exist in a variety of types, ranging in size from a few microns to tens of microns, and differing in morphology. The defect types are distinguished by their origin. Within a given type, the morphology depends on the thickness of the epilayers and the growth conditions.

Because they are all roughly oval in shape, and despite the dramatic differences in morphology and probable origin, the various defect types have been lumped under

the general classification of "oval defects." This generalization has led to a variety of claims regarding *the* origin and properties of oval defects. Several mechanisms have been proposed for the origin of "oval defects," including spitting from the gallium cell [3,4], contamination on the substrate surface (particulates, impurities, or oxides) [5,6], and contamination in the effusion cells [6]. In an important classification of oval defect types, Fujiwara et al. [1] have attempted to cut through the confusion by distinguishing between defect types when considering the issue of the origin of oval defects. The oval defects studied in this chapter are of the α_3 and α_4 types, which were attributed to anomalous enhancement of the GaAs growth rate due to localized accumulation of excess gallium [1]. The crystalline quality inside oval defects of these types has been found to be good [7].

While GaAs oval defects have been studied extensively, there have been only a few studies of $Al_xGa_{1-x}As$ in oval defects. Recent spectroscopic investigations have revealed a variation of the aluminum concentration of $Al_xGa_{1-x}As$ epilayers in oval defects of the α_3 and α_4 types [7,8,9,10]. It was found that the aluminum concentration is lower in the defects, compared to the surrounding $Al_xGa_{1-x}As$. Raman spectroscopy measurements showed that the aluminum concentration is slightly enhanced at the surface of these oval defects, and that the crystalline orientation of material in the defects differs from the orientation outside the defects [7].

While the observation of an enhanced gallium concentration is consistent with the proposed mechanism for the origin of α_3 and α_4 oval defects [1], there is no direct evidence that the variation of aluminum concentration is related to the defect origin.

In the following sections, the variation of aluminum concentration in oval defects of five samples will be studied in detail.

6.3 Experimental results

6.3.1 Sample MBE 562

The first sample studied was MBE 562. Growth was done at a substrate temperature of 650°C. The structure consists of a 500Å Be-doped $Al_{0.28}Ga_{0.72}As$ surface layer, a 100Å undoped $Al_{0.28}Ga_{0.72}As$ layer, an undoped 130Å quantum well, a 100Å undoped $Al_{0.28}Ga_{0.72}As$ layer, a 0.64 μm Si-doped $Al_{0.28}Ga_{0.72}As$ layer, a superlattice buffer layer, and a 0.75 μm Si-doped GaAs layer. The growth has a high density of oval defects (about 4×10^5 cm^{-2}), which are of the α_4 type. Room temperature cathodoluminescence data from this growth have been presented elsewhere [8,9].

The defects in this sample are approximately 5 μm long and 3 μm wide, with a pit in the center (see Figure 6.1). Phase contrast optical microscopy of the oval defects shows a circular area surrounding the each defect, $\approx$ 10 μm in diameter, which is slightly tilted with respect to the nominal (100) growth direction. Due to its shape and luminescence properties (see Figure 6.1.c), we refer to this area as the halo. Cathodoluminescence images and spectra of this sample at 77 K and 13 K reveal a strong variation of the composition of the AlGaAs in the vicinity of the defects. Figure 6.1 shows spectrally resolved cathodoluminescence images of the defects at 77 K, at 6400Å, 6700Å, and 7100Å. At the peak of the AlGaAs emission from the sample, luminescence from the oval defects (including the halo) is weak. The halo

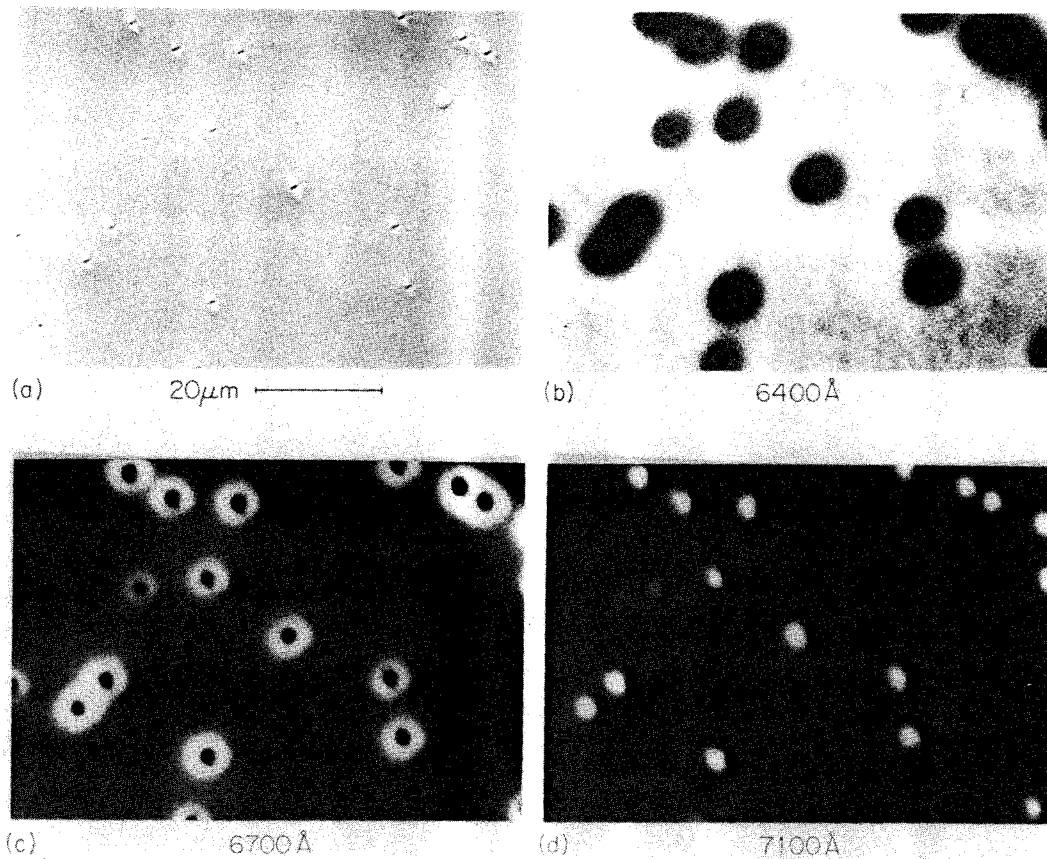

Figure 6.1: Oval defects in MBE 562 exhibit strong spatial dependence of the cathodoluminescence emission.

(a) Secondary electron image of the sample, showing a high density of oval defects.

(b) Cathodoluminescence image, taken at 77 K, at a wavelength of 6400Å. This wavelength corresponds to the peak of the $Al_{0.28}Ga_{0.72}As$ spectrum. Luminescence is weak in the vicinity of oval defects at this wavelength.

(c) Cathodoluminescence image, taken at 77 K, at a wavelength of 6700Å. At this wavelength, the halo regions of the oval defects luminesce strongly.

(d) Cathodoluminescence image, taken at 77 K, at a wavelength of 7100Å. At this wavelength, the centers of the defects luminesce strongly.

luminesces strongly at a somewhat longer wavelength, 6700Å, but the center of the defect remains dark at this wavelength (Figure 6.1.c). At 7100Å, the centers of the defects exhibit strong luminescence.

Cathodoluminescence spectra quantify the spatially dependent emission observed in the CL images. Figure 6.2 shows a luminescence spectrum of a defect. The defect-free spectrum exhibits a broad peak at 8195Å, which is identified as the superposition of luminescence from the quantum well, the superlattice, and the GaAs substrate and buffer layer. The luminescence peak at 6467Å corresponds to the $Al_{0.28}Ga_{0.72}As$ layers. The oval defect spectrum shows little change in the 8195Å peak, compared to the defect-free spectrum. The halo has a broad luminescence peak at approximately 6800Å. The strong luminescence peak at 7147Å originates in the center of the defect. No luminescence was observed from AlGaAs with a higher aluminum concentration than 0.28 in this sample. This is not conclusive evidence that the oval defects contain only AlGaAs with an enhanced gallium concentration, because the bandgap of AlGaAs becomes indirect at $x \approx 0.37$ at this temperature, and the luminescence efficiency becomes worse as the aluminum concentration approaches this value [11].

6.3.2 Sample MBE 775

The next sample studied was MBE 775. The growth consists of a 0.1 μm GaAs buffer layer, and a 2.3 μm Si-doped $Al_{0.07}Ga_{0.93}As$ layer grown on a semi-insulating GaAs substrate. The oval defects in this sample are primarily of the α_3 and α_4 types, with a wide variety of external features. The defects have in common an oval shape, with the long axis oriented along the $[01\bar{1}]$ direction. There is a ridge running

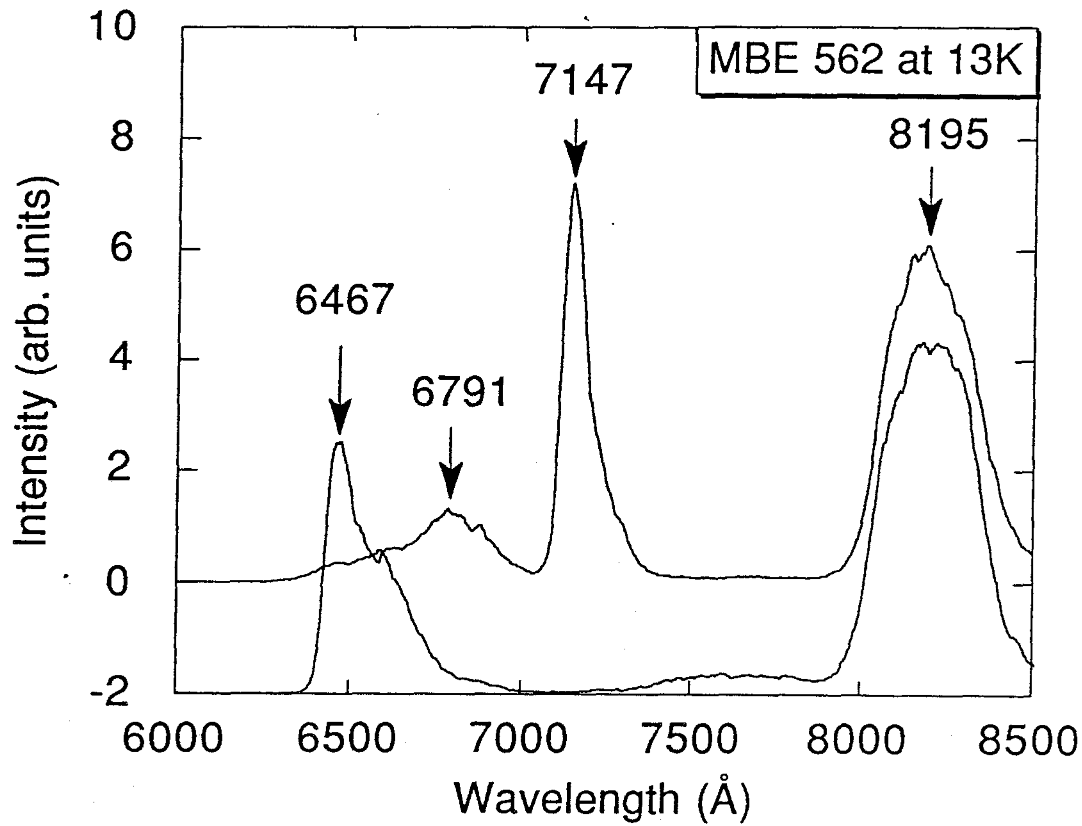

Figure 6.2: Cathodoluminescence spectra of MBE 562, showing the luminescence peaks emitted by oval defects. The spectra were taken at 13 K. The upper spectrum shows luminescence from the center of an oval defect. For comparison, the lower spectrum shows luminescence from a defect-free area of the sample. The lower spectrum, plotted for comparison, was taken under the same excitation conditions from a defect-free area of the sample. See text for discussion of the compositional variation exhibited by the spectra.

the length of the defect, sometimes terminated by a triangular facet. The primary variation in defect morphology is in the center. In the center of the defect, there sometimes occurs a pit, similar in appearance to the defects pictured in Figure 6.1. Other defects exhibit a faceted central feature instead of a pit, which may include a spherical lump on one side (see Figure 6.3). Matteson and Shih noted the presence of faceted features and spherical protuberences in oval defects. They proposed that a liquid phase occurs in these oval defects during growth, which results from the agglomeration of gallium [12]. Defects similar to the faceted defects in MBE 775 were observed by Bafleur and Munoz-Yague, who attribute the origin of this type of defect to substrate preparation and contamination [13].

The oval defect in Figure 6.3 is typical of this sample. The low temperature SRCL images of the oval defect have a number of interesting features, which illustrate the spatial variation of the luminescence, and its correlation with the external features of the defect. The faceted center of the defect exhibits very strong luminescence. The SRCL image at 6800Å shows that the luminescence peak at 6800Å, which is very weak, originates from two of the facets in the center of the oval defect (see Figure 6.3.b). The luminescence at 7500Å also originates in the center of the defect, but in this case all of the facets are luminescing (see Figure 6.3.c). At 7600Å, the defect-free areas of the sample luminesce, but the center still exhibits the strongest luminescence (see Figure 6.3.d). At 8140Å, the center luminesces very strongly (see Figure 6.3.e).

The primary peak in the luminescence spectrum from the center of the defect

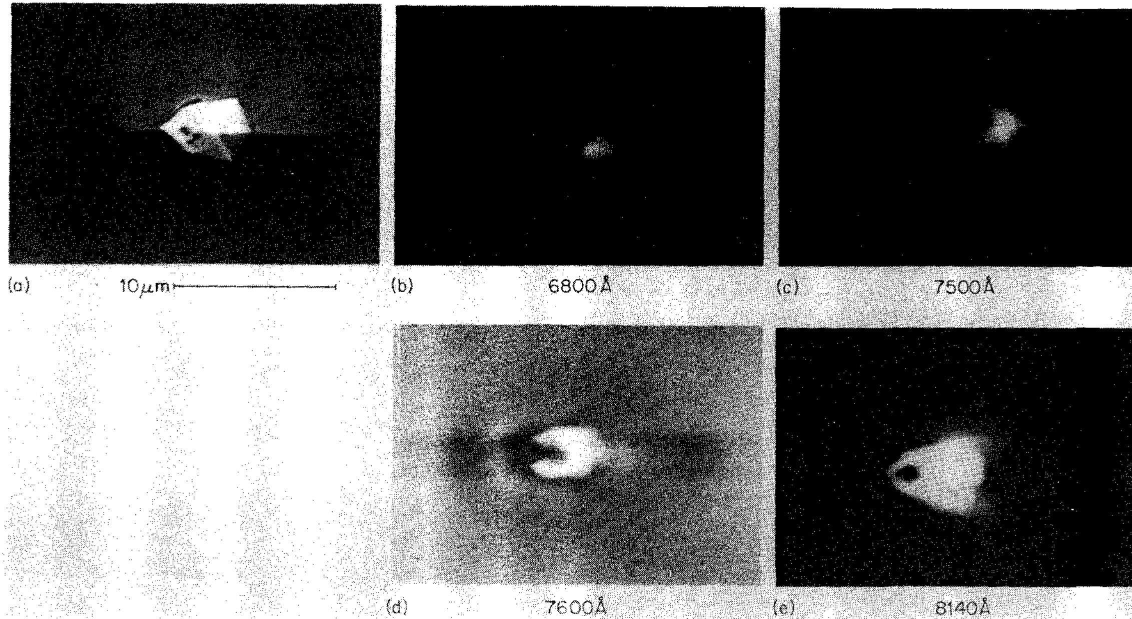

Figure 6.3: Secondary electron and cathodoluminescence images, taken at 77 K, of a typical oval defect in MBE 775, showing the variation in composition of AlGaAs in the vicinity of the defect. (a) Secondary electron image of the oval defect, showing the faceting characteristic of this type of defect. (b) Spectrally resolved cathodoluminescence (SRCL) image of the defect at 6800Å, taken at 77 K. This luminescence corresponds to a much higher aluminum concentration than the nominal value of $x \approx 0.07$. (c) SRCL image of the defect at 7500Å. (d) SRCL image of the defect at 7600Å. This image corresponds to the peak luminescence of $Al_{0.07}Ga_{0.93}As$ in the defect-free areas of the sample. (e) SRCL image of the defect at 8140Å. This image corresponds to the dominant luminescence peak from the faceted growth in the center of the defect, representing an 83 meV shift in energy relative to the defect-free AlGaAs.

occurs at 8160Å, with a smaller linewidth than the luminescence peak from the defect-free part of the sample (see Figure 6.4). In addition, there are at least five other peaks in the spectra from this part of the sample, at 6810Å, 7581Å, 7660Å, 8030Å, and 8300Å (this peak is identified as GaAs luminescence, probably arising from a band to donor transition). The luminescence from the defect-free part of the sample exhibits a single peak at 7720Å. Thus, the aluminum concentration in this oval defect differs significantly from that of the defect-free material in the sample, varying (at least) over the range $x \approx 0.01$ to $x \approx 0.22$ in different facets of the defect.

6.3.3 Sample MBE 815

The third sample studied, MBE 815, is interesting, because the substrate was patterned with grooves prior to growth. Luminescence of AlGaAs grown in the grooves is described in Chapter 3. The structure in this sample consists of a 1 μm GaAs buffer layer, a 1 μm $Al_{0.25}Ga_{0.75}As$ layer, a 100Å GaAs quantum well, and a 1000Å $Al_{0.25}Ga_{0.75}As$ cap layer. All layers were undoped. Grooves 15 μm wide were etched in the GaAs substrate prior to the growth. The growth was done with a Riber 2300 molecular beam epitaxy machine, using a substrate temperature of 600°C. The substrate was rotated at 48 rpm during the growth.

SRCL images of an oval defect in this sample are shown in Figure 6.5. The oval defect, shown in Figure 6.5.a, is of the α_4 type, with a length of approximately 13 μm, and a width of approximately 7 μm. The strongest shifts in the luminescence occur in the ends of the defect, Figure 6.5.d, and the faceted feature in the center of the defect, Figure 6.5.e. Luminescence from the sides of the defect is shifted to a slightly

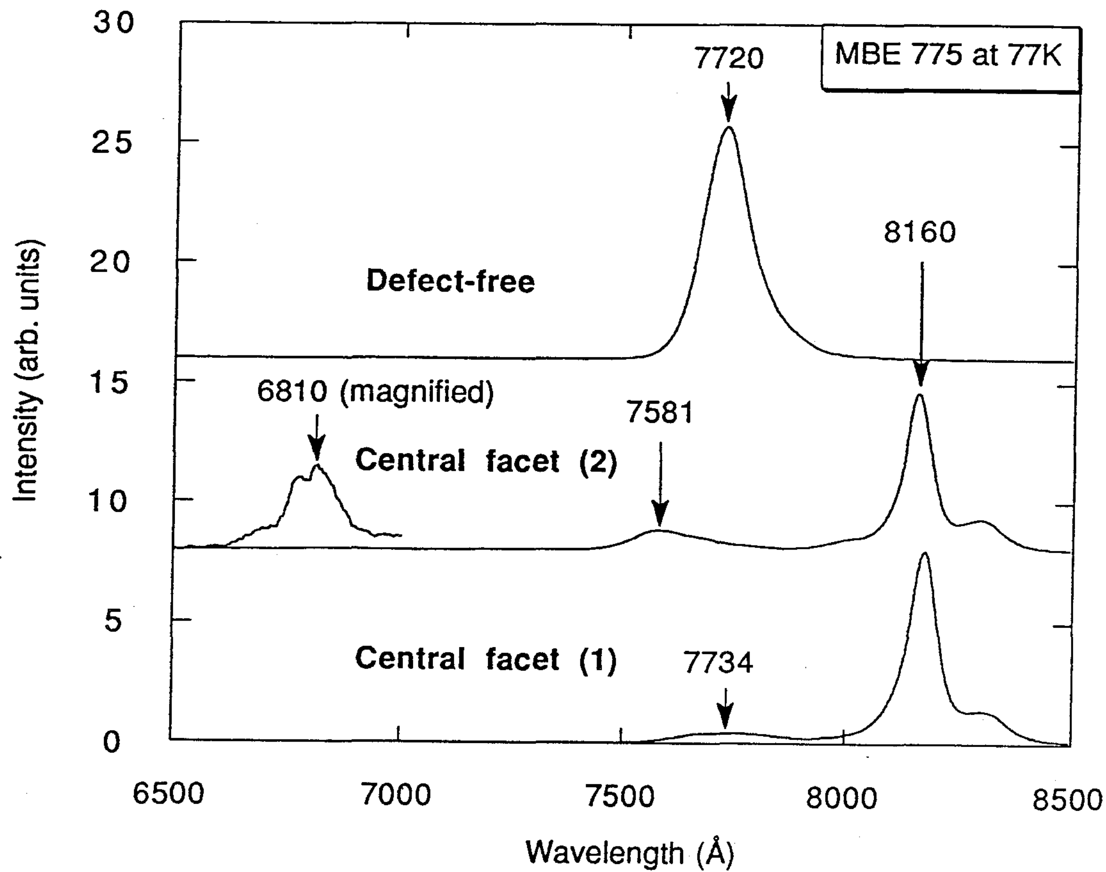

Figure 6.4: Cathodoluminescence spectra, taken at 77 K, showing luminescence from an oval defect in MBE 775. Luminescence spectra from two facets in the defect are shown. Facets 1 and 2 have narrow luminescence peaks, which are red-shifted relative to defect-free AlGaAs in the sample. Facet 2 has a strongly blue-shifted peak, appearing at approximately 6810Å, and a weakly blue-shifted peak at approximately 7581Å. The spectrum from the defect-free AlGaAs, shown for comparison, has a peak at 7720Å.

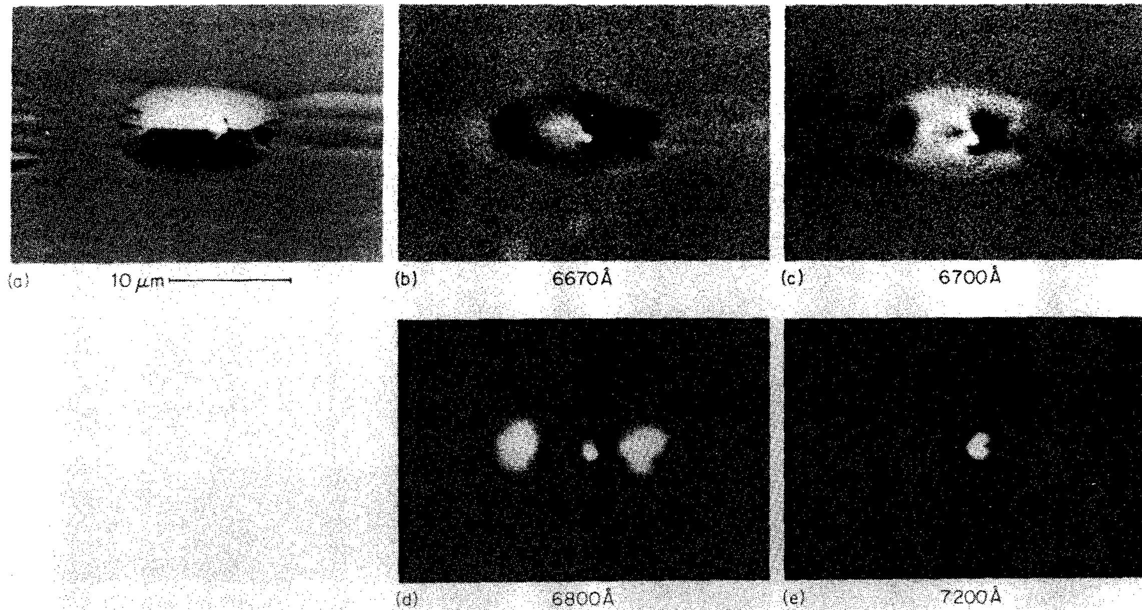

Figure 6.5: Cathodoluminescence images of an oval defect in sample MBE 815. (a) Secondary electron image of the defect, showing the dimensions of the defect and the external morphology. (b) Spectrally resolved cathodoluminescence (SRCL) image of the defect, showing luminescence at 6670Å. The defect-free part of the sample , and the center of the defect, luminesce at this wavelength. (c) SRCL image of the defect at 6700Å. The sides of the defect luminesce strongly at this wavelength, which is slightly red-shifted relative to the peak of the luminescence from the defect-free AlGaAs. (d) SRCL image of the defect at 6800Å. The ends and faceted center of the defect luminesce strongly at this wavelength. (e) SRCL image of the defect at 7200Å. Only the faceted center of the defect luminesces at this wavelength.

longer wavelength (Figures 6.5.b and 6.5.c).

Cathodoluminescence spectra from the faceted feature near the center of the defect exhibit two peaks (Figure 6.6), appearing at 6950Å and 7240Å. The ridge running down the center of the defect has a CL peak at 6650Å. Luminescence from the defect-free AlGaAs has a single peak at 6685Å. Luminescence from the side of the defect has a peak at 6700Å. The end of the defect has a CL peak at 6875Å. The luminescence emitted by the faceted central feature in the defect, which is much brighter than luminescence from other parts of the sample, has a peak at 7240Å.

A similar defect, which exhibited a very small pit instead of a faceted protrusion, had similar luminescence properties (see Figure 6.7). Luminescence from the pit has three peaks, at 7191Å, 6919Å, and 6688Å. The center of the defect exhibited peaks at 7191Å and 6651Å.

The cathodoluminescence data from oval defects in MBE 815 are to be compared to data from AlGaAs grown in grooves on the same sample, and in similar growths on grooves in samples NSI1, NSI2, and NSI3. These data are presented in Chapters 3 and 5 of this thesis. Discussion of the implications of similarities in the CL spectra of oval defects and grooves is deferred to section 6.4.

6.3.4 Sample NSI1

The fourth sample studied, NSI1, contained patterns of grooves arranged to study the growth of AlGaAs in a variety of surface orientations. A description of the sample, and results of cathodoluminescence measurements on the grooves, is presented in Chapter 5. The oval defect studied in this sample is of the α_4 type, very similar

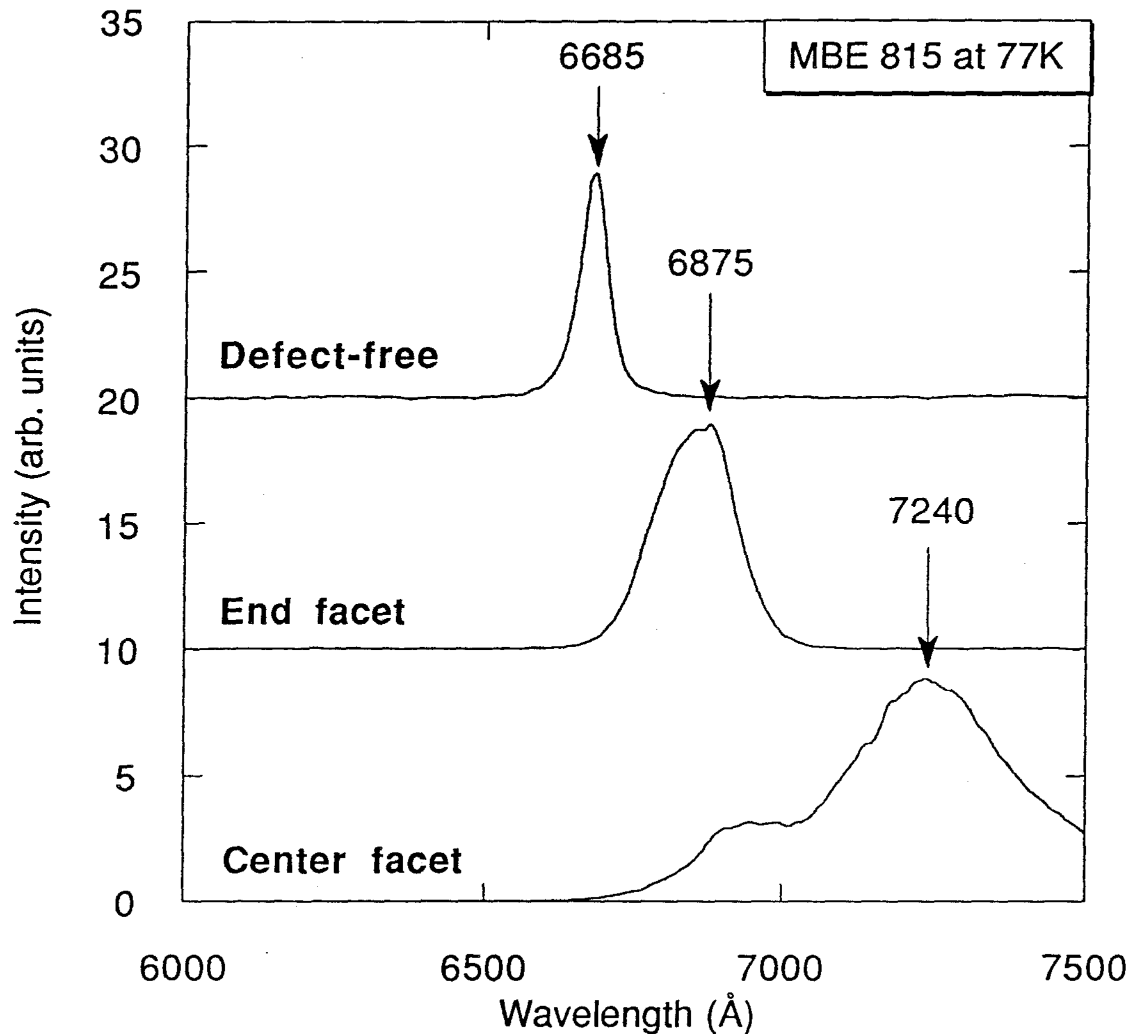

Figure 6.6: Cathodoluminescence spectra of an oval defect in MBE 815. Luminescence from the faceted center of the defect and the end facet of the defect are shown, with peaks at 7240Å and 6875Å, respectively. A luminescence spectrum from AlGaAs away from the defect, with a peak a 6685Å, is shown for comparison.

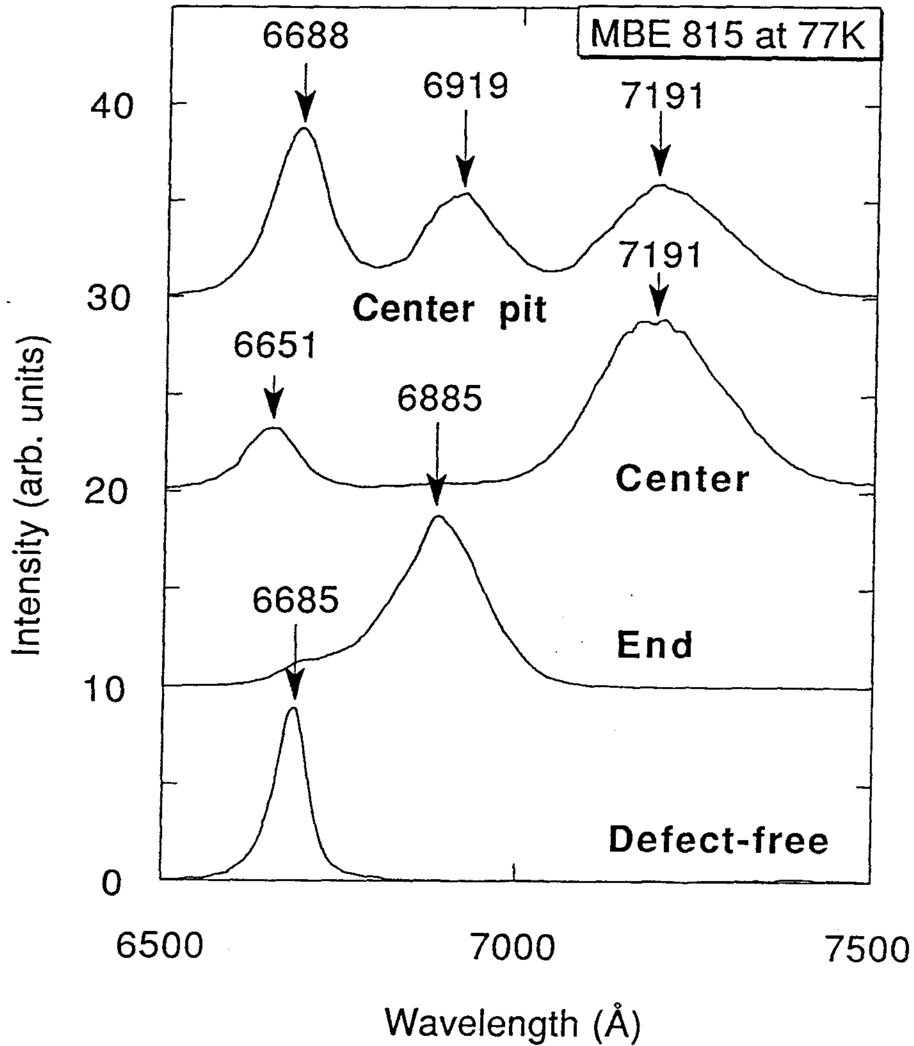

Figure 6.7: Cathodoluminescence spectra from a second defect in MBE 815. This defect is similar to the first defect, except that a pit appears in the center, rather than a faceted protrusion. Spectra from the pit, the center, and the end of the defect are shown, with the peak positions labelled. A spectrum from defect-free AlGaAs is shown for comparison.

morphologically to the first defect studied in sample MBE 815.

Cathodoluminescence spectra of the oval defect in this sample (Figure 6.8) are similar to those presented for sample MBE 815. The faceted feature in the center of the defect exhibits a broad luminescence peak at 7172Å. The end facet of the defect, which is similar to the end facet in MBE 815 (see Figure 6.5), has a luminescence peak at 6905Å. For comparison, luminescence from AlGaAs away from the oval defect is shown, with a peak at 6735Å.

6.3.5 Sample NSI3

The fifth and final sample studied, NSI3, contained patterns of grooves, similar to the the sample discussed in the previous section. This sample is described in Chapter 5. The oval defects studied in this sample were of the α_4 type. Cathodoluminescence spectra from the centers of three defects are presented in Figure 6.9, along with a spectrum from defect-free AlGaAs in the same sample, shown for comparison. The first two defects resemble the defects of sample MBE 815, and had similar spectral emission. The AlGaAs luminescence from these defects was shifted from 6639Å to approximately 7100Å. The third defect studied had a spherical protrusion in the center, similar to that observed by Matteson and Shih [12], and identified as a larger defect of the α_4 type by Fujiwara et al. [1]. Cathodoluminescence spectra from this defect exhibited two peaks, at 7373Å and 7650Å, strongly red-shifted relative to luminescence from defect-free AlGaAs.

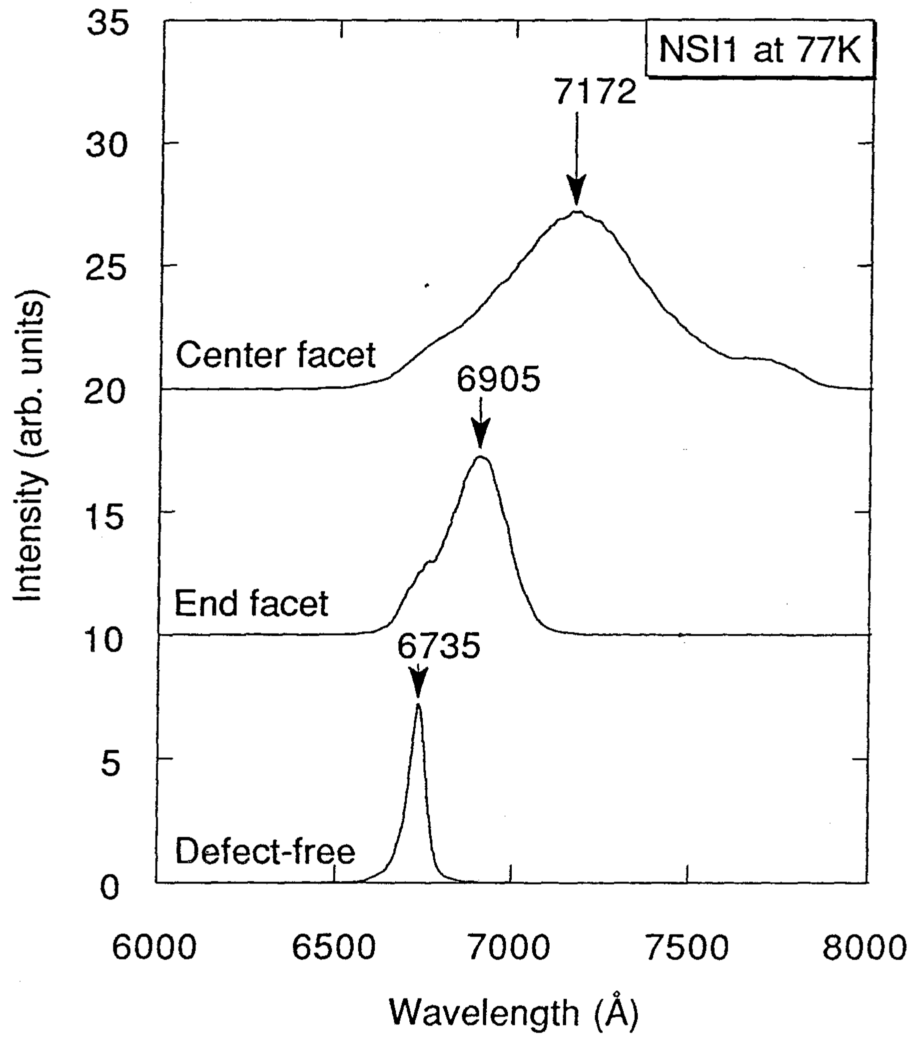

Figure 6.8: Cathodoluminescence spectra of an oval defect in NSI1. The end facet has a peak at 6905Å, and the center facet has a peak at 7172Å. The spectrum from defect-free AlGaAs, shown for comparison, has a single peak at 6735Å.

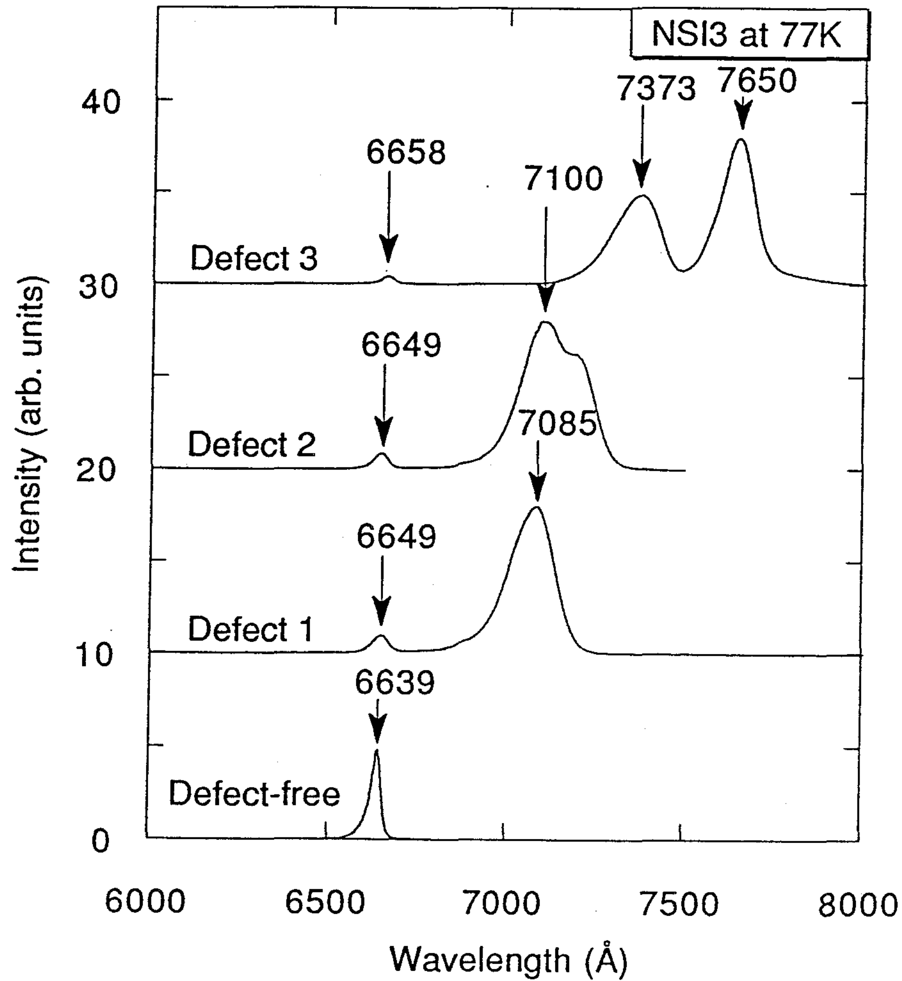

Figure 6.9: Cathodoluminescence spectra from the centers of three defects in sample NSI3. Defects 1 and 2 were similar morphologically, with faceted pits in the center. Defect 3 had a spherical protrusion in the center (see text).

6.4 Discussion: Variation of composition of AlGaAs in oval defects

The experimental data presented in section 6.3 demonstrate strong variation of the composition of AlGaAs in oval defects. This has been observed previously, and correlated to the mechanism of origin of these types of oval defects (see section 6.2). The data presented here indicate that there are at least two additional mechanisms responsible for the variation of aluminum concentration in oval defects.

6.4.1 Orientation selective epitaxy in oval defects

Growth on oval defects involves growth on several different crystalline orientations, and several different surface orientations. The crystal orientation inside an oval defect is not necessarily the same as the orientation outside the defect, so that the surface orientation is not a good indicator of the crystal orientation in the center of an oval defect [7]. This complicates interpretation of the data, because cathodoluminescence does not provide a direct measure of crystal orientation. Nevertheless, both surface orientation and facet orientation vary within the defects, and data on the grooves provide an interesting reference for comparison. In Chapters 3, 4, and 5, the relationship between facet orientation and aluminum concentration is studied in detail, for growth on grooves in a GaAs substrate. At a substrate temperature of 600°C, spontaneous segregation of aluminum and gallium is observed to occur in AlGaAs, forming a superlattice on the sides of the grooves.

Oval defects in the same samples used for the measurements on grooves were

studied in this chapter (sections 6.3.3, 6.3.4, and 6.3.5). The centers of two oval defects in sample MBE 815 luminesced at 7240Å (defect with faceted center), and 7191Å (defect with pit). AlGaAs on the end facets of this sample, and in the pit of the second defect, has a luminescence peak at approximately 6900Å. Similarly, an oval defect in sample NSI1 luminesces at 7172Å in the center facet, and at 6905Å in the end facet. Two of the defects in sample NSI3 luminesce at approximately 7100Å in the center. These three samples were grown under nearly identical conditions, and the oval defects were of the same type, with similar morphology[1].

Because the developing oval defect presents surfaces with a variety of orientations during the growth of epitaxial layers, it may be that some of the facets would exhibit segregation of the group III elements, resulting from the same mechanism responsible for orientation selective epitaxy. Comparison of the luminescence from oval defects and grooves shows a similar shift in peak wavelength, and an associated increase in the linewidth. In particular, the end facets of oval defects, which are expected to have approximately the same surface orientation as the sides of [011] grooves, exhibit nearly the same shift in wavelength. Comparison of luminescence from the non-faceted center of the second defect studied in MBE 815 with the $[01\bar{1}]$ groove shows a similar shift in peak wavelength. These comparisons of oriented growth on grooves and defects in the same samples indicate that orientation selective epitaxy causes

[1]A third defect in sample NSI3, with a much different morphology than the other defects studied in this chapter, exhibited two peaks, at 7373Å and 7650Å. This demonstrates that the composition is associated with the morphology of the defect, and that there is some diversity in the growth of oval defects within the same sample.

some of the observed variation in composition of AlGaAs grown in oval defects.

6.4.2 Surface diffusion in oval defects grown at high temperature

Previous photoluminescence and cathodoluminescence studies found that oval defects contain material with an enhanced concentration of gallium, but did not find evidence of an enhanced concentration of aluminum [8,10]. A study of oval defects using Raman spectroscopy did find evidence of a slight increase of the aluminum concentration, in a volume limited to the surface of the defects [7].

The spectra from oval defects in MBE 562, grown at 650°C, and MBE 775, grown at 720°C, have peaks which are quite narrow compared to the peaks present in spectra of the sample away from the defects. While MBE 562 has a high concentration of aluminum, which makes observation of an increased aluminum concentration difficult in cathodoluminescence studies[2], MBE 775 has a relatively low nominal aluminum concentration outside the defects. One of the facets of an oval defect in MBE 775 exhibited a luminescence peak at 6810Å, representing a 910Å blue shift of the luminescence. In addition, another blue-shifted peak, at 7581Å, is observed in this oval defect.

Interfacet surface diffusion of gallium is likely to have caused variation of the aluminum concentration in samples MBE 562 and MBE 775, both of which were grown at

[2]The luminescence efficiency becomes very poor as the aluminum concentration approaches 0.37, where the transition is made (at low temperature) from a direct to an indirect bandgap. In addition, luminescence from material with a lower aluminum concentration dominates luminescence from material with a higher aluminum concentration, for regions smaller than the minority carrier diffusion length.

higher temperatures than the other samples discussed in this chapter. Studies of high temperature growth of AlGaAs on nonplanar substrates have found that the surface diffusion length is quite long for some facets, giving rise to variation of the aluminum concentration on the scale of microns [14]. Surface diffusion induced variation of the aluminum concentration may also explain the relatively narrow luminescence spectra from oval defects in these samples. Because surface diffusion results in a gradual variation of the composition, the electrons in the facets would experience a graded potential. Carrier diffusion in a graded potential results in accumulation of the carriers in the lowest bandgap AlGaAs, accounting for the observed narrow luminescence spectra.

6.5 Conclusions

The composition of AlGaAs in oval defects of the α_3 and α_4 types has been found to vary. Previously, this observation was suggested to be a result of the mechanism of formation of the oval defects, which involves the accumulation of excess gallium during the growth. Variation of the aluminum concentration in oval defects was studied with cathodoluminescence, for five samples. The results were compared with growth of AlGaAs in grooves on three of the samples, in order to establish a connection between orientation selective epitaxy in grooves and the observed composition of oval defects. We conclude that orientation selective epitaxy contributes to variation of the aluminum concentration in oval defects grown at lower temperatures ($\approx 600°C$). At higher temperatures, oval defects are observed to have both enhanced gallium and

enhanced aluminum concentration in different areas of the defects. This suggests that interfacet surface diffusion during growth is responsible for some of the variation in composition of oval defects. This is consistent with the observation of narrow, red-shifted, luminescence lines from the oval defects grown at higher temperatures. Finally, these additional mechanisms for variation of the aluminum concentration do not preclude the previously suggested accumulation of gallium during formation of the defects. The overall composition of an oval defect is determined by several factors, which include the defect origin, surface diffusion, and orientation selective epitaxy.

Bibliography

[1] K. Fujiwara, K. Kanamoto, Y. N. Ohta, Y. Tokuda, and T. Nakayama, "Classification and origins of GaAs oval defects grown by molecular beam epitaxy," J. Cryst. Growth, **80**, 104 (1987).

[2] J. S. Smith, "III-V Molecular Beam Epitaxy Structures for Electronic and Optoelectronic Applications," Ph.D. Thesis, Caltech, Dept. of Appl. Phys. (1986).

[3] C. E. C. Wood, L. Rathbun, H. Ohno, and D. DeSimone, "On the origin and elimination of macroscopic defects in MBE films," J. Cryst. Growth, **51**, 299 (1981).

[4] R. A. Stall, J. Zilko, V. Swaminathan, and N. Schumaker, "Morphology of GaAs and $Al_xGa_{1-x}As$ grown by molecular beam epitaxy," J. Vac. Sci. Technol. B, **3**, 524, (1985).

[5] Shang-lin Weng, C. Webb, Y. G. Chai, and S. G. Bandy, "Particulates: An origin of GaAs oval defects grown by molecular beam epitaxy," Appl. Phys. Lett., **47**, 391 (1985).

[6] Masanori Shinohara and Tomonori Ito, "Thermodynamic study on the origin of oval defects in GaAs grown by molecular-beam epitaxy," J. Appl. Phys., **65**, 4260 (1989).

[7] J. Sapriel, J. Chavignon, and F. Alexandre, "Oval defects in $Ga_{1-x}Al_xAs$ molecular beam epitaxy layers: A Raman scattering and photoluminescence combined study," Appl. Phys. Lett., **52**, 1970, (1988).

[8] Michael E. Hoenk and Kerry J. Vahala, "Cathodoluminescence of oval defects in $GaAs/Al_xGa_{1-x}As$ epilayers using an optical fiber light collection system," Appl. Phys. Lett., **53**, 2062 (1988).

[9] Michael E. Hoenk and Kerry J. Vahala, "Cathodoluminescence system for a scanning electron microscope using an optical fiber for light collection," Rev. Sci. Instrum., **60**, 226 (1989).

[10] A. C. Papadopoulo, F. Alexandre, and J. F. Bresse, "Characterization of oval defects in molecular beam epitaxy $Ga_{0.7}Al_{0.3}As$ layers by spatially resolved cathodoluminescence," Appl. Phys. Lett. **52**, 224 (1988).

[11] T. F. Kuech, D. J. Wolford, R. Potemski, J. A. Bradley, K. H. Kelleher, D. Yan, J. Paul Farrell, P. M. S. Lesser, and F. H. Pollak, "Dependence of the $Al_xGa_{1-x}As$ band edge on alloy composition based on the absolute measurement of x," Appl. Phys. Lett., **51**, 505 (1987).

[12] S. Matteson and H. D. Shih, "Morphological studies of oval defects in GaAs epitaxial layers grown by molecular beam epitaxy," Appl. Phys. Lett., **48**, 47

(1986).

[13] M. Bafleur and A. Munoz-Yague, "Crystal, impurity-related and growth defects in molecular beam epitaxial GaAs layers," Thin Solid Films, **101**, 299 (1983).

[14] H. P. Meier, E. Van Gieson, W. Walter, C. Harder, M. Krahl, and D. Bimberg, "Molecular beam epitaxy of GaAs/AlGaAs quantum wells on channeled substrates," Appl. Phys. Lett. **54** 433 (1989).